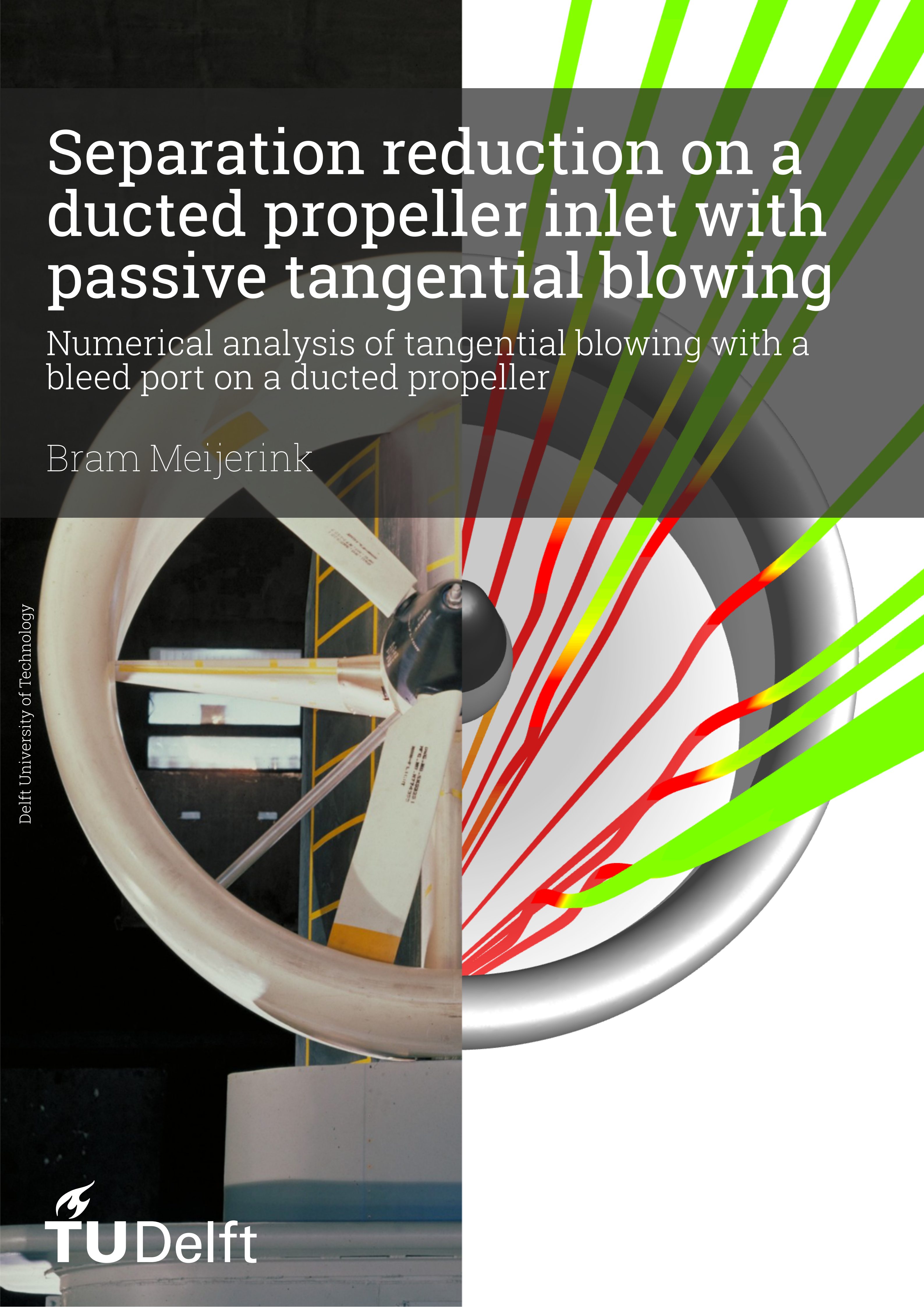

Separation reduction on a ducted propeller inlet with passive tangential blowing

Numerical analysis of tangential blowing with a bleed port on a ducted propeller

Bram Meijerink

Delft University of Technology

TU Delft

Separation reduction on a ducted propeller inlet with passive tangential blowing

Numerical analysis of tangential blowing with a bleed port on a ducted propeller

by

Bram Meijerink

to obtain the degree of Master of Science
at the Delft University of Technology,
to be defended publicly on September 8, 2025.

Student number:	4997328	
Project duration:	January 13, 2025 – September 8, 2025	
Thesis committee:	Prof. dr. ir. L.L.M. Veldhuis,	TU Delft, supervisor
	Dr. ir. T. Sinnige,	TU Delft, examiner
	Prof. dr. M. Kotsonis,	TU Delft, chair

Cover: ARC-1964-AC-32846 by NASA under CC BY-NC 2.0 (Modified)
Style: TU Delft Report Style, with modifications by Daan Zwaneveld

An electronic version of this thesis is available at `http://repository.tudelft.nl/`.

Preface

This thesis marks the end of six years of hard work and constant learning, a time I have enjoyed with all my heart. Although not easy at times, especially during the Covid era, the satisfaction I found in engineering has helped me through the most difficult of challenges. Utilising all the skills I have learned in the past years for this thesis has been a fulfilling conclusion to this chapter of my life. The thesis presented here tries to provide a passive solution to inlet separation on a ducted propeller. A form of active control could be supplied with the pressure created by a propulsor. As this topic had not been discussed in depth previously, I was eager to investigate it further. It has been wonderful to try and add a solution to a problem arising in the aviation industry.

For this project I would like to first of all thank my supervisor, Leo Veldhuis. As a knowledgable professor I have enjoyed learning from you and as a kind supervisor I have enjoyed our conversations about flow mechanics even more. Thank you for being available when I walked into your office to discuss thesis topics, thank you for allowing me the opportunity of diving into this CFD investigation. I hope it can function as a stepping stone for future analyses. I would additionally like to thank Tomas Sinnige and Alexander van Zuijlen. Professor Sinnige for his support on the remote desktop and Green Light Phase and professor Van Zuijlen for his support with the HPC12. I would also like to thank Navneet Chadha for his time during my internship. Your insights and lessons on CFD have allowed me to use it as an effective tool.

A lot of students have made it possible to do this research. Koen, Jack and Thomas, thank you for listening and providing insights. Thank you Elia for the help with the operation of the HPC12 and Kiril for the discussions on our shared topic. All provided a puzzle piece of the entire picture this thesis tries to solve. I would like to thank my friends, Dorothé, Fleur, Gerwin, Joshua, Lisa, Lily, Marco, Mauro, Noa, Thijmen, Tim, for listening to my talks about ducted propellers. I would like to thank the students I have had the pleasure of meeting and working with over the past six years. Everyone one of you taught me a bit more. A special thank you goes to the people from AeroDelft who have taught me a lot about taking responsibility.

My greatest gratitude goes out to my family. My father and mother who have supported me during the last six years. Every day I could call you for advise and support, even when you could not understand the problem entirely. My sister Emma, thank you for your interest, in my topic but also in my well-being. I feel loved by all of you. Thank you to my soon-to-be in-laws. Thank you for accepting me into your family. And finally thank you to my soon-to-be wife, Astrid. This thesis is written with your support as a driving force, thank you for never stopping to push me and never stopping to love me.

Bram Meijerink
Delft, August 2025

Contents

List of Figures

List of Tables

Nomenclature

Symbols

Symbol	Definition	Unit
A	Reference area	[m^2]
C_f	Skin friction coefficient	[-]
C_p, $C_{p,t}$	Static and total pressure coefficient	[-]
C_T, C_P, C_Q	Propeller coefficients for thrust, power and torque	[-]
c	Chord length	[m]
cc	Circumference	[m]
d_e	Duct exit diameter	[m]
D	Propeller diameter	[m]
D_H	Hydraulic diameter	[m]
$DC60$	Distortion coefficient for 60°	[-]
f	Darcy friction coefficient	[-]
J	Advance ratio	[-]
H	Boundary layer shape factor	[-]
H	Total enthalpy	[J]
h	Slot/port height	[mm]
L	Reference length for Reynolds number	[m]
L	Channel length	[m]
N	Propeller rotational speed	[rpm]
n	Propeller rotational speed	[rps]
$\bar{p}_{t,60^\circ,min}$	Lowest total pressure 60° on AIP	[Pa]
P	Power	[W]
P	Perimeter	[m]
p	Static pressure	[Pa]
PR	Pressure ratio	[-]
$\frac{P}{D}$	Pitch ratio	[-]
Q	Torque	[Nm]
q	Dynamic pressure	
R	Propeller radius	[m]
r	Radial coordinate	[m]
Re	Reynolds number	[-]
S	Kinematic entropy	[J]
T	Thrust	[N]
T_C	Propeller coefficient for thrust	[-]
t	Time	[s]
$\frac{t}{c}$	Thickness ratio	[-]
v	Velocity	[m/s]
$y+$	Non-dimensional cell height	[-]
B	Number of blades	[-]

Symbol	Definition	Unit
α	Angle of attack	[°]
δ	Boundary layer total thickness	[mm]
δ^*	Boundary layer displacement thickness	[mm]
η	Efficiency	[-]
θ	Boundary layer momentum thickness	[mm]
$\theta_{0.75}$	Propeller pitch angle at 75% of the radius	[°]
μ	Dynamic viscosity	[Pa s]
ρ	Air density	[kg/m^3]
ω	Propeller rotational speed	[rpm]

Subscripts

Symbol	Definition
j	Jet
p	Pressure
p, t	Total pressure
μ	Momentum
∞	Freestream condition

Abbreviations

Abbreviations	Definition
AIP	Aerodynamic Interface Plane
AJVG	Air Jet Vortex Generator
BEM	Blade Element Momentum
BBL	Blown Boundary Layer
CAD	Computer Aided Design
CFD	Computational Fluid Dynamics
DC60	Distortion coefficient for 60 degrees
DFDC	Ducted Fan Design Code
EVM	Eddy Viscosity Model
ISA	International Standard Atmosphere
NACA	National Advisory Committee for Aeronautics
MRF	Moving Frame of Reference
PIV	Particle Image Velocimetry
PTB	Passive Tangential Blowing
RANS	Reynolds Averaged Navier-Stokes
RBM	Rigid Body Motion
RST	Reynolds Stress Transport
SA	Spalart-Allmaras turbulence model
SIMPLE	Semi-Implicit Method for Pressure Linked Equations
SST	Shear Stress Transport
URANS	Unsteady Reynolds Averaged Navier-Stokes
VLM	Vortex Lattice Method
VTOL	Vertical Take-Off and Landing

Abstract

The current energy transition effects the aviation industry heavily. To find sustainable propulsion systems, electric power systems are proposed and with that the interest in propellers has increased. The concept of ducted propellers can increase the efficiency of propeller systems. However, ducted propulsion systems are limited in operation by inflow conditions. High angles of attack can lead to separation on the inlet of a duct or nacelle, causing distortion on the propeller or fan. This thesis discusses the use of passive momentum addition on a ducted propeller to reduce the separation on the lower lip of the inlet. The simulation was performed on the ducted propeller design of the Bell X22. A hybrid CFD simulation was applied where the propeller is modelled by an actuator disk with an applied pressure jump. This pressure jump was derived from the low fidelity ducted propeller simulation program Ducted Fan Design Code (DFDC). With a half model of the duct the separation on the lower lip was investigated. The unsteady RANS solver from Ansys Fluent was used to solve for unsteady separated flow. Using tangential blowing on the lower lip the separation on the lower lip was postponed and the distortion on the propeller plane was reduced. With active momentum addition a prescribed momentum coefficient was applied on the blowing slot and the distortion factor DC60 could be reduced by 78% with a C_μ of 6%. To discuss the passive momentum addition, the pressure on a flush and ram port behind the propeller were measured. The measured pressure was applied to the blowing slot, with an additional loss factor. This loss factor was based on a channel flow equation, similar to the Darcy-Weisbach equation. The system with a ram port displayed significant reduction in distortion, a reduction of 50% in DC60 was possible. At higher thrust setting, the distortion was reduced by 63% with respect to the original duct design. Using a flush port, the distortion factor was not reduced, but increased by 23%, while at high thrust the increase is 9%. It was found that the flush port provided a low momentum coefficient, which was applied at the slot. In practice, this displaces the boundary layer with a lower momentum boundary layer. The boundary layer close to the surface has low momentum which cannot move through the adverse pressure gradient induced by the curvature of the duct. This induces separation, even though the system is intended to postpone separation. The results indicated the possible effectiveness of the passive tangential blowing system with a ram port, while a possible problem with the tangential blowing concept was identified for low momentum values. It was concluded that the system proposed in this thesis operates effectively if a ram port is utilised. Additionally, it was concluded that any system functioning on the concept of tangential blowing can also induce separation.

1

Introduction

The history of aviation has displayed a variety of propulsion mechanisms. During the early years, simple propellers were used, but since the 1960's the jet engine has been used as propulsion system for larger airplanes. Traditional combustion engines burn fuel for the power generation, which contributes to environmental pollution. In sustainable electric propulsion systems, propellers are driven by electric motors to transfer the generated power into propulsive power. This renewed interest in propellers has driven a closer look into advanced propeller designs. One of these designs is the ducted propeller, which was recently discussed by Jiang et al. [1]. For a ducted propeller, a round shroud is placed around the propeller. The result is that ordinary losses associated with tip leakage on the propellers can be prevented. The advantage is more thrust generation for the same provided power, most notable at higher propeller loading. A problem that can occur with a ducted propulsion system is distorted inflow. Due to distortions, turbofan engines are prone to compressor stall, a condition discussed by Mohankumar et al. [2] in which a fan cannot compress airflow effectively. For ducted propellers distorted inflow may result in uneven propeller loading, leading to propeller damage or performance loss. The distortion of interest in this thesis is induced by the angle of attack of the propeller. This angle of attack is effected by the aircraft attitude or heavy crosswinds. In wind tunnel tests the distortion phenomenon has been analysed [3]–[7]. These tests require expensive installations and measuring equipment. Additionally, the complicated nature of flow control on a propulsion system may require more data than can be extracted in physical tests. With CFD simulations, distortion and local flow fields can be visualised more in-depth [2] [8], as can be seen in the work of Nambiar et al. in Figure 1.1. Usually, CFD simulations are simplified due to computational constraints. However, as it negates the need for a physical test model, it is the type chosen for this thesis.

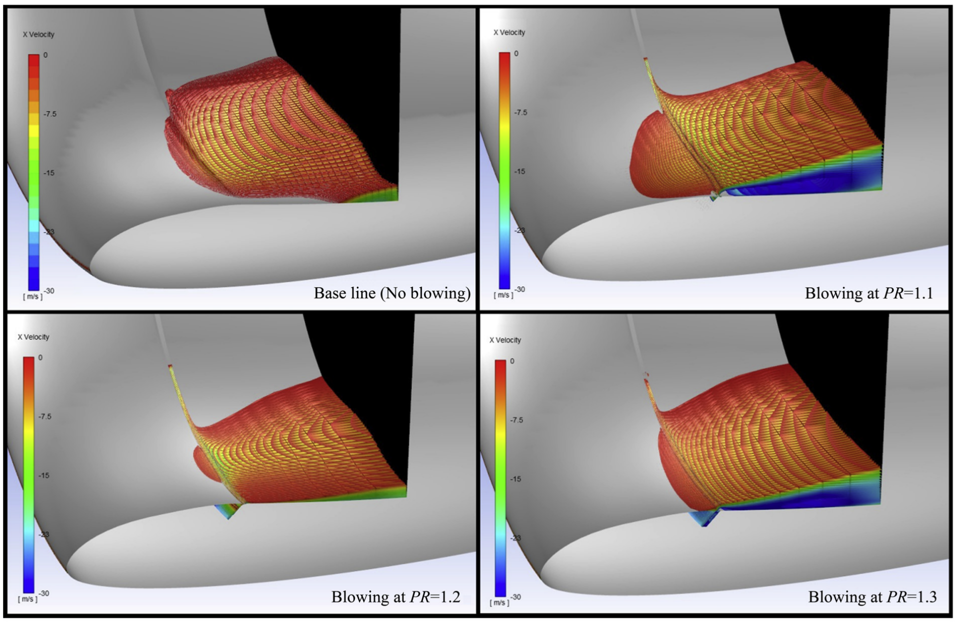

Figure 1.1: Isosurfaces indicating separation on a nacelle inlet under an angle of 20°. The baseline case is compared to the active control cases. The use of active flow control can postpone separation. Work by Nambiar et al. [8].

To prevent disrupted inflow in a ducted inlet, active separation control can be used. With active flow control, the behaviour of the flow can be manipulated with controllable system. In contrast, passive flow control requires no additional operation of a secondary system. Various types of active flow control in a range of conditions have proven to reduce distortion in the inlet [3]–[11]. The goal is to prevent separation occurring on the inside of the ducted inlet, which causes the distortion on the propeller or fan. Separation can be postponed or prevented by energising the boundary layer. In this report the concept of tangential blowing is considered, which has been applied to simple geometries [12] [13], but also to inlets of nacelles [8]–[10]. A difficulty with the active blowing concept is that it relies on the source of the blown air. This source has to be certified, which makes it difficult to implement in commercial propulsion systems. This thesis looks into the option of taking the pressurised air behind the ducted propeller as a source for the blowing air. The goal is to investigate whether the pressure bypass line can prevent separation on a ducted propeller.

In chapter 2, the scientific background is investigated. The concept of ducted propellers is discussed and relevant reference cases are presented. Additionally, the type of flow control and parameters of relevance are analysed. Next, chapter 3 discusses the methodology applied in this thesis. The method of prescribing the pressure jump over the actuator disk is presented, as are the CFD setups for the 2D and 3D cases. The setups are validated in chapter 4. Reference data from other analyses are compared to results from the used setup. With the validated setups, results can be extracted with a known degree of accuracy. The results of the analyses are presented in chapter 5. Both integral effects as well as local flow behaviour are presented in this chapter. Conclusions from these results are drawn and discussed in chapter 6. Finally, recommendations for further research are presented in chapter 7.

2

Literature study

In this chapter, the results from the literature study are discussed and conclusions from this study are presented. In section 2.1 the relevant theory of propellers and ducted propellers are presented. In section 2.2 the behaviour of a boundary layer and onset of separation are discussed. Common boundary layer control techniques and their results are discussed as well. The aerodynamic separation of ducted propulsion systems are discussed in section 2.3. Furthermore, the flow control techniques applied to ducted system are discussed here. Finally, the conclusion from the literature study are presented in section 2.4. The research question of this thesis and the sub-questions derived from this research question are presented here as well.

2.1. Ducted propellers

2.1.1. Propeller operation

Propeller blades experience similar aerodynamic behaviour as lifting surfaces. Where the high pressure side meets the low pressure side, a vortex is generated. This generation can be associated with losses and performance reduction. As propellers rotate, their tips operate at larger velocities than the root. Most propellers are thus more outward loaded as compared to wing. Highly loaded blades cause strong vortices, which can interact with other surfaces. To mitigate the effect of these vortices, the propeller tip is usually designed with a reduced load. On the blades this is visible as the blade tapers towards the tip.

In some numerical models the tip losses are modelled with a tip-loss factor. Simple, low-fidelity models can calculate propeller loading. One such model is the Blade Element Momentum (BEM) model, which is often equipped with a loss factor as seen in Figure 2.1. As a BEM model integrates airfoil loads over the propeller, no 3D effect can be captured. To take 3D flow effects into account, loss factors are required. With the early loss factors introduced by Prandtl [14], a BEM model can model propellers more accurately. One can see that the losses become prominent towards the tip. Other models, such as lifting line model, may not require the loss factor, as their nature allows for the modelling of the tip vortex.

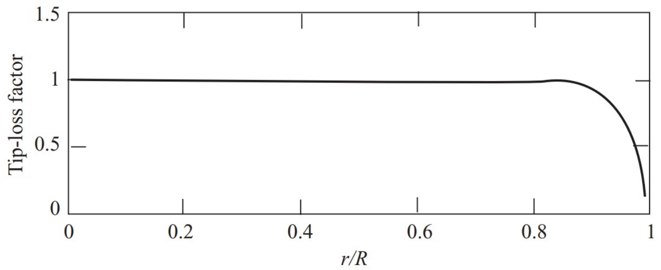

Figure 2.1: Tip-loss factor for uniform circulation as illustrated by Burton et al. [15]. It illustrates the losses induced by the tip vortex.

When discussing the operation of a propeller it is common practice to discuss the advance ratio J. This variable indicates the distance a propeller advances in a single rotation. It gives a non-dimensional indication of what the local inflow angle at the propeller is. The advance ratio is defined as ratio:

$$J = \frac{v_\infty}{nD} \tag{2.1}$$

The upstream velocity v_∞ is divided by the propeller diameter D and the rotational rate n in revolutions per second. This definition is according to SAE International [16]. Since this convention is used often, it is also used in this report. For propeller performance characteristics, the SAE report also determines the following definitions, which will be adhered to during this thesis report:

$$C_T = \frac{T}{\rho n^2 D^4} \quad (2.2) \qquad C_Q = \frac{Q}{\rho n^2 D^5} \quad (2.3) \qquad C_P = \frac{P}{\rho n^3 D^5} \quad (2.4)$$

From the thrust and power coefficient one can also find the efficiency, as can be found in (2.5). In this report the following alternate definition of thrust coefficient will also be used. In this equation T is the thrust delivered in axial flow conditions, q_∞ is the upstream dynamic pressure, c is the duct length and d_e is the duct exit diameter. The duct that will be discussed in this thesis is from the Bell X22, with a chord of 1.24 m and a diameter of 2.37 m.

$$\eta = \frac{C_T}{C_P} J \quad (2.5) \qquad T_C = \frac{T}{q_\infty c d_e} \quad (2.6)$$

2.1.2. Effect of a duct

As discussed, the tip vortices can yield significant losses. This is generally associated with highly loaded propellers, so solutions have been introduced to inhibit the effects of this interaction. In the marine industry, it is common to use highly loaded propellers in stationary or low speed conditions. The application of a large ring around the propeller has proven to benefit this case. In this industry, this is called a Kort nozzle and it is an example of a ducted propeller. One aspect of the ducted propeller concept leans on the fact that the ring or duct limits the interaction of the high and low pressure sides of the propeller. In Figure 2.2 the CFD results from Bento et al. [17] display the difference in loading on the propeller. Note that the advance ratio is equal, but C_T for the isolated and ducted propeller are 1.13 and 0.864 respectively. The thrust provided by the propeller is lower, but the total ducted propeller system provides a C_T of 1.05.

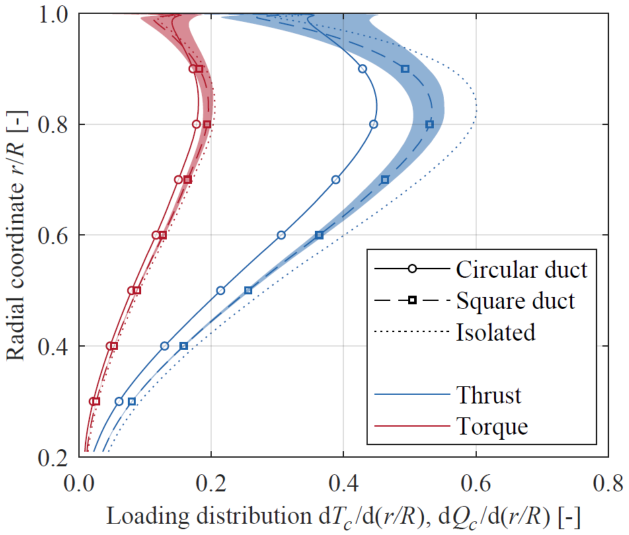

Figure 2.2: Loading distributions for an isolated propeller and a ducted propeller with a square of circular duct at J = 0.7. The loading distribution for a circular duct is more even distributed in comparison to the isolated propeller. The load on the isolated propeller drops at the tip, while the ducted propeller is more evenly loaded towards to tip. From the work of Bento et al. [17].

As can be observed, the outer tip of the propeller caries more load compared to an unducted propeller. Another observation is that the loading is more distributed, indicating that the duct effects the propeller inflow and thus influences the entire propeller. In the flow, the slipstream behind an unducted propeller contracts, due to the added pressure trying to find an equilibrium with the ambient pressure. This increases velocity in the slipstream, resulting in a contraction. Ducted propellers restrict the slipstream from contracting, as the flow is guided by the duct nozzle. According to Black et al. [18], the larger slipstream behind the propeller induces a larger mass flow through the propeller. In turn, this yields a larger suction force on the inlet of the duct, resulting in more thrust. This is seen in the performance data from Bento et al. [17], which indicates that thrust is produced by the duct. Turbojet nacelles often have a diverging diffuser before the fan, illustrated in Figure 1.1. This reduces the Mach number the fan experiences, reducing losses due to shock waves.

It can be concluded that a duct can influence the tip vortex on a propeller, but can also influence the inflow to the propeller. The ducted propeller can be particularly of interest in low speed, high thrust situations. The negative effects of the duct become more prevalent at higher speeds. Black et al. [18] state that the restriction on the slipstream by the duct becomes less effective. The higher velocity causes the slipstream to contract less. Therefore, the restriction posed by the duct is less effective as well. Additionally, the propeller operates at a lower load in cruise. The performance of a ducted propeller in Figure 2.3 illustrates the difference in high thrust and high efficiency. The more efficient advance ratio of a propeller is usually a lower loaded condition.

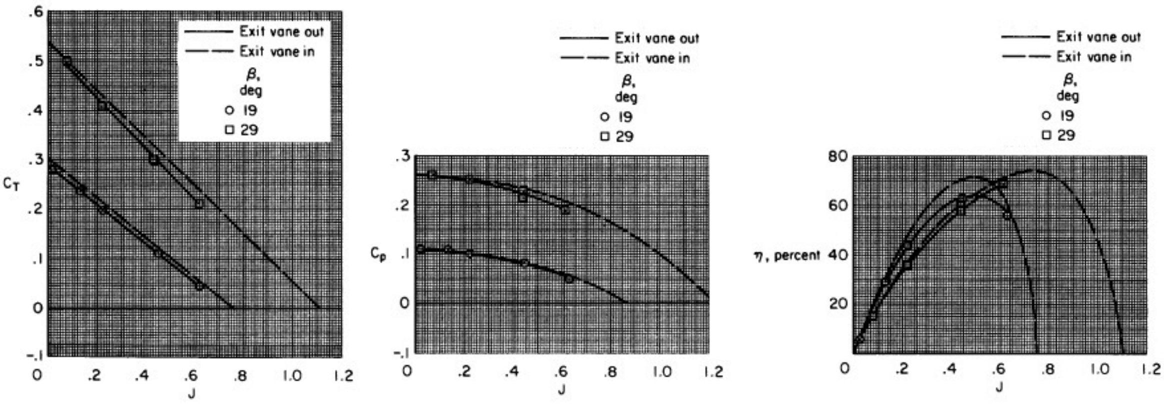

Figure 2.3: Performance parameters C_T, C_P, η with respect to the advance ratio. These graphs are from wind tunnel data of the Bell X22 ducted propeller, analysed by Mort et al. [19].

The lower propeller loading in turn reduces the effect of the vortex restriction by the duct. Simultaneously, the duct generates more drag at higher speeds, thus reducing the net thrust output of the system. In literature, the effectiveness of the duct has been investigated and it has proven to be very design dependent. The United States Army already researched the applicability of ducted propellers in the 1960's and found that open propellers outperformed the ducted variant at medium speed [20]. Pereira [21] discussed the behaviour of the performance for a ducted propeller as well. The results indicated that the thrust provided by the ducted propeller quickly reduced with increasing axial airspeed. Yilmaz et al. [22] discuss the performance tests of a small propeller. The duct started adding negative thrust to the system at advance ratios over 0.35 irrespective of which duct was tested. For the various duct shapes tested by Bontempo et al. [23], the open propeller had higher efficiency than some tested ducted variants at low thrust coefficients. Bento et al. [17] compared a square and circular duct with an isolated propeller. At an advance ratio of 0.7 it was found that even though the thrust was reduced with a circular duct, the circular duct did provide a slightly higher system efficiency. In prototypes, the ducted fan has been applied as a replacement for conventional propulsion systems. For example, the Airbus E-Fan concept was equipped with a ducted fan [24].

Figure 2.4: Bell X-22 (US Army, 1965) VTOL aircraft. This VTOL test bed is an application of ducted propellers.

Previously, it was stated that the propellers are designed with reduced tip loading to reduce the vortex losses. However, a ducted propeller can be loaded up to the tip as the losses are reduced. Therefore, the entire design is significantly different to an unducted propeller. As it has proven costly to design new propellers for this application, the number of tested full scale ducted propellers have been low. One of the few publicly available designs which has been tested, is the propulsion system of the Bell X22 [19], seen in Figure 2.4. The US Navy displayed interest in VTOL transport vehicles, requesting a prototype aircraft in 1962. In 1966 the maiden flight of the VTOL X22 occurred. Even though it never reached production, it has provided the industry with insights in the development of VTOL systems. The ducted propellers were utilised as it allows for higher loaded propellers, which are needed for the vertical thrust during take-off and landing. In recent years, the ducted propeller designs have increased in (electric) Vertical Take-Off and Landing (eVTOL) concepts, yielding designs mostly kept proprietary.

(a) Model used by Kriebel et al. [25]

(b) Model used by Mort et al. [19]

Figure 2.5: Tested model of the ducted propeller from the Bell X22

As can be seen in Figure 2.4 the ducted propellers may operate in extreme angles of attack. This feature is indicative of a VTOL aircraft, where the take-off and cruise phases blend. Propulsion systems thus operate in severe incidence angles. A lot of documentation can be found on the performance of the Bell X22 [26] [27], as well as on the performance and design of the ducted propeller itself [25] [19]. The tested models are presented in Figure 2.5a and Figure 2.5b. This ducted propeller is therefore taken as the design that will be discussed during this thesis.

2.2. Boundary layer behaviour and control

To understand the options for boundary layer control, it must be understood how a boundary layer behaves. The implementation of control can be done based on the fundamentals, especially as different control types are based on different concepts.

2.2.1. Fundamentals of boundary layer separation

Hermann Schlichting and Klaus Gersten explain the boundary layer behaviour and separation onset in their book [28]. The boundary layer close to a surface loses momentum through the friction on this surface. Per definition, the flow on the surface has no velocity, this is known as the no-slip condition. The slowed flow takes momentum from the flow around it through momentum transport. When the surface has a curvature, the pressure of the flow varies. On a diverging section of surface, the velocity of the flow is reduced and the pressure increased. The increase in pressure is a direct effect of the Bernoulli principle in low Mach number flows. Schlichting et al. [28] introduce the adverse pressure gradient, which results from a higher pressure upstream. The boundary layer loses momentum through friction and additionally through the adverse pressure gradient. Once the momentum from the boundary layer becomes too low, the flow can start separating. This is visualised in Figure 2.6.

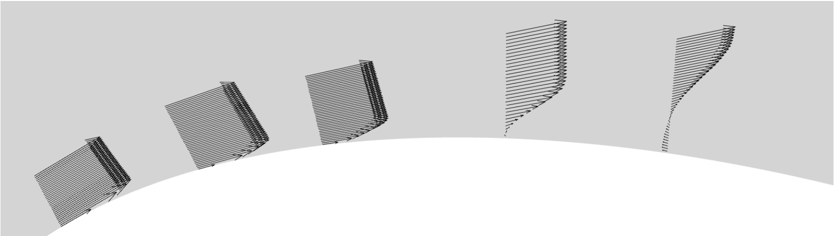

Figure 2.6: Velocity vectors displaying the process of boundary layer separation over a curved body in a 3D analysis of the author. The momentum close to the surface is reduced by friction and the adverse pressure gradient until the separation point. The first and last profile displayed are at 0.012 and 0.12 m along the leading edge of the ducted propeller inlet respectively. v_∞ = 13 m/s, J_∞ = 0.522, α = 35°, $\theta_{0.75}$ = 19°

The result is a boundary layer with reversed flow. This can lead to a local separation with reattachment, known as a separation bubble, or to separation of the entire boundary layer. In many conditions separation is an unwanted behaviour and thus preferably prevented. For a wing, separation results in a loss of lift and an increase in drag. For ducts, the separation induces distortion to the flow through the duct.

In practice, the shape of the local boundary layer can be described numerically. The boundary layer thickness δ indicates the height of the boundary layer. Additionally, the boundary layer displacement thickness δ^* can be calculated, which indicates the boundary layer thickness if a uniform flow would be present. According to White et al. [29], the thickness added to the surface describes the effective body an inviscid flow would observe. In Figure 2.7, the boundary layer thickness and the equivalent inviscid thickness are illustrated.

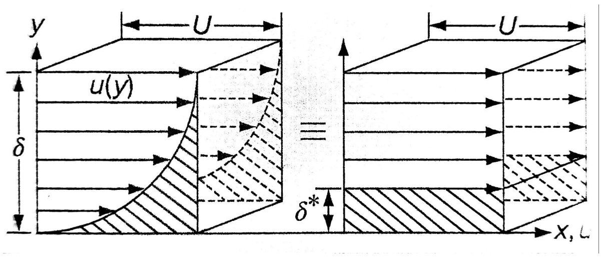

Figure 2.7: A boundary layer with boundary layer thickness δ compared to the equivalent inviscid, irrotational, uniform boundary layer with the displacement thickness δ^*. Figure from the work by White et al. [29].

It is also possible to define the momentum thickness θ, which can be related to the drag force on the body. H is the shape factor and numerically quantifies the shape of the local boundary layer profile. A higher number implies a more distorted boundary layer and can thus indicate the state of the boundary layer. Castillo et al. [30] found that the separation criterion for the shape factor is around 2.7. Equation 2.7, Equation 2.8 and Equation 2.9 describe the mathematical definitions used by White et al. [29] for δ^*, θ and H respectively. For a flat plate White et al. derive (2.7) and (2.8) from the conservations of mass and momentum respectively.

$$\delta^* = \int_0^{\delta} (1 - \frac{v}{v_\infty}) dy \qquad (2.7) \qquad \theta = \int_0^{\delta} \frac{v}{v_\infty}(1 - \frac{v}{v_\infty}) dy \qquad (2.8) \qquad H = \frac{\delta^*}{\theta} \qquad (2.9)$$

In these equations v is the velocity locally in the boundary layer and v_∞ is the freestream velocity. Note that this analysis by White et al. is done for a laminar boundary layer on a flat plate with no curvature. Therefore the integral can go until the freestream, which mathematically can be ∞. Since all boundary layers in this document will experience surface curvature, the integral is taken until the edge of the boundary layer δ. This edge is defined as the maximum velocity in the boundary layer, without the flow controlled region. The presented equations are derived for incompressible flows, which will be considered in this thesis. In further discussions White et al. describe that the mentioned principles hold for turbulent flows as well, although the exact numerical values might be slightly different.

2.2.2. Separation control

Separation control is the practice of manipulating the boundary layer such that it will be delayed or prevented from separating. In general, there are two distinct types of separation control, active and passive control. Active control uses a power source to prevent separation, while passive control does not require a power source. In the industry, active control is less applied, as regulations stipulate strict reliability requirements [31]. For active boundary layer control systems this safety aspect is often difficult to adhere to as it is dependent on the power system.

In practice, the passive control systems are thus used more often. A well known case of passive control is the use of vortex generators (VG) [32]. VGs are small surfaces that induce a vortex, which mixes the boundary layer and the freestream flow. This allows the boundary layer to be energised and stay attached longer, thus postponing or even preventing separation. It is a geometric modification often used on aircraft. The drawback of this passive system is that the system is always present. In cruise the VG also generates a vortex, while separation is often not a problem in cruise. The added vortex does add vortex induced drag, which reduces the efficiency of the aircraft.

An active system has the advantage of being controllable. When not needed, the system can be turned off. Deployable VGs are also under investigation, but often require an active system to be deployed. This makes the VGs a form of active flow control. Other types have also been proven to enhance separation postponement. For example, suction can be used to remove the low momentum boundary layer. This was explained by Schlichting [33] and has been tested for multiple applications, as described by Gad-el-Hak et al. [34]. A suction system has the disadvantage of requiring a low pressure system. In an applied situation, high pressure air is easier to bleed than low pressure air. The most common way of using an active system is using the bleed air from the engine or a separate compressor. Other solutions utilise acoustics to manipulate the boundary layer [35].

An example of flow control linked to a bleed line is discussed in the patent by Winter et al. [36]. This thesis discusses flow control on a propeller system, thus high pressure can be bled. For this reason, energising the boundary layer with bleed air is of interest. This means control mechanisms not using air jetting, will not be further discussed. When injecting air into the boundary layer, two options are usually possible. The air can be injected perpendicular to the flow, causing a vortical structure to be formed in the airflow. The boundary layer and freestream flow are mixed. It has a similar working principle as a vortex generator and is therefore called an Air Jet Vortex Generator (AJVG). The vortex generated is shown in Figure 2.8 by Hayböck et al. [11].

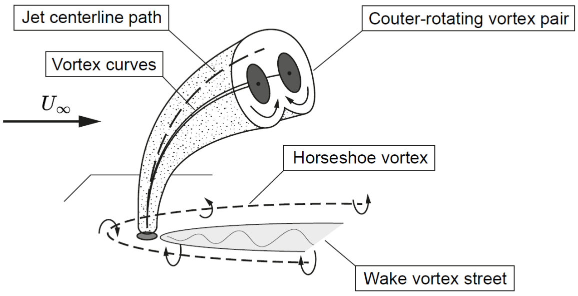

Figure 2.8: Vortex generated by a jet perpendicular to the surface, generating two counter-rotating vortices. This system functions similarly to a VG and is named an Air Jet Vortex Generator (AJVG). Figure from Hayböck et al. [11].

Kumar et al. [37] discussed the use of blowing air in the boundary layer to generate streamwise vorticity. Experiments showed that the system was effective on a Stratford ramp in an adverse pressure gradient. To further enhance the momentum mixing, some applications use oscillating injectors. Boeing has applied this system to the vertical stabiliser of their 757 ecoDemonstrator [38]. It has been operated in large side-slip angles and proved to enhance the attachment of the boundary layer of the tail.

The second option is injecting the air tangential to the local flow field. As discussed before, the boundary layer loses momentum at the interaction with the surface. Tangential blowing injects air into this region to add momentum to the lower part of the boundary layer. This will prevent the boundary layer from taking momentum from higher in the stream. There are multiple names for this concept, but in this thesis the concept is named tangential blowing. The resulting boundary layer influenced by tangential blowing is called a blown boundary layer (BBL). The term 'momentum addition' indicates the amount of momentum added to the flow. In Figure 2.9 this process is visualised.

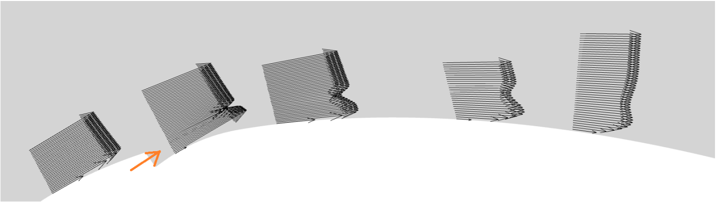

Figure 2.9: Velocity vectors displaying the development of a boundary layer with tangential blowing. From CFD simulations performed by the author, the air is injected tangentially along the orange arrow. Compared to Figure 2.6 at the same conditions with a similar setup, separation is postponed.
v_∞ = 13 m/s, J_∞ = 0.522, α = 35°, $\theta_{0.75}$ = 19°, C_μ = 3.8%

In literature, the input to the momentum addition is measured in one of the following two descriptions.

$$C_\mu = \frac{\dot{m} v_j}{q_\infty A_{ref}} \qquad (2.10) \qquad\qquad PR = \frac{p_{0,bl}}{p_{0,\infty}} \qquad (2.11)$$

The momentum coefficient C_μ in Equation 2.10 relies on a prescribed velocity on the jet. It can be used to prescribe a momentum addition to the flow, as can be done in CFD. When no momentum addition can be prescribed, pressure ratio PR is used. Especially in wind tunnel conditions, it is difficult to ensure a momentum coefficient and PR as defined in Equation 2.11 is applied. It is also applied in more complex cases as done by Nambiar et al. [8]. If the applied system is a duct or nacelle, the pressure ratio is often linked to a bleed percentage. This would be the amount of bleed needed from the mass flow through the geometry to operate the tested condition.

Both in numerical CFD simulations as well as physical wind tunnel experiments the tangential blowing concept has been tested. Saripalli et al. [39] proved that with the correct jet, a flow can stay attached for longer in an adverse pressure gradient. It was later also tested on the lower half of an airfoil mounted to a wall by Borgmann et al. [12]. The tests displayed that a closely spaced array of wall jets operate more effectively than a larger spaced setup. With Particle Image Velocimetry (PIV) the flow fields around 75% of the chord were recorded. The results, displayed in Figure 2.10, indicate that more 3D behaviour is present with a larger spacing.

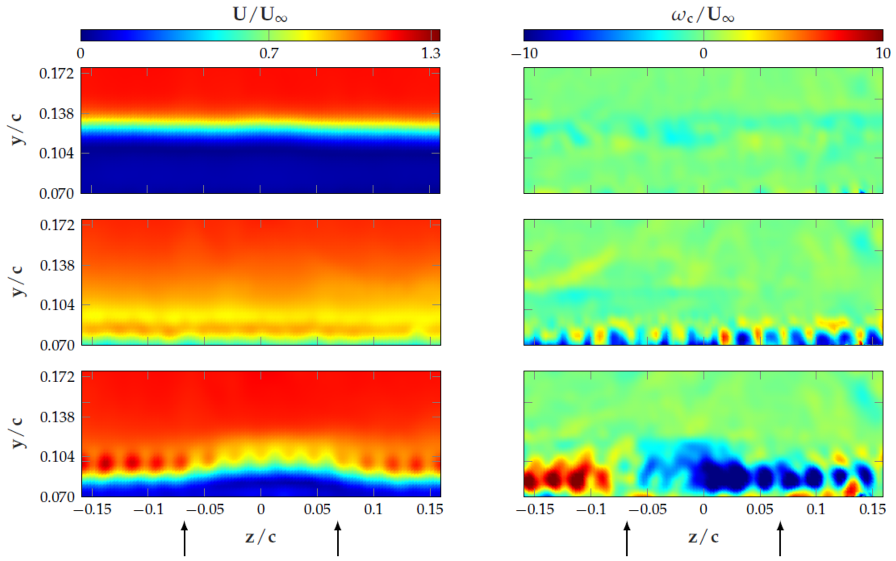

Figure 2.10: Averaged velocity magnitude (left) and vorticity (right) from the work of Borgmann et al. [12]. The fields are recorded with PIV around 75% of the chord for Re = 1.01 million. Top displays the baseline flow field, middle displays an actuated flow field with jet spacing of 0.25 in. and C_μ = 1.1% and bottom displays the field for a spacing of 0.5 in. and C_μ = 2.5%.

The actuation is less uniform and the jets may generate more vortices, more like the operation of an AJVG. When using the tightly spaced jets a C_μ of 0.9% is required, which can be considered low when compared to other references. For example, Puri et al. simulated a NACA airfoil with tangential blowing [13]. Using a small C_μ of 0.6% is ineffective, but 5% did allow for reattachment. Using a simple wall boundary layer, VanSickle et al. [40] proved that the boundary layer thickness can be reduced by half when tangential blowing is used. In recent years, there is also a development in the concept of the Co-Flow Jet. Xu et al. [41] developed a concept where a tangential blowing port at the front of a geometry is supplied by a suction port at the trailing end of the geometry. By pressurising the air between the two ports, separation can be significantly reduced.

Note that for for both the Borgmann et al. and VanSickle et al. cases the jet was inclined by 29° and 20° with respect to the local surface. The practical effect is still considered generally tangential to the flow, due to the Coandă effect. It is thus important to use a shallow angle for the jet relative to the surface, as to allow the Coandă effect to align the blown flow with the boundary layer.

2.3. The aerodynamics of ducts

2.3.1. Nacelle and duct design considerations

In propulsion systems the inlet plays an influential role. In high subsonic flows, the air is slowed by a diverging inlet shape. This is done to reduce the Mach number effects on the propulsion system. In ducted propellers it is observed that the duct inlet provides a suctioning effect and thus thrust [22]. The inlet is also supposed to allow sufficient airflow into the engine or propeller region. This supply is essential as low airflow may reduce the propulsive output of the system, while in extreme conditions it may cause a jet engine to fail or be damaged. To provide proper inflow, thick inlet lips are used. This allows the airflow to stay attached in non-ideal inflow conditions. However, in cruise conditions the thicker lip increases drag.

To optimise the inlet, the distorted inflow has to be managed in some other way. For this purpose, a large body of research has been dedicated to active flow control on nacelle inlets in extreme conditions. VTOL inlets are also part of this research, as the ducts and inlets for VTOL applications operate in very high inflow angles. To quantify the influence of separation on a propulsor, the DC60 factor is commonly used. This is the distortion index at the propulsor plane. It is defined in Equation 2.12, as defined by Hayböck et al. [11]. Additionally the total pressure coefficient is defined in Equation 2.13, in literature it is often plotted to display the local distortion.

$$DC60 = \frac{p_{t,AIP} - \bar{p}_{t,60^\circ,min}}{q_{AIP}} \tag{2.12}$$

$$C_{p,t} = \frac{p_{t,gauge}}{q_\infty} \tag{2.13}$$

AIP means the Aerodynamic Interface Plane, the plane where the flow interacts with the propulsor. The total and dynamic pressures ($p_{t,AIP}$ and q_{AIP}) are related with the lowest averaged, total pressure over 60° ($\bar{p}_{t,60^\circ,min}$). For lower distortion the value becomes closer to 0 as the difference between the 60° pressure and the total pressure reduces. For $C_{p,t}$, a value below 0 implies a loss of total pressure. In separated regions the loss is significant, which will display a local negative $C_{p,t}$. Not only is the pressure distortion a reduction in mass flow rate, the uneven loading on the fan also induces a loss in efficiency of the engine. Mohankumar et al. [2] discussed the loss of performance by inlet separation. Choking losses, rotor-separation interaction and variation of thermodynamic work done by the fan were proven to cause performance loss.

2.3.2. Inlet separation control

In some operating conditions, geometry modifications may not be enough to reduce separation. In Figure 2.4, it can be observed that the X22 ducted propellers operate at a high incidence angle. In these cases separation is sometimes reduced with flow control techniques. On certain systems so called blow-in doors are used, which open to allow more air into the propulsion system. Another option is the use of previously mentioned vortex generators. As they can be very effective, many separation problems are solved with vortex generators. In Figure 2.11, some modification can be noted on the lower lip of the ducted propellers. This is usually where the separation occurs. In a project report of the X22 [27] the modifications seem to be certain types of vortex generators. It indicates that the X22 ducts suffered from separation in the extreme angles they were used. In addition to vortex generators, other flow control techniques have also been applied on inlets.

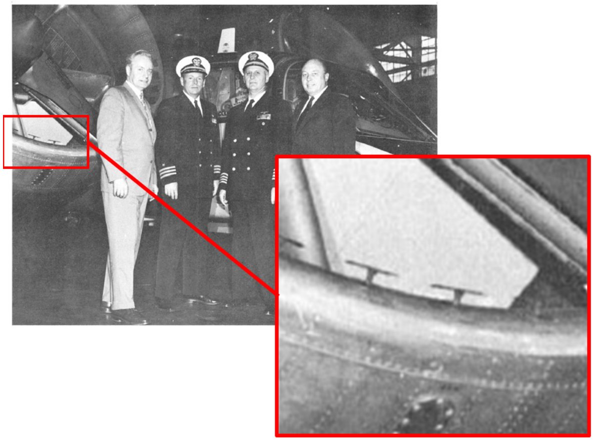

Figure 2.11: Bell X22 acceptance picture, with zoomed in the possible flow control vanes at the ducted propeller inlets. Figure from Bell X22 project report [27], modified by the author.

The AJVG concept has been used to prevent separation on the inside of inlets of ducts and jet nacelles. Erbslöh et al. [4] investigated the separating flow field inside a nacelle inlet. The effectiveness of AJVG and conventional vortex generators were compared. With oil visualisation the surface flow field showed clear 3D behaviour, where the separation region displayed significant flow reversal. The AJVG also proved to be as capable as conventional vortex generators, while having the advantage of being controllable. The system provided a reduction of 40% in DC60 using 10% bleed. To improve the efficiency, Erbslöh et al. [3] optimised the design further, displaying that with 0.1% bleed it is possible to reduce DC60 by 34%. In extreme conditions the AJVG also proved to be effective, as can be seen in the case for crosswinds in Figure 2.12a and Figure 2.12b. The separated region on the duct is smaller in the case with the AJVG. With an array of jets, Wakelam et al. [7] showed that air can stay attached when the airflow was coming in tangentially to the inlet. Even though the pressure ratio required was high, in the order of 10, the effectiveness of the AJVGs is proven.

(a) Oil visualisation on the baseline inlet

(b) Oil visualisation on the AJVG inlet

Figure 2.12: Experiments by Erbslöh et al. [3] discussing the effectiveness of AJVG for a nacelle inlet. The duct is positioned perpendicular to the flow, so conditions are 18 m/s crosswind. The separation shows 3D vortical structures, highlighting the three dimensionality of the problem.

It was also found that oscillating or unsteady jets can increase the efficiency of the control system. Both Nichols et al. and Hayböck et al. presented the applications of AJVG with time dependent actuation. The advantage is that the vortex is still generated, while the jet is not blowing continuously. This reduces the massflow needed for the operation of the AJVG. Nichols et al. [6] discussed the application of this concept to a ramping engine with a varying massflow. It proved effective, only requiring 0.3% massflow required to keep the flow attached. Hayböck et al. [11] tried to optimise the system. It was found that for a particular frequency of oscillating the efficiency, the effectiveness of the jets over the massflow needed, is highest.

In 1979 NASA [10] already investigated the use of tangential blowing on nacelle inlets to prevent separation at high angles of attack. A pressure ratio of 1.4 with 5% bleed mass flow was required to keep the duct separation free. With this input the operational range of the duct was significantly increased. Where previously 61° was the maximum angle before separation, with tangential blowing 110° was possible. In recent years a series of boundary layer blowing solutions were simulated with CFD. Nambiar et al. [8] discussed the effect of blowing with an array of different jet geometry designs. Both perpendicular and angled blowing was simulated, proving that both have separation reducing effects at low pressure ratios (1.1 to 1.3). Certain designs use perpendicular injection, making the jet work as a AJVG. Other designs use more tangential inflow, resulting in a blown boundary layer. It was deemed that the inclined jets were more effective. Benjamin et al. [9] also discuss an array of designs. With the vast number of variables known, the inclination angle was also discussed. It was proven that shallower angles, i.e. more tangential blowing, proved to be more effective than slightly higher angles. Where Nambiar et al. tested with an angle of 45°, Benjamin et al. proved that angles below 30° were more effective. For the crosswind conditions in their analysis reattachment was possible. In the investigation, which discussed more designs for the jetting slot, the 30° design proved to be very effective. The effect of the blowing slot on the streamlines over the surface is presented in Figure 2.13b. Compared to Figure 2.13a it can be seen that fully attached flow is possible. It can be concluded that tangential blowing is a viable separation control mechanism.

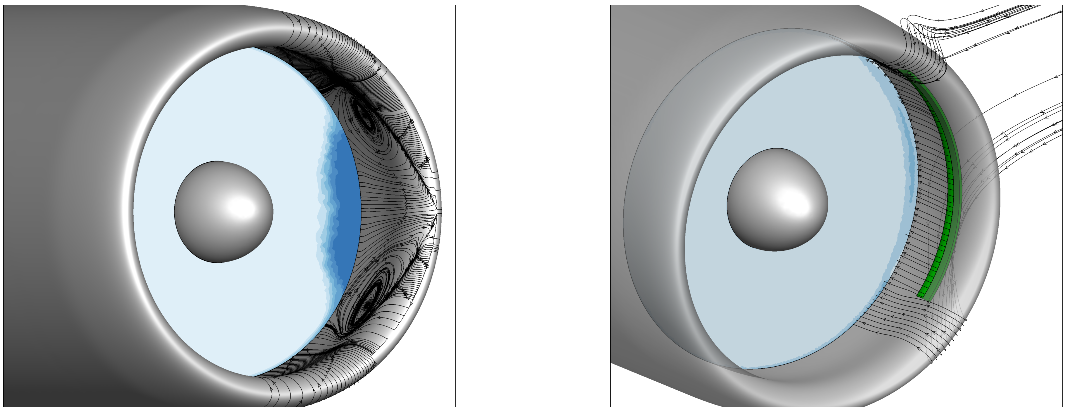

(a) Surface streamlines for the baseline inlet **(b)** Surface streamlines for the tangentially blown inlet

Figure 2.13: A numerical analysis by Benjamin et al. [9] discussing the effectiveness of tangential blowing on a nacelle inlet. The nacelles are in crosswind conditions, inducing significant separation and flow reversal on the baseline inlet. With adequate jetting velocity, the distorted region can be reduced.

Although active flow control has not been applied to a duct or nacelle on the market, patents for the system have been filed. Airbus [42] filed a tangential blowing system for the diffuser section of a nacelle inlet. United Technology Corporation [36] has filed a patent in which an active flow control system on a nacelle inlet is supplied with air from the high pressure compressor. This would be similar to the system of interest in this thesis. However, in this thesis the high pressure air would be bled from behind the propeller.

2.4. Project scope

2.4.1. Conclusions from literature

In conclusion, the performance of a propeller can be improved with the utilisation of a duct. Especially at highly loaded conditions the performance can be enhanced [20]–[22], [43]. Open propellers lose the load at the tip of the propeller, while the duct prevents leakage on a ducted propeller. With this process the ducted propeller can be more tip loaded and can produce more thrust. Since an open propeller is less tip loaded, conventional designs take this into account. So, the addition of a ducted propeller benefits from a modified, tip loaded propeller. In recent years, the interest in ducted propellers has risen as it is a viable option for (e)VTOL applications and possible performance improvements on propeller aircraft. Previous wind tunnel experiments thus become relevant as sources of data. A particularly interesting reference case is the propulsion system of the Bell X22. Introduced in 1966, it has been a test bed until the 1980's. The system proved to be a very well documented ducted propeller, allowing for adequate validation during this thesis. Additionally, it can be argued that flow separation was a problem for the operation of this ducted propeller, as flow control was applied. This thesis would present an alternate solution to the separation problem encountered on this duct. Although the system was applied to a VTOL aircraft, the flow control technique can be tested on this design.

It has been observed that duct inlets can exhibit separation under high angle of attack conditions. In practice, the inlet lips are given a larger radius to prevent separation. Certain flow control mechanisms have been used to prevent separation. In literature some of these techniques have also been used on nacelle inlet, with the goal of allowing the duct inlet to be optimised for cruise. As discussed, vortex generators are effective, but are uncontrollable. Therefore active flow control systems are of interest as these can be disabled when not needed. The AJVG delivers good results, with attachment improved even in pure crosswind conditions. Postponement of separation is done with efficient jets, causing vortices which mix the boundary layer and core flow effectively. A possible drawback could be that the vortices interact with airflow downstream and thus also with propellers and turbomachinery downstream. Tangential blowing energises the boundary layer, also delaying separation. In this process no vortex is used to mix the boundary layer. It thus benefits the boundary layer without the drawback of introducing vortices in the flow. This process does require more momentum addition through the jets.

2.4.2. Hypotheses

Literature proves the effectiveness of boundary layer blowing on a separation in an inlet. In the discussed papers, the jet was either controlled with supplied pressure or set as a boundary condition in CFD. If the system was applied to a propulsion system, it would require a higher pressure supply of air. In a turbomachine this can be done at the cost of increased complexity. In a ducted propeller system the bleed air can be taken from behind the propeller. As pressure is added by the propeller, the flow field behind the propeller has a higher pressure.

The hypothesis in this thesis is that a bleed line from behind the propeller can supply enough pressure to a tangential blowing jet. In theory this would allow the high pressure air to energise the boundary layer without an active flow control system. The bleed line would be a geometric design, which would make the system a form of passive control. This passive system is named the passive tangential blowing system or PTB for short. The aim of this research is to analyse if this form of passive control can reduce distortion on ducted propeller. The objective is to analyse the effectiveness of tangential blowing in preventing separation on a ducted propeller by being linked to a bleed line behind the propeller with the use of CFD in subsonic flow. The discussed system is presented in Figure 2.14a.

For the analysis of this problem, CFD is used. It was discovered that certain regions of separation on the duct presented temporal behaviour. Therefore, the simulation were run a URANS solver, with the propeller simulated by a fan boundary. It can be expected that the CFD setup presented in this thesis performs different than a more high fidelity model would. As the boundary layer on the duct inlet is of relevance, refinement is placed locally. It can thus be expected that the local flow field should be found accurately. The influence of a propeller model would present a different pressure distribution compared to reference data. The degree to which this is different is unknown and will be discussed in the validation chapter.

The supply of air from behind the propeller can be achieved with a flush port or a ram port. A flush port would be flush with the local surface and can only bleed off static pressure. A ram port is directed into the flow, allowing total pressure to be bled off. It is expected that the flush port operates more stable as it is not relying on ram air. If the ram port experiences a separation region, it may display a significant reduction in total pressure. This would reduce the momentum addition available, thus increasing the separation and yielding even less pressure on the ram port. A flush port that is located in the separated region is not effected by this problem as much. With an increase in thrust it can be expected that both the flush as well as the ram system operate more effectively as the pressure on the ports is increased. In Figure 2.14b the flush and ram ports are indicated. Both are located behind the propeller, the flush port being flat on the duct surface and the ram port being perpendicular to the surface. The position of channel is illustrated, with the flow bled through the flush and ram ports and jetted through the slot.

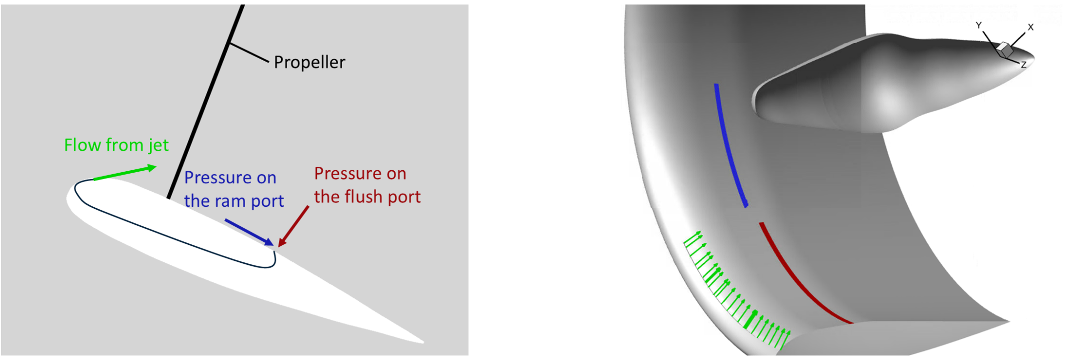

(a) Flow bled and jetted by the channel concept

(b) The chosen positions of the ram (blue) and flush (red) ports

Figure 2.14: A schematic approach of the link between the jet and bleed ports, from the setup of the author.

2.4.3. Research questions

The main research question for this thesis is as follows. To what extent can bleed air delay separation through tangential blowing on the ducted propeller of the Bell X22 in a high angle of attack situation in a temporal CFD simulation? To find the answer to this question, a group of subquestions is introduced:

- To what extent is a CFD simulation with an actuator disk in a ducted propeller accurate with respect to test data?
- How is separation influenced by tangential blowing before the separation point?
- How effective is tangential blowing if the air is bled with a flush port from behind the propeller?
- How effective is tangential blowing if the air is bled with a ram port from behind the propeller?
- How does the effectiveness of the passive tangential blowing system vary with the higher thrust setting on the propeller?

3
Methodology

A description of the methodology is given in this chapter. Since there is a mixed usage of high and low fidelity models, both will be discussed here. In the numerical setup the propeller will be modelled by a virtual disk or fan boundary condition. This would allow for a prescribed pressure, which will be discussed in section 3.1. A similar simplification is done for the passive bleed line, where momentum can be extracted from behind the propeller to the inlet. To exclude meshing of the entire channel, a equation model is introduced in section 3.2. The assumptions and the justification of these assumptions are mentioned in section 3.3. The high fidelity CFD, done with Ansys Fluent, will be first discussed in the analysis of a simpler reference case in section 3.4. As this case also discusses the concept of momentum addition to the boundary layer, the numerical setup here would also work well as a basis for the further ducted propeller setup. The CFD setup of the ducted propeller will be discussed in section 3.5. Since there is an inherent difference between the two, the 2D and 3D setups are discussed separately.

To ensure consistency in nomenclature, the design of the duct should be discussed. In Figure 3.1 the chosen naming convention is presented. A simplified duct is used in this thesis, so no structural parts are part of the analysis.

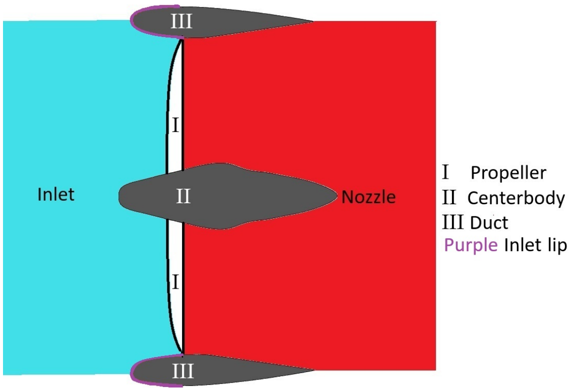

Figure 3.1: Naming convention used in this thesis, work by the author

The naming has been chosen as it is most consistent with literature nomenclature and other applications in this thesis. The naming of centerbody is consistent with the low-fidelity model that will be discussed later [44]. The inlet lip is highlighted as further discussions will be focussing on the lip, both in the results chapter as well as in the setup discussion.

3.1. Pressure jump prediction

The propeller in this setup will be modelled with a fan boundary condition. It is an internal boundary condition onto which a pressure jump is prescribed by the user. With the functions in Fluent, one can vary the pressure jump with respect to the radial position on the propeller. This pressure jump can be calculated with low fidelity models, so no full propeller has to be simulated in CFD. This reduces the complexity of the simulation, thus reducing the computational effort. Simply stated, this thesis is only interested in if the propeller can supply the passive system with enough pressure differential. The swirl induced by a propeller is therefore not of interest, as it is not aligned with the flush and ram ports.

Additionally, Nederlof et al. [45] found that the tangential velocities are much smaller than the axial velocities in the slipstream of the propeller. This implies the effect of swirl on the pressure field is small. Assuming no swirl is present allows the setup to use a prescribed pressure jump over the fan boundary condition. Stich et al. [46] proved for NASA that the use of an actuator disk requires only 2% of the computational power of a fully sliding mesh. Note that this is for a fan engine with more blades than the propeller in this paper, meaning this number may be lower for this case. The conclusion is that the use of a disk rather than a meshed blade greatly reduces computational effort required. Further analysis of the implication of this assumption can be found in section 3.3.

3.1.1. Low fidelity model comparison

For propeller modelling there are a number of low fidelity options, two of which will be discussed and compared in this subsection. As discussed in section 2.1, a well-known model is the BEM. A limitation of this modelling is the unmodelled 3D effects on a propeller. In practice BEM simulations use the Prandtl tip and root corrections, as discussed before. JavaProp [47] is a free, often used BEM program. It returns very detailed information at low computational effort. To model a ducted propeller it is equipped with an options to add a shroud. This sets the tip loss factor to 1, which is the theoretical effect of the duct on the propeller. It therefore can model a ducted propeller, but it cannot model the duct or spinner. This is a limitation of the software. These limitations are known from the user's guide by Hepperle [47].

Another program has been developed at MIT. The Ducted Fan Design Code (DFDC), created by Drela et al. [44], uses a lifting line model to model the propeller, while using a panel method for the surfaces of the centerbody and duct. With this enhanced method the entire ducted propeller system is modelled. This allows for accurate results from this low fidelity model. Extracting the pressure rise across the propeller is more difficult than for JavaProp, which presents the pressure jump directly. For each annulus along the radius of the ducted propeller DFDC calculates the rise in total enthalpy (ΔH) and rise in kinematic entropy (ΔS). In the theoretical background report for DFDC, Drela et al. [44] pose the following equation for the rise in total pressure:

$$\Delta p_t = \rho(\Delta H - \Delta S) \tag{3.1}$$

To compare DFDC and JavaProp, a Python wrapper was created to extract the data from DFDC and calculate this pressure jump.

3.1.2. Pressure jump comparison to reference cases

The geometry of the X22 ducted propeller was retrieved from Mort et al. [19] and analysed with JavaProp and DFDC. For a range of advance ratios the thrust and power coefficients were plotted. For both, the reference value from the wind tunnel test [19] is added as well. Note that for both Figure 3.2a and Figure 3.2b the rotational rate was kept at 1200 RPM. This rotational rate is chosen as it is indicated by the source that the experiments were performed between 1200 and 2590 RPM with an additional varying dynamic pressure inflow.

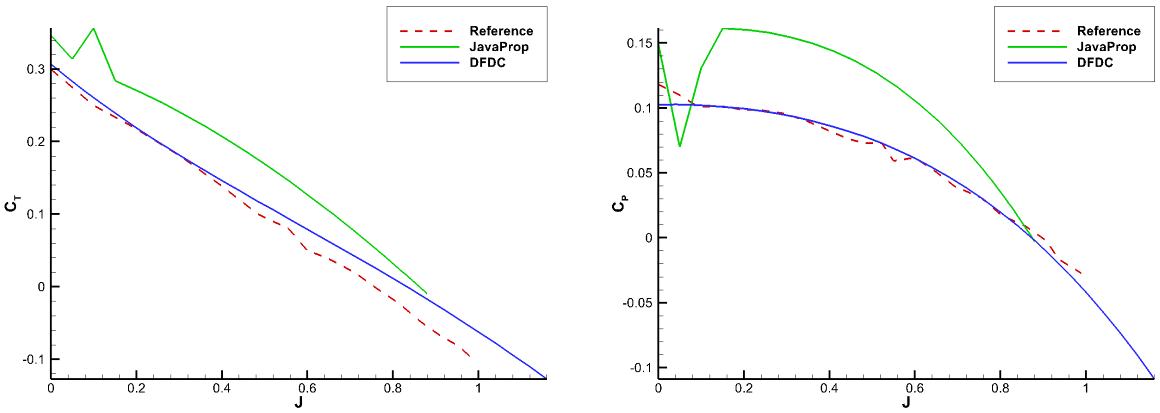

(a) Thrust coefficient vs advance ratio for the X22 propeller at 1200 RPM.

(b) Power coefficient vs advance ratio for the X22 propeller at 1200 RPM.

Figure 3.2: Performance of the X22 ducted propeller for 1200 RPM. The reference data is from wind tunnel tests [19], while the DFDC and JavaProp analyses are performed to discuss their accuracy. From these analyses DFDC seems to provide accurate results.

It can be seen that the JavaProp approximation is less accurate than the DFDC output. Inherently there is a thrust difference as the duct is not modelled in JavaProp. In addition to this, the power coefficient is also less accurate when using JavaProp.

To validate the operation of these pressure jumps, it was determined to perform a validation study with a well documented reference case. A full XPROP propeller with a circular wing was simulated in CFD by Bento et al. [17]. It was used as a reference case and the geometry of the duct and the propeller were loaded into JavaProp and DFDC. To create a reference pressure distribution the solution used in the paper was received from Bento. The simulation used a sliding mesh and a rotating domain to create the motion of a rotating propeller. For three different azimuthal positions the radial total pressure distributions were exported. This was done in front of the rotating domain and also behind the rotating domain. The distribution at the front was averaged, as it was expected that there was not be much effect of the propeller on total pressure upstream. Subtracting this averaged radial distribution from the pressures behind the propeller yields the total pressure rise. In Figure 3.3 these three pressure distributions are plotted as Δp1, Δp2 and Δp3.

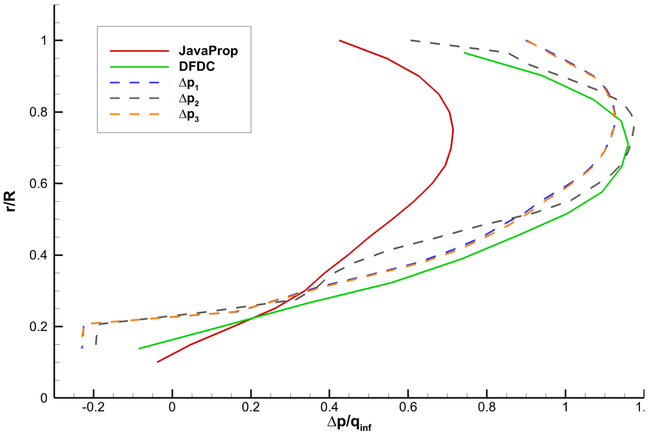

Figure 3.3: Pressure distribution from CFD, JavaProp and DFDC

These pressure distributions clearly indicate that DFDC is closer to the high fidelity CFD than JavaProp. Another interesting note is that the pressure integrated over the radius should equal the thrust. For DFDC this is congruent, while for JavaProp the data shows an inconsistency. The integrated pressure does not equal the thrust predicted, it is lower by a factor of 2. It was concluded that the pressure jump prescribed by JavaProp is incorrect. DFDC will thus be chosen as the low fidelity model for the fan pressure jump.

3.1.3. Fluent pressure jump implementation

Ansys Fluent is equipped with the fan boundary condition. This is an internal boundary condition between two regions and applies a pressure jump to the flow from one to another zone. The jump is a static pressure jump, as an actuator disk does as well. It is directed normal of the fan boundary, which can be in either upstream or downstream direction. The pressure jump can be related to inflow to the boundary condition, but Fluent does not allow the pressure jump to be variable with radius. By creating a Named Expression for the radius, the pressure jump can be related to the radial position. For any position in space, the radial position was calculated in Fluent with the following equation:

$$radius = \sqrt{(x - x_{center})^2 + (y - y_{center})^2 + (z - z_{center})^2} \tag{3.2}$$

Note that this equation determines a radial position for all locations in the numerical domain. The pressure jump is thus also calculated for all positions in the numerical domain, however it is only applied at the fan boundary. With the radius defined the pressure jump can be related to the radius. From DFDC the pressure jump per annulus is exported with the Python wrapper. A fourth order polynomial was then used to fit the pressure jump. The coefficients of this polynomial can be exported into Fluent. Whenever DFDC is used to prescribe a pressure distribution, the fitted polynomial is always plotted to validate its accuracy. In Figure 3.4 the polynomial is indicated by the Polyfit line. Note that this loading condition is taken from reference material and will be used as a loading of interest [25]. Dimensional values are used as this polynomial is directly exported to Fluent.

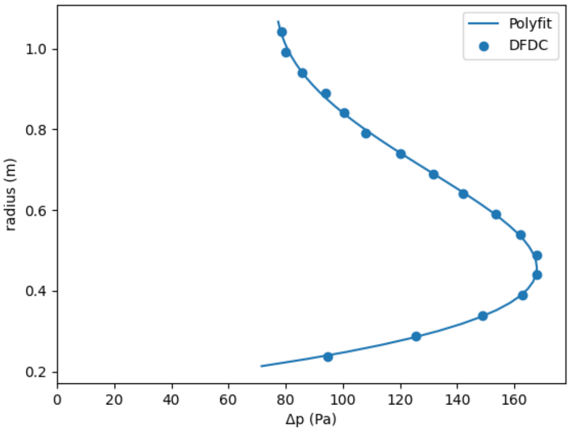

Figure 3.4: Pressure distribution on the propeller as described by DFDC and with the polynomial fitting in Python. With a fourth order polynomial the distribution as found by DFDC can be accurately approximated, requiring only a limited amount of coefficients to be exported to Fluent.
v_∞ = 13 m/s, α = 40°, J_∞ = 0.522, $\theta_{0.75}$ = 19°

The pressure jump can be approximated with the polynomial. The low fidelity model DFDC can model the propeller and calculate the pressure jump. With a polynomial, the pressure jump can be prescribed on the fan boundary condition in CFD. This allows for the simulation of a ducted propeller without the need for simulation of the entire propeller blade.

3.2. Bleed line flow

The concept of interest for this thesis is the flow control system using bleed air from behind the propeller. Simulating this bleed flow can be done with CFD, which would require a fine mesh in the bleed channel. However a simplified channel flow equation may prove to be as effective and can greatly reduce the simulation complexity. Pipe flows are well-understood and can be modelled rather simply, yet effectively.

3.2.1. Channel equation derivation

In Figure 3.5 a simplified channel can be found. It consists of the jet, a position 1 and a position 2. Position 1 is the bleed port. Position 2 and the bleed port have the same height h, while the jet has a height of h_j.

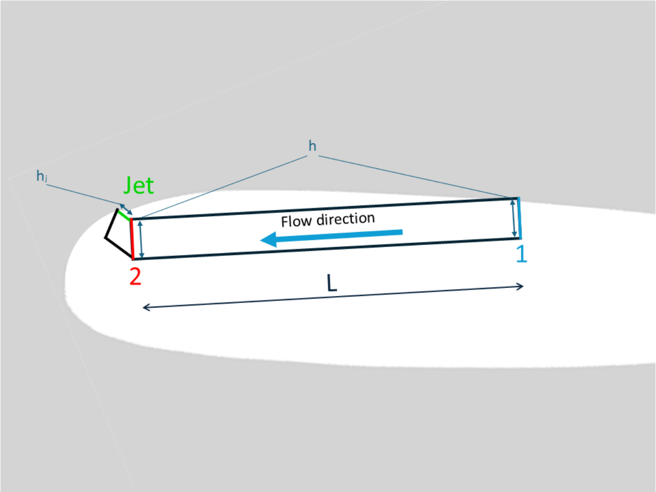

Figure 3.5: A simplified schematic of the channel flow. This diagram created by the author was used to derive the pressure loss in the channel. Note that this illustration is for a 2D channel, a 3D channel would have a width as well.

With this schematic a simple derivation can be performed. A few assumptions must first be made: firstly, the flow will be considered incompressible. Secondly, friction is only applied to the section between positions 1 and 2. Between position 2 and the jet the distance is shorter and therefore considered negligible. From Newtons first law it can be written:

$$p_1 A_1 - p_2 A_2 = \frac{1}{2} A_w C_f \rho v^2 \tag{3.3}$$

The pressures p_1 and p_2 are the static pressures at positions 1 and 2. Since the channel is the same size from 1 to 2, the cross-sectional areas $A_1 = A_2$ and the velocity in the channel v must be the same from a continuity principle. The cross-sectional area is the channel height h multiplied by the channel width cc. The wetted area A_w is twice the channel width, which is the circular length cc multiplied by the channel length L. The friction coefficient C_f will be defined later.

$$(p_1 - p_2) h cc = \frac{1}{2} cc L 2 C_f \rho v^2 \tag{3.4}$$

$$(p_1 - p_2) h = L C_f \rho v^2 \tag{3.5}$$

Any pressure tapped from the bleed port, will become the total pressure at the position 1. Bernoulli's equation has to be applied to find the static pressure. At the jet, the static pressure p_j acts as a back pressure on the channel. Both the Bernoulli equation and the continuity equation need to be used to solve the entire problem. For the continuity, the height at position 2 is h and the height of the jet is h_j.

$$p_{t,2} = p_2 + \frac{1}{2}\rho v^2 = p_{t,j} = p_j + \frac{1}{2}\rho v_j^2$$

$$p_2 = p_j + \frac{1}{2}\rho v_j^2 - \frac{1}{2}\rho v^2 = p_j + \frac{1}{2}\rho((\frac{h}{h_j})^2 - 1)v^2$$

Combining this into (3.5) yields the following equation:

$$(p_{t,1} - \frac{1}{2}\rho v^2 - p_j - \frac{1}{2}\rho((\frac{h}{h_j})^2 - 1)v^2)h = (p_{t,1} - p_j - \frac{1}{2}\rho(\frac{h}{h_j})^2 v^2)h = LC_f \rho v^2$$

$$p_{t,1} - p_j = (\frac{LC_f}{h} + \frac{1}{2}(\frac{h}{h_j})^2)\rho v^2 \tag{3.6}$$

Using the continuity equation again allows for a relation from v to the jet velocity v_j. This velocity can be used in Equation 3.10 and so the pressures behind the propeller and at the jet can be used to find the momentum addition.

3.2.2. Validate channel equation

To validate the channel equation, one can implement the concept of the hydraulic diameter. This is defined as the ratio of the area A to perimeter P times 4. The area is the cross-sectional area as defined previously, while the perimeter is twice the width plus twice the height. The height is ignored here, as it is negligible with respect to the channel width.

$$D_H = 4\frac{A}{P} = 4\frac{h * cc}{2h + 2cc} \approx 4\frac{h * cc}{2cc} = 2h \tag{3.7}$$

Implementing this in (3.5) yields.

$$\frac{(p_1 - p_2)D_H}{2} = \frac{\Delta p D_H}{2} = LC_f \rho v^2 \qquad \frac{\Delta p}{L} = \frac{2C_f}{D_H}\rho v^2 = \frac{4C_f}{D_H}\frac{\rho v^2}{2} \tag{3.8}$$

From TU Delft Open Courseware the following equation can be found [48]. This equation is known as the Darcy-Weisbach equation and predicts pressure loss through a pipe.

$$\frac{\Delta p}{L} = \frac{f}{D_H}\frac{\rho v^2}{2} \tag{3.9}$$

f is known as the Darcy friction coefficient. Comparing (3.9) and the derived equation (3.8), it can be seen that $f = 4C_f$, meaning the friction coefficient used in this thesis is a quarter of the Darcy friction coefficient. From the Moody diagram, the Darcy coefficient can be found. With this result the channel flow equation is validated, as further development is simply an application of the Bernoulli equation for incompressible flow.

3.2.3. Channel equation variable sensitivity

With the bleed model complete it can be investigated which parameters have effect on the performance of the bleed system. A number of parameters are limited and do not vary or are considered invariable. The geometric distance between the bleed port and the jet fixes L. Depending on the position of the bleed port L can vary, but it can never be more than the length of the low duct, this being 1.24 m. In practice L is in the order of 0.4 to 0.6 m. The density of the fluid ρ is fixed as the flow is considered incompressible. The friction coefficient is considered a constant number. The relative roughness factor was estimated to be of the order of 10^{-5}, which was found by using an roughness height ϵ of 0.0025. The accuracy of this estimation is of lower relevance, because the equations yield a Reynolds number in the pipe of $2 * 10^4$. At this point in the Moody diagram many relative roughness lines coincide. The Darcy friction coefficient f is then found to be 0.03. It was later found that this was applied incorrectly and f was used as C_f, yielding a higher applied friction coefficient. This should be noted, but the implications of this error are relatively small. The result is that the element $\frac{LC_f}{h}$ is of low effect on the short bleed line.

This implies that there are three main parameters of influence. Firstly, there is the jet height h_j, which is directly related to C_μ through Equation 3.10 as it determines the mass flow rate $\dot{m}$. The second parameter of influence is the relative bleed port height $\frac{h}{h_j}$. The third parameter of influence is the differential pressure between the jet and bleed port $p_{t,1} - p_j$. Note that this last parameter is dimensional. To non-dimensionalise this number, the differential is divided by the dynamic pressure upstream in the CFD simulation. This yields the non-dimensional differential pressure coefficient ΔC_p. Figure 3.6 displays the momentum coefficient as a function of relative bleed port height for various differential pressure coefficients. Note that this figure is for a jet height of 5 mm, which is the slot height that will be used during the ducted propeller simulations.

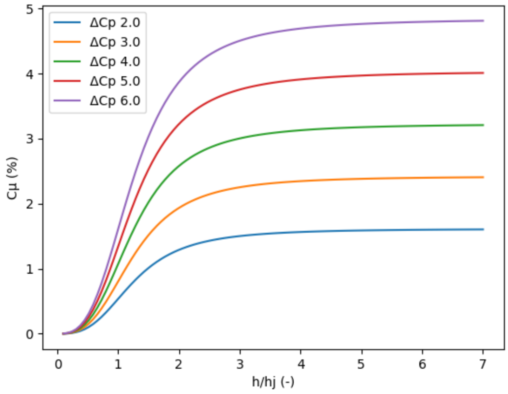

Figure 3.6: C_μ as a function of slot height for various differential pressures. From analyses presented in chapter 5 it can be seen that the pressure differential is in the order of the values presented in this figure.

In Figure 3.6 it can be seen that the rise in momentum coefficient is not as steep for a higher relative bleed height. It is thus concluded that there is no added benefit of increasing the relative port height $\frac{h}{h_j}$ above 5. The differential pressure is a result of the flow field in the CFD solution. In conclusion, the bleed port height shall be set at 5 times the jet height as a bigger bleed port does not seem to enhance the performance significantly.

3.3. Assumptions

In the simulations for the ducted propeller presented in this thesis a number of assumptions have been made. In section 6.2 the validity of these justifications is reviewed. Note that the simulations of the NACA airfoil are done with the same assumptions as used by Puri et al. [13].

Firstly, there is the state of the flow. Since low velocity magnitudes are expected, the flow will be considered incompressible. Low Mach numbers of below 0.3 indicate that this assumption is considered valid. Above this Mach number the flow can be significantly impacted by the compressibility effects. The flow is in sea-level conditions, meaning ISA sea-level conditions. The resulting density and speed of sound are also used. With the operating velocity between 13 and 60 m/s and the duct length being 1.24 m, the Reynolds number is above 1 million. This is of the same order of magnitude as at which external flow in the aerospace industry occur. At the leading edge of the duct, laminar flow can be present. A large part of the flow is expected to be turbulent under these conditions.

The second major assumption lies in the modelling of the propeller. As has been discussed, the propeller will be modelled using a fan boundary condition, creating a virtual disk to represent the propeller. As swirl is of no interest to this flow problem at hand, the simplification of the propeller was added. It allows for a reduced computational complexity and thus less computational effort required during the simulation. The fan boundary condition does bring the problem of the propeller tip gap. Due to the presence of the boundary condition, a jump in pressure is sudden. The tip gap does not gain a pressure jump as no propeller is present. This will mean that locally the airflow on the duct is experiencing a severe adverse pressure gradient and could present separation. This concept will be discussed as fan-induced separation.

3.3.1. Tip gap assumption

The CFD results in 2D present the effect of fan-induced separation. An attached flow may be forced to separate by the adverse pressure gradient, as can be seen in Figure 3.7c. In a ducted propeller at an inflow angle, the local boundary layer is moving into an adverse pressure gradient naturally. This means that the flow is low in momentum and the induced adverse pressure gradient has a significant effect on the prediction of the separation point. The difference can be seen clearly in Figure 3.7a and Figure 3.7b. With a open tip gap the separation is induced at the fan surface. A close-up of this phenomenon can be found in Figure 3.7d. In green the fan boundary is indicated for reference.

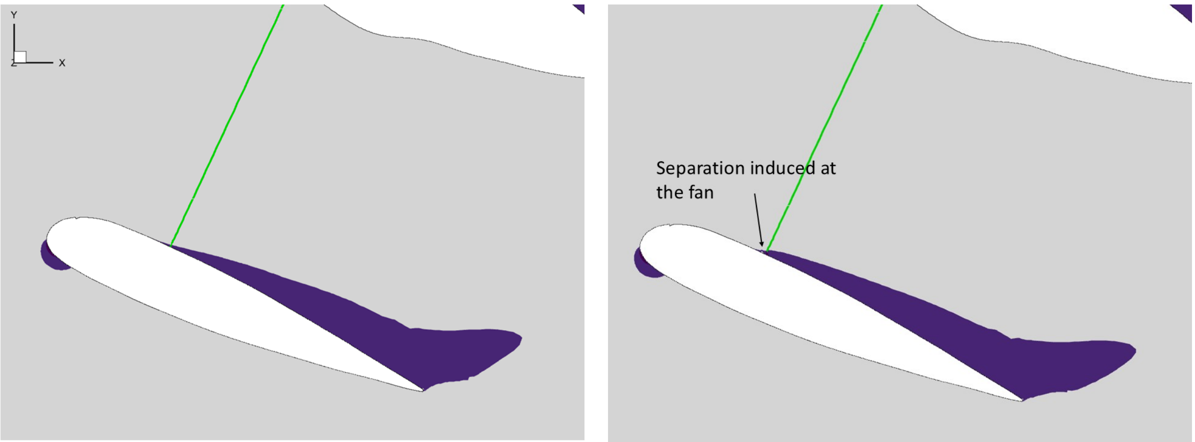

(a) Attached flow through the fan without tip gap

(b) Separated flow on the fan with tip gap

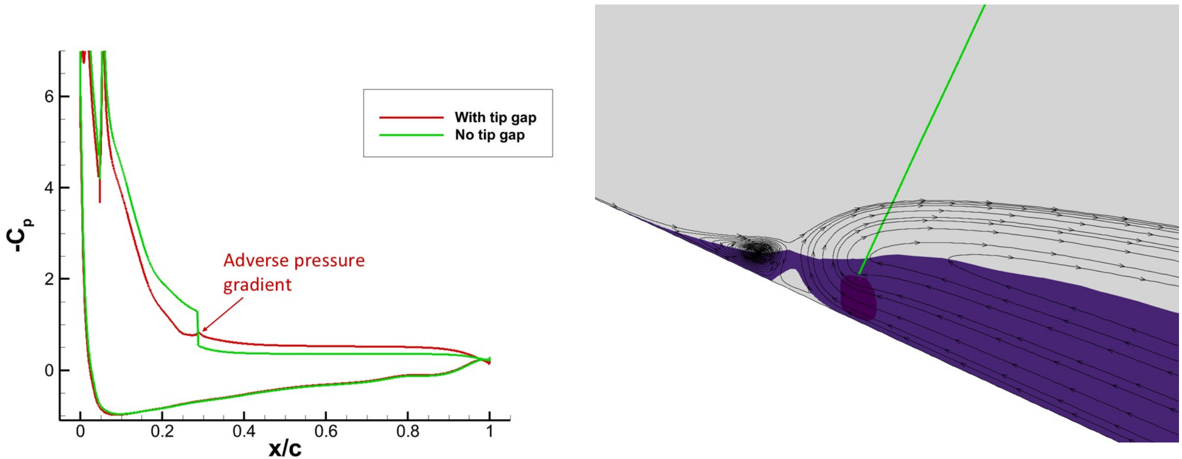

(c) Pressure distributions on the lower duct for the X22 duct

(d) Close-up of the separation on the fan boundary. This indicates an unrealistic flow.

Figure 3.7: Effect of the tip gap applied to the fan boundary condition on the blown ducted propeller. The figures are from the 2D analysis of the X22 ducted propeller. The green line in the flow field indicate the location of the fan boundary.
α = 25°, v_∞ = 13 m/s, J_∞ = 0.522, C_μ = 5%, $\theta_{0.75}$ = 19°

Akturk et al. [49] indicate that at ducted fan with a large tip gap, the axial velocity around the duct surface is significantly lower when compared to a case with a smaller tip gap. The passing blade induces a large pressure gradient, causing tip leakage. This is a local occurrence, at the tip of the blades where the pressure and suction side coincide. As an actuator disk models the propeller without blades, this phenomenon cannot be simulated accurately. The separation due to a passing blade is not the separation effect this research focuses on. Akturk et al. describe the difficulty in modelling this interaction lies in the combination of the tip vortex, the boundary layer on the duct and the wake of the propeller. It is thus determined that this flow interaction is not of interest and the tip gap will be ignored for further simulations. Note that this may have an upstream effect on the point of separation on the duct. This will be further discussed in chapter 4.

3.4. Simple airfoil case

As the ducted propeller will develop a complex flow, it requires a setup that captures this flow behaviour. To establish an accurate setup for tangential blowing, a simpler case was analysed to start with. Puri et al. [13] discuss in their 2018 paper the effect of tangential blowing on a NACA 0018 airfoil. This thesis replicates this case to validate the setup. The measure for the momentum addition is known as the momentum coefficient and is defined as:

$$C_\mu = \frac{h_j v_j^2}{\frac{1}{2} c v_\infty^2} \tag{3.10}$$

The simulation is run with steady RANS 2D settings, with an airfoil of 1 meter long. While the velocity and the Reynolds number of 250,000 are lower than for the ducted propeller of interest, other flow characteristics are similar. Both cases are in incompressible flow with low Mach numbers. Both this airfoil and the inside of the duct will be analysed in conditions with separation present. For this airfoil the leading edge separation occurs at an angle of attack of 15°, which is lower than for the duct inlet. It is therefore assumed that a setup that can capture the flow behaviour of this NACA foil, can also capture the flow behaviour on the duct. The setup from the NACA case will be used as a basis for the 2D ducted propeller setup.

3.4.1. Numerical setup

The flow around the airfoil will have a mainly streamwise component. Even in the separated condition, the flow around the separated region will be streamwise. For this reason it was decided to create a structured, predominantly quadrilateral mesh. It is important to align the mesh with the dominant flow direction. The numerical stability is enhanced when the simulated flow aligns with the mesh. The advantage of a structured, quad mesh is that fewer mesh elements are needed to capture the flow phenomena accurately. Puri et al. [13] use an unstructured mesh in their analysis, as their analysis was set up with a plenum to supply air to the blowing slot.

The numerical domain was set with a circular inlet and a straight outlet. The velocity inlet has a radius of 15 times the chord length, while the pressure outlet is set 20 chord lengths behind the leading edge of the airfoil. This can be seen in Figure 3.8a. The top and bottom of the numerical domain also function as a velocity inlet boundary condition, with the velocity prescribed along the axial direction. In the wake of the airfoil, a refinement is added. This refinement is linked to the angle of attack of the airfoil. The blue zones in Figure 3.8b indicate the wake refinements. Finally, the wake of the jets also have a refinement. Indicated in green in Figure 3.8c, these refinements are used to locally to refine the mixing between the boundary layer and the jet flow.

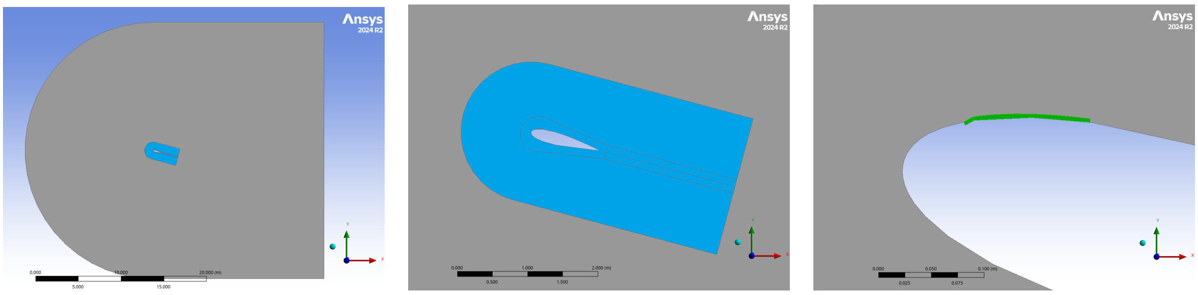

(a) Entire numerical domain, with velocity inlets at the left, top and bottom

(b) Refinement zones along the wake. Note the alignment with the wake direction

(c) Refinement zone on the front jet, also present on the second jet on the airfoil

Figure 3.8: NACA 0018 numerical domain setup used by the author to establish a basic setup for tangential blowing. The modified NACA foil is the same as used by Puri et al. [13].

3.4.2. Mesh setup

The meshing is done with the Fluent mesher. It is equipped with pre-programmed mesh workflows, one of which is specifically made for 2D simulations. This workflow also follows the order in which the mesh operations are performed. It is thus important to structure the workflow such that the desired mesh is generated. As the momentum addition is done with a jet slot, the mesh should also capture the local flow behaviour very accurately. It was thus assigned to be created first, after which the rest of the prism layer is built which can be seen in Figure 3.9c. The refinement in the wake is then meshed on top of this prism layer, which is displayed in Figure 3.9b. The rest of the numerical domain mesh is displayed in Figure 3.9a.

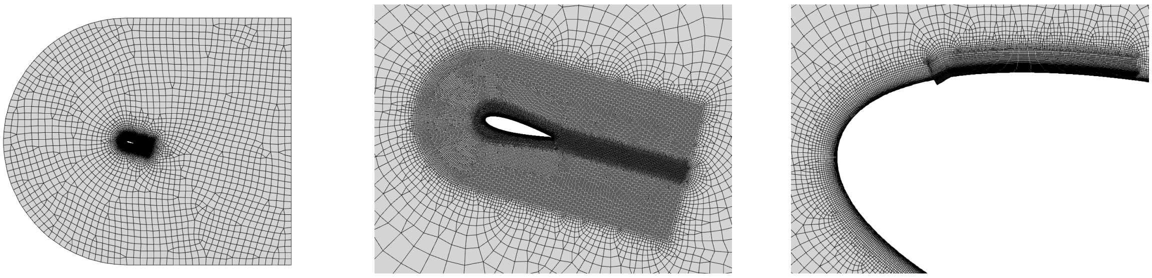

(a) Numerical domain **(b)** Refinement zones **(c)** Surface

Figure 3.9: NACA 0018 mesh setup

3.5. CFD setup

To analyse the concept of the passive tangential blowing more effectively, it was decided to first analyse the system in 2D. The limitations of the chosen setup can be discussed and the mesh setup can be prepared for the 3D case at reduced computational cost. Certain parameters, such as operational advance ratio and upstream velocity, can also be determined as to limit the number of simulations required in the 3D analysis. It also gives an initial idea about the performance of the passive momentum addition system. It must be mentioned that the analyses done are performed for the ducted propeller of the X22. This system is designed to operate in VTOL conditions, which will be noticeable in the angles of attack that will be discussed. These angles is not similar to a ducted propeller or nacelle for an axial flight regime. The setup as well as the results discussed in this thesis may not be directly comparable with more axial applications of the ducted propeller system.

3.5.1. 2D setup

The numerical domain can be fitted with refined zones where flow of interest could be present. A similar numerical domain as for the NACA analysis was chosen. The inlet circle is positioned 12.5 times the propeller diameter upstream and the outlet is 25 times this length downstream. The origin of the numerical domain is the centre of the propeller disk. The refinement zones are set up in such a way that there is high resolution in the slipstream of the ducted propeller. A finer refinement zone is positioned around the entire ducted propeller and moves with the angle of attack of the propeller. The geometry of the ducted propeller was reconstructed from technical reports [19]. The struts and deflection fin were not added and the centerbody was modified to reduce the separation induced by its shape.

As discussed, the mesh and the mesh settings of the NACA 0018 setup were used to create the mesh for the ducted propeller, as can be seen in Figure 3.10a and Figure 3.10b. Due to the difference in operating velocity, the near wall thickness for the ducted propeller had to be lowered. This was done to guarantee a low wall $y+$ of no higher than 2 and generally lower than 1. Additionally, the surface mesh on the bottom duct had been refined. This is done to properly capture the reaction of the boundary layer to the momentum addition and adverse pressure gradient. The interesting part of the simulation is present on the lower duct, the upper duct and spinner do not need this refinement, as can be seen in Figure 3.10c. A prism layer has been added to the propeller disk to capture the jump across the fan effectively. Further mesh settings are very similar. In total this yields a mesh cell count of 343,000.

It must be noted that the 2D simulations were solved with a steady RANS solver. This proved to be an incorrect setup. Part of the separation on the duct, especially on the top outside, has an unsteady behaviour and therefore cannot be solved with steady RANS. On the lower duct the separation is steadier. The reached convergence with the steady solver was $1e-3$, while the convergence criterion was set at $1e-5$. Due to the low convergence, no final conclusions will be taken from the 2D simulations. Notes relevant for the 3D simulations will be discussed.

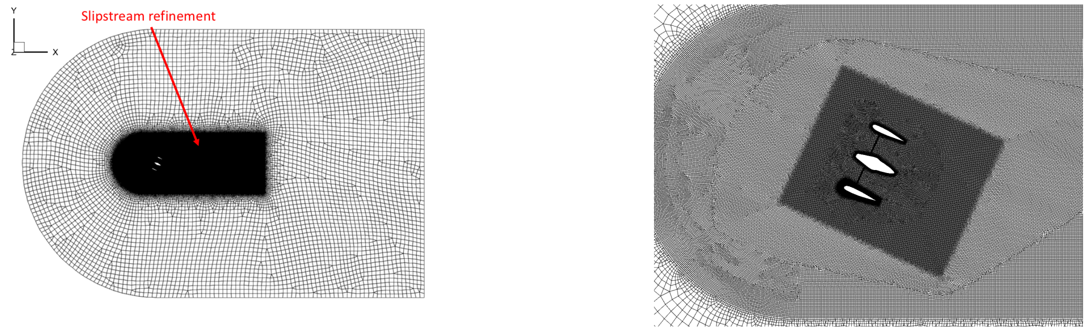

(a) 2D mesh of entire numerical domain **(b)** 2D mesh in slipstream refinement

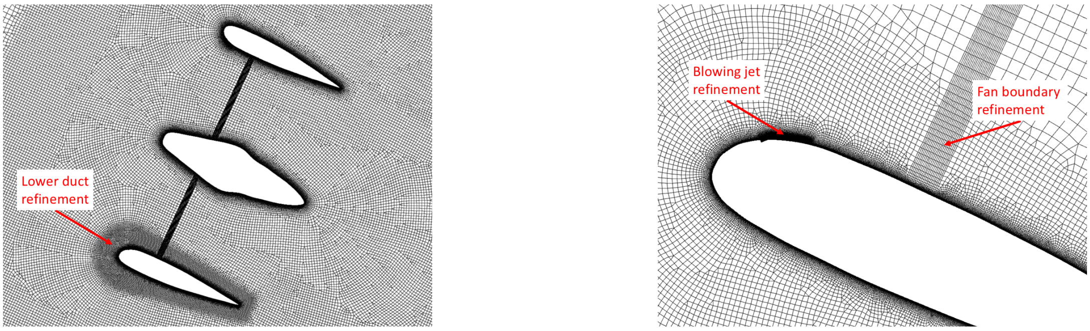

(c) 2D mesh in the propeller refinement **(d)** 2D mesh refinements on the jets

Figure 3.10: Mesh of the ducted propeller in the 2D simulation. The duct surfaces have a spacial discretisation based upon the NACA 0018 analysis

The geometry of the ducted propeller and the fan boundary are tilted when a different angle of attack is of interest. In the figures above the angle of attack is 25°. The slot height was 5 mm at 5% of the duct length with a local inclination to the surface of 20°. As the passive system was not implemented in 2D, no design was proposed for it. Further discussion on the active flow control system can be found in subsection 3.5.5.

3.5.2. Low fidelity comparison between 2D and 3D

In the 2D simulation the effective geometry simulated is not a circular duct. In practice the setup numerically represents a biplane setup. Since this is a significant difference in the geometry, the difference should be understood better. Free and well-established numerical software can accurately use low fidelity models to analyse these kinds of geometries. XFLR5 is a multi-analysis solver which can perform both Vortex Lattice Method (VLM) as well as panel method analyses. Both simply a lifting surface as will be described later. Neither analysis is, however, able to model viscous flow effects. It can only solve for viscous drag by interpolating from 2D polars, according to the theoretical information published by Deperrois [50]. This means there is no significance to take from the the results. It would be beneficial to understand the offset between the 3D ducted propeller case and the 2D biplane case.

As stated, XFLR5 can perform two analyses, a Vortex Lattice Method (VLM) and a panel method. The VLM option assumes airfoils to infinitely thin and calculating the horseshoe vortex wake. It uses the influence of the horseshoe vortices to determine the local load. As the surfaces are considered thin, this method only returns the local load in difference in pressure between the upper and lower part of the surface. Panel methods use panels on the surface of the body to determine local surface pressures. The more difficult limitation in XFLR5 for the panel method is that it cannot analyse a biplane. Where the VLM analysis is supported when a biplane is created, the panel method becomes unavailable for simulations. It requires the creation of a biplane out of a single geometry. This requires vertical sections on the geometry to connect the two. In the used analysis the two wings are separated by the diameter of the ducted propeller. The ends of the biplane were set at a 10 m distance from the centre. Another simulation was done with 20 m, but there was not much influence. The ducted propeller was modelled with a ring wing. The chord length for both cases was set at the duct chord length. The biplane and ring wing are displayed in Figure 3.11a and Figure 3.11b respectively.

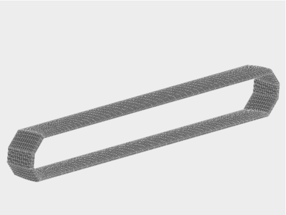

(a) Biplane model used for VLM

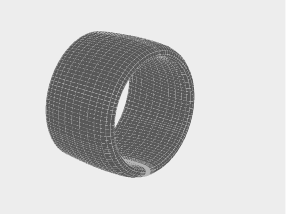

(b) Ring wing used for VLM

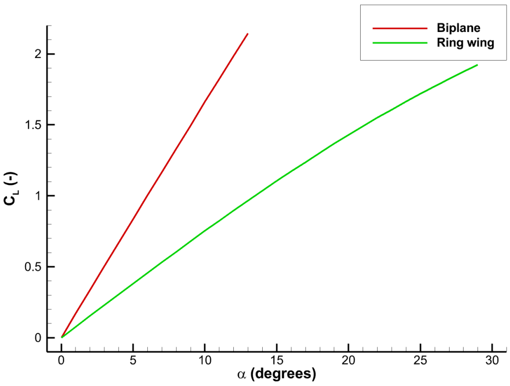

(c) Lift polars for biplane and ring wing from XFLR5 with a VLM analysis. The prescribed velocity is 25 m/s, resulting in Re 2.10 million. It can be seen that the biplane has a higher lift-curve slope.

Figure 3.11: XFLR5 VLM analyses to discuss difference between a ring wing and biplane. The airfoil used is the airfoil of the duct of the X22. The chord length is 1.24 m and the ring diameter and height between the two wings is 2.134 m.

From Figure 3.11c the lift curve slopes for the biplane and ring wing were calculated. For the biplane, the slope was found to be 0.165, while for the ring wing 0.0671 was found. This creates an offset factor of 2.46. The difficulty is that this is the overall lift coefficient of the system, not the local lift coefficient at the 2D midplane. When comparing the pressure distributions on the VLM and panel simulations, it was found that similar distributions are found at an offset of 1.9. This means that at an angle of attack of 10° at the biplane, a similar distribution was found at 19° at the ring wing. The simulations do not include the separation point, since not all simulations converge for this point. However, the offset does indicate that the 2D case would exhibit stall twice as early as the 3D duct in terms of angle of attack. This is important to discuss when comparing 2D simulations with 3D reference data.

3.5.3. 3D numerical domain

In general the 3D setup is based on the 2D setup. A blowing jet implemented at the top duct in 2D was not implemented in 3D, as it proved to have no effect on the separation prevention. The numerical domain is of similar size, but has been revolved around the x-axis. The numerical domain is only a half domain. The reasoning is the absence of swirl in the flow. As this swirl induced by the propeller is not of interest to the upstream lip separation, it is not introduced by the fan boundary. As this is not of part of the flow, the condition is symmetric and the half domain can be equipped with a symmetry boundary condition. The green surface in Figure 3.12a indicates the symmetry boundary on which this condition is applied. This reduced the need for a large mesh of the entire duct. In Figure 3.12b the main zones of interest are displayed. In green the symmetry boundary is displayed. The fan boundary is displayed in blue and the surfaces of the spinner and duct are grey. The red surface is the lower lip surface. It is expected that this surface displays the separation of interest and therefore requires a finer mesh than the other surfaces. The lower lip and the other surfaces are no-slip walls. In Figure 3.12c the far field boundary conditions can be found. In light green the velocity inlet boundary is displayed, while a pressure outlet is used at the end of the numerical domain. Velocities on the velocity inlet are defined as the upstream velocity directed in the direction of the x-axis. The outlet condition is the upstream static pressure.

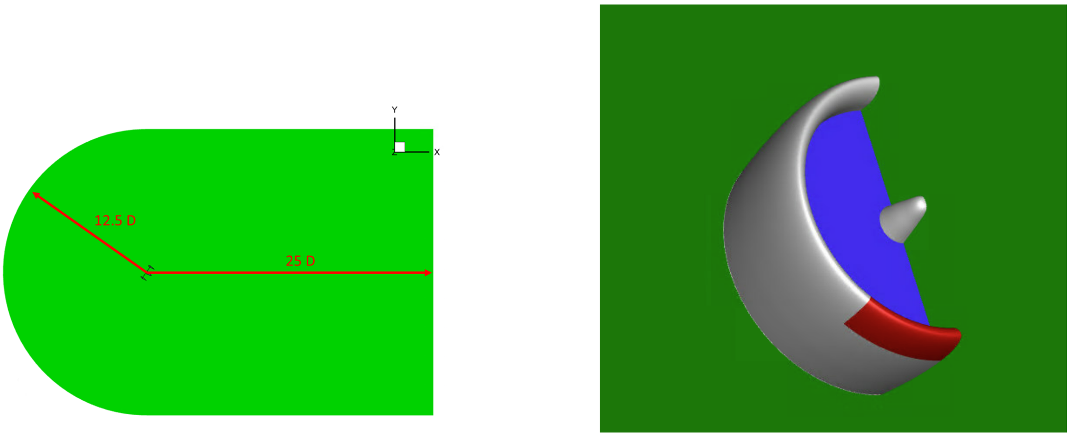

(a) 3D Numerical domain with the size relative to the propeller diameter D. Green indicates the symmetry boundary and blue the fan boundary.

(b) Numerical boundaries of relevance. Green : symmetry boundary, blue :fan boundary, grey : no-slip wall for the duct and centerbody, red : no-slip wall for lower lip

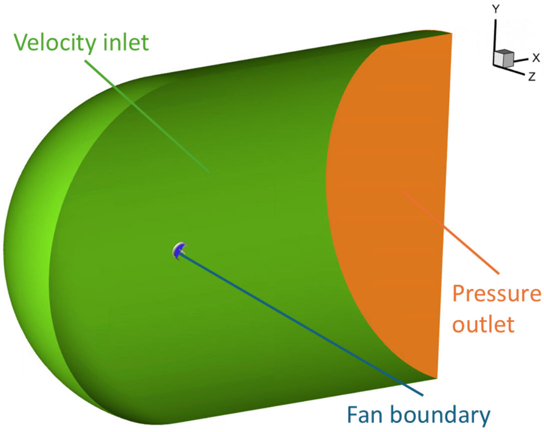

(c) Far field boundary conditions in the 3D numerical domain

Figure 3.12: 3D setup utilised in this thesis

3.5.4. 3D setup

In 3D the mesh setup had to be slightly changed as compared to the 2D mesh. The number of cells in 2D was over 300,000, which would result in $(300,000)^{3/2} = 164$ million cells. This would be impractical for simulations and is inefficient from a computational effort perspective. The regions of interest would thus be refined, while less important zones would be coarsened. As discussed, the local refinements were adapted in such a way as to create an efficient mesh. The refinement zones used in the 2D setup were used as a basis. However, in 2D each refinement zone was a separate region. For 3D only three regions were used. The bulk of the numerical domain was a single zone, while the regions right before and after the propeller were also separate zones. This setup is required as the fan boundary condition in Fluent has to be applied to an internal boundary. The internal boundary within the duct was set to this fan boundary condition. As discussed before, the assumption was made to apply a pressure jump across the entire fan boundary condition, thus neglecting the tip gap.

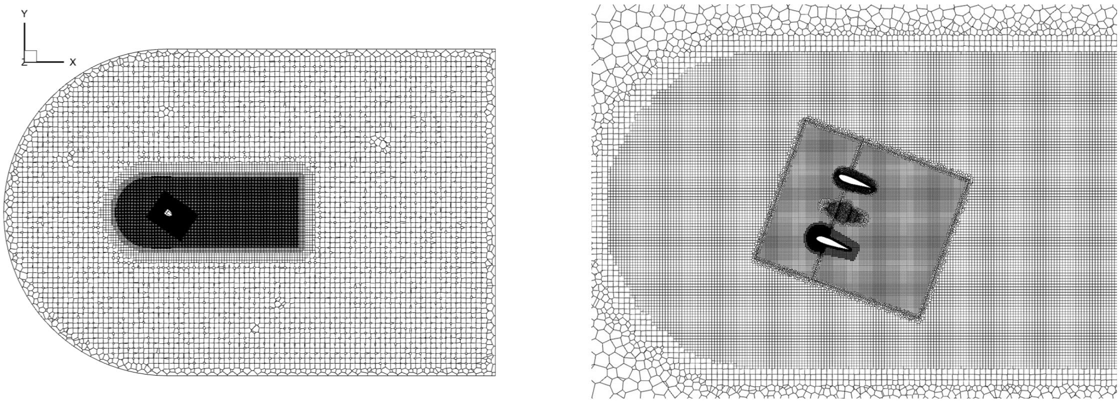

(a) 3D mesh in the entire numerical domain

(b) 3D mesh in the slipstream refinement

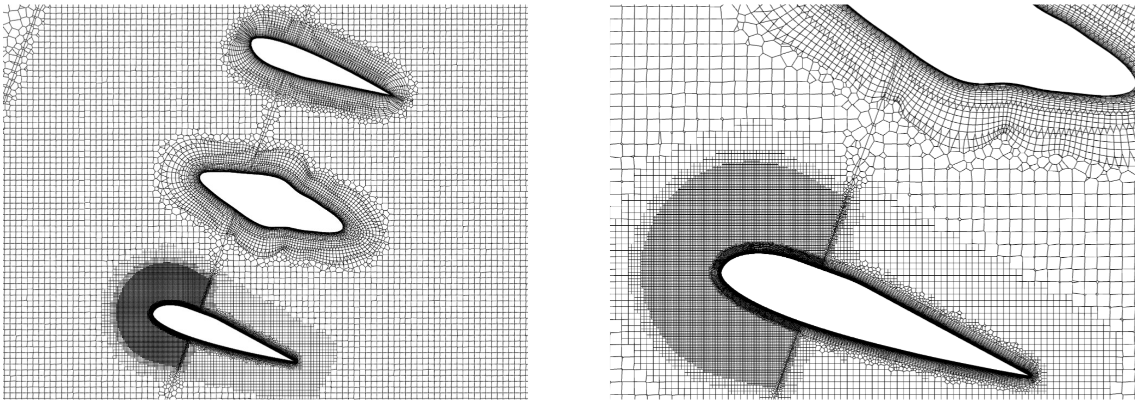

(c) 3D mesh in the propeller refinement

(d) 3D mesh close to the lower lip

Figure 3.13: 3D mesh used in this thesis. The ducted propeller is positioned at an angle of attack of 35°. The mesh is a 2D illustration of the 3D mesh on a slice slightly inward of the z-plane. Each figure slightly close to the symmetry plane. Note the coarser mesh compared to Figure 3.10a - Figure 3.10d

As can be seen a poly hexcore mesh is used. As the flow will have a general direction in line with the x-axis, the poly hexcore allows cells to be aligned with this direction. This would allow for an efficient mesh. The lower 45° of the duct is refined. It is the section of the duct where separation is expected. Note that this 45° is on the half model, in practice this would refine the lower quarter of the duct. In Table 3.1 the number of cells for four variants of the mesh are noted.

Table 3.1: Cell mesh count in 3D

	Cell count (million)
Coarse	4.8
Mid	6
Fine	9.4
Superfine	12.1

As will be discussed in section 4.1, the $k-\omega$ SST model was chosen for the turbulence model. Nambiar et al. [8] use the same turbulence model in their work, which discusses similar types of separation and flow control. It proves to be effective and accurate for this condition. Initialisation is done from the inlet condition. This yields an initial condition of undisturbed flow. The solver was set with a SIMPLE pressure-velocity coupling and second order upwind discretisation. Since part of the motion in the flow is unsteady, URANS was used to solve the 3D simulations. For each time step the convergence criteria for x,y,z-velocity, k, ω and continuity is $1e-5$, which should converge the simulation. The convergence criterion was also found in the work of Nambiar et al. [8]. For the coarse and mid meshes the time step was set to 0.005 seconds, while for fine and superfine a time step of 0.0025 seconds was used. This would yield a Courant number in the bulk flow of well below 1.

3.5.5. Tangential blowing setup

The active tangential blowing in 3D was applied with a velocity boundary condition. The prescribed momentum can thus be added to the flow, with a prescribed velocity. It is also the boundary condition used for the tangential blowing in 2D. The validation process proved that this setup is accurate with respect to the reference case. For 3D the momentum coefficient definition is used as in the reference paper [13]. The width of the slot may need to be implemented, but non-dimensionalising with the surface of the duct returned low C_μ values. This is because in 2D the entire surface is effected by the blowing jet. In 3D the top half of the duct is uneffected by the blowing jet. For a more even comparison, the area in the equation should be the effected wetted surface. Using the effected wetted surface yields the same equation for 3D as for 2D.

In literature the design of a blowing slot has been widely investigated [8], [9], [13]. As this thesis is not focused on improving this design, known conventions from literature are taken. An important part of the tangential blowing system is the position on the surface. To prevent separation, the momentum should be added before the separation point, however the work by Benjamin et al. [9] also displayed that positioning the slot far forward may cause separation. For the 2D case the separation occurs later than for the 3D case, so for 2D the slot is positioned at 5% of the duct length, while for 3D the position is 3%. Another parameter is the slot height. In section 3.4 the case presented by Puri et al. [13] was equipped with slots of 3.1 mm, which is 0.31% with respect to the chord length. Small slots have proven to be very effective in literature, but a small jet will restrict the flow rate through the channel of the passive system. This balance is difficult to place, but it was found that a slot of 7 mm was ineffective in 3D. For 2D and 3D simulations the slot height was set at 5 mm which roughly translates to 0.4% of the duct length.

The inclination of the slot with respect to the local surface has been discussed at length in literature. To achieve a blown boundary layer instead of the air jet vortex generator effect, a shallow inclination is required. Puri et al. [13] used an angle of 20° with respect to the local surface. To enhance the Coandă effect of the jet from the slot, the surface from the slot was smoothed to the duct surface with a fillet. In 2D, slots were positioned on both the upper and lower duct lip, but it was decided that the upper lip slot did not improve the boundary layer behaviour on the lower lip. For 3D the width of the slot must also be determined. Benjamin et al. [9] proved that this type of active flow control only works if the slot is wider than the separated region. With the results from CFD, it was found that a slot width of 90° could perform effectively, which is in fact simulated by an angle of 45° as only half a model is simulated. The edge of the slot was fitted with a small chamfer to avoid numerical instabilities and dense mesh.

3.5.6. Passive tangential blowing setup

For the 3D channel equation, the 2D equation from Equation 3.5 is taken. To add the third dimension to this equation, all heights h and h_j and lengths L are multiplied by the width of this section of the channel cc. Note that this ignores the friction on the sides of the channel, but this is a small part of the channel. The majority of the friction is found on the walls which are included. Applying this yields:

$$p_{t,1} - p_j = (\frac{LccC_f}{A} + \frac{1}{2}(\frac{A}{A_j})^2)\rho v^2 \tag{3.11}$$

Where A and A_j are the areas of the bleed port and jet slot respectively. cc is the width of the channel, which in this approach is equal to the width of the bleed port. This width can be found when the area A is divided by the assigned port height h. Any observations done for the 2D equation hold for the 3D equations similarly. This means that the area of the bleed port should be 5 times the area of the jet slot.

It was noticed during simulations that where the active tangential blowing can be simulated with a velocity inlet boundary condition, this passive system requires a different setup. Using a velocity inlet would allow for a prescribed velocity, which in turn would change the pressure on the jet slot, which in turn changes the velocity prescribed. It was observed during simulations that this approach was highly unstable. To solve this problem, it was decided to use a pressure inlet boundary condition on the jet slot. To prescribe these inlet flow conditions the channel equation had to be rewritten:

$$p_{t,1} = \frac{LccC_f}{A}\rho v^2 + \frac{1}{2}(\frac{A}{A_j})^2(\frac{A_j}{A})^2\rho v^2 + p_j = \frac{LccC_f}{A}\rho v^2 + \frac{1}{2}\rho v^2 + p_j = \frac{LccC_f}{A}\rho v^2 + p_{tot,j}$$

$$p_{t,1} - \frac{LccC_f}{A}\rho v^2 = p_{tot,j} \tag{3.12}$$

With $p_{t,1}$ being the pressure on the bleed port. Channel velocity v can be found with the equation described previously. As the bleed port design can highly influence the operation of this system, it was decided to simplify the bleed flow. Instead of actually bleeding off the flow behind the propeller, the ports are positioned and the pressure over these surfaces are evaluated. The pressure is used in the channel flow equation to find the momentum addition possible. This will negate the effect of bleed on the trailing edge of the duct. It is considered a limitation, but this thesis focuses on lip separation prevention. It must be noted that this implies that the effect of bleeding airflow from the flowfield is not simulated. As some literature uses bleeding as a type of flow control, it can be argued that this effect may play a role in the effectiveness of the system, even in a beneficial way. Since this is a different type of flow control, it is considered outside the scope of this research.

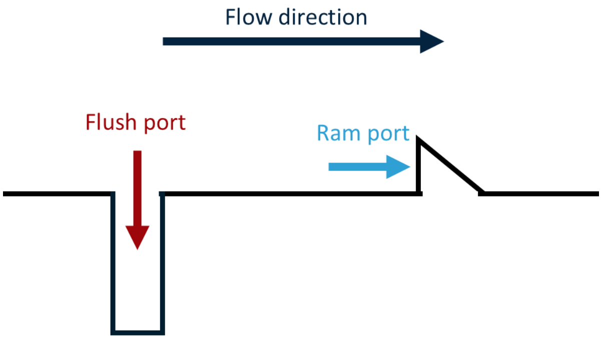

Figure 3.14: Illustration of the flush and ram ports by the author. The flow direction is perpendicular to the ram port, thus resulting that the ram port captures total pressure, the flush port only captures static pressure.

A final influence is the type of the bleed port. Two types will be considered in this investigation, the flush and the ram port as indicted in Figure 3.14. A flush port bleeds static pressure from the local flow field, just as a static port on an aircraft fuselage can measure static pressure. A ram port is protruding out of the surface and uses ram air. The ram air applies the local total pressure to the channel flow. A ram port can thus achieve a higher differential pressure with the jet pressure, but does require a protruding design, possibly causing flow separation. During the 3D phase this thesis discusses and simulates these types of ports.

4

Validation

Before retrieving results from the simulations, it is important to note the validity of the simulations. This chapter discusses the validation of the chosen setups. In section 4.1 the tangential blowing setup is validated. A limited validation step is applied to the 2D simulation, which can be found in section 4.2. Finally, the validation process for the 3D simulations is discussed. This is presented in section 4.3.

4.1. Tangential blowing airfoil validation

The mesh and numerical domain as described in section 3.4 are for an one meter airfoil, which is similar to the 1.24 meter chord length of the X22 duct. It is positioned at an angle of attack of 15°. The freestream velocity of 4 m/s is prescribed to achieve a Reynolds number of 250000, which is a condition also discussed by Puri et al. [13]. The pressure distributions are used for validation of the setup created here. In Figure 4.1a the pressure distribution for various meshes are plotted. Note that in this figure the airfoil is equipped with blowing slots, but the jets are off. This is done to inspect the ability of the meshes in predicting the separation point. A blown case would not be useful, as no or reduced separation is expected. It can be seen that the distribution is dependent on the mesh until the mid-mesh size. Finer cells do not enhance the accuracy any further. Therefore the mid sized mesh is deemed accurate enough. The dependency on the turbulence model is also investigated. Puri et al. used the $k-\epsilon$ model. From Figure 4.1b it can be seen that the dependency on the turbulence model is low. The figure displays the pressure distribution for the blown NACA 0018. A momentum addition C_μ of 5% was applied, which enables attachment in a case that otherwise displays significant separation. From the graph it can be deduced that the difference between the $k-\epsilon$ and $k-\omega$ SST models is small, while the use of Spallart-Allmaras (SA) returns slightly different results. For the next analyses, the mid mesh is used as a basis and $k-\omega$ SST model is used as a turbulence model.

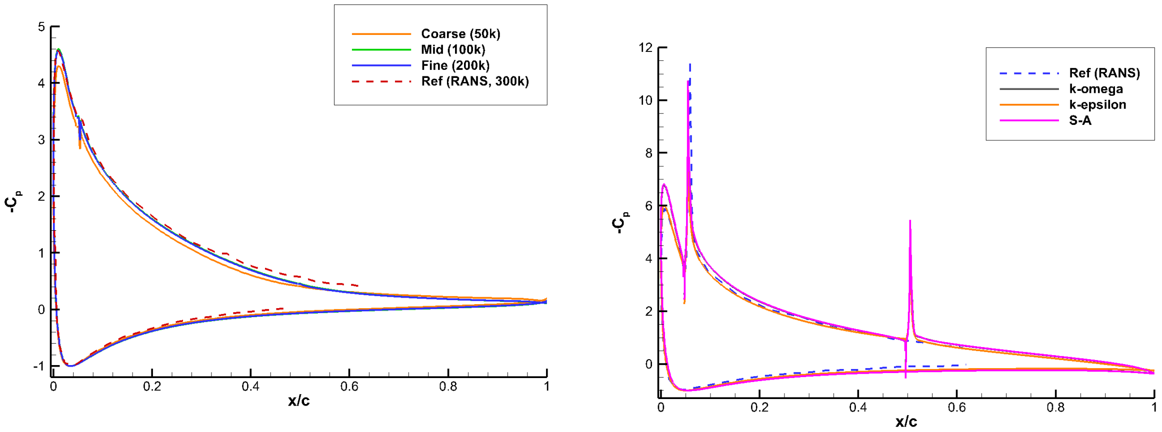

(a) Pressure distributions for unblown NACA 0018 airfoil to evaluate the separation prediction of each mesh. The modelling of separation was accurately done by the mid and fine mesh, compared to reference data from Puri et al. [13].

(b) Turbulence dependency for blown NACA 0018 airfoil. The SA model seems to be less accurate with respect to reference data from Puri et al. [13].

Figure 4.1: Setup dependency study for the NACA simulation. It was found that the mid mesh and the $k-\epsilon$ and $k-\omega$ SST models were deemed accurate with respect to the reference data [13]. For the next analyses, the mid mesh is used as a basis and $k-\omega$ SST model is used as a turbulence model.

4.2. 2D validation

As already discussed, Bento et al. investigated the difference between square and round ducts on the performance of a ducted propeller [17]. The simulation data of the round duct from this paper was used as validation data for the 2D setup. For this setup the mesh was scaled down as the ducted propeller used by Bento had a chord length of 0.3 meter. Bento used a round ducted propeller in a stationary zone with a single blade of the XPROP in a rotating zone. XPROP is a scientific model used by the TU Delft as a reference propeller [51]. As the flow is axial, Bento only simulated a quarter of the entire ducted propeller, with periodic symmetry boundaries closing the numerical setup. Note that a comparison with this setup will have an offset, as discussed in subsection 3.5.2. In Figure 4.2a the pressure distributions for both the setup of this paper and the setup of Bento are displayed.

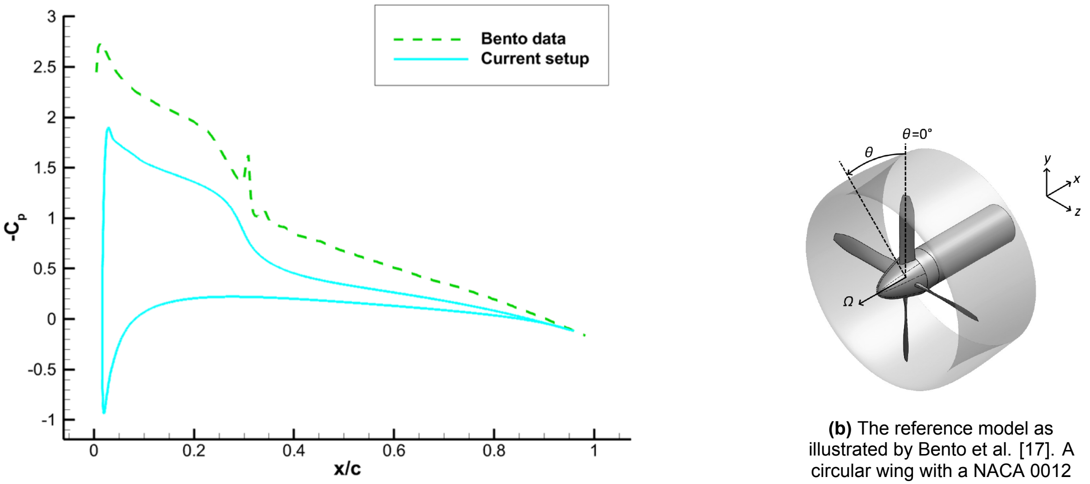

(a) Pressure distribution on the inside of the duct for Bento setup at J = 0.7 in axial conditions [17]. The difference can be explained by the different between the 2D simulation of this thesis and the 3D simulation performed by Bento et al.

(b) The reference model as illustrated by Bento et al. [17]. A circular wing with a NACA 0012 airfoil cross-section around a 4 bladed XPROP model. One quarter of the model is simulated with a sliding mesh simulation.

Figure 4.2: The results and setup as used by Bento et al. for a ducted propeller

The plotted Bento data is only the pressure distribution over the inside of the duct. The pressure distribution of the current setup is over the entire duct. The offset between the 2D and 3D simulations can be seen here, which was discussed in subsection 3.5.2. It is argued that the offset is related to the difference in 2D and 3D simulations. In general, the chosen setup has a similar behaviour as the higher fidelity Bento setup. In this 2D phase of the research, determining the momentum coefficient and discussing the possible operation of the passive system are of interest. For this purpose the setup provides a basis. As stated previously, no conclusions will be taken from he 2D analyses.

4.3. 3D validation

4.3.1. Unsteady resolved flow

Separation on the outside of the duct and on the lower trailing edge of the duct behaves unsteady. This can be found when discussing the residual in the steady RANS simulations, presented in Figure 4.3. Steady RANS cannot simulate this behaviour and the solution will not reach the set convergence criteria. It is deemed an unsteady behaviour as the same mesh does converge for axial conditions.

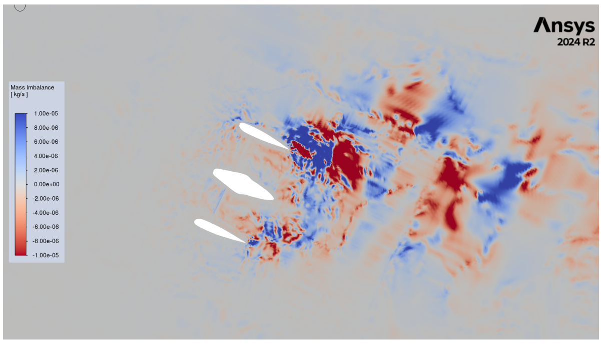

Figure 4.3: The mass conservation residual for the 2D steady RANS ducted propeller with C_μ = 5%. This is the residual for Figure 5.2d. The residual is most notable in the wake of the upper duct, indicating a possible unsteady flow.

The solution is to employ a URANS simulation in 3D. The RANS results of the lower lip of the duct display an independency on the number of iterations. The separation on the inlet, which is of interest for this thesis, is thus likely steady or quasi steady. The definition of the lower lip is defined in red in Figure 3.12b. To investigate the steadiness on the lower lip, the minimum pressure and the overall resulting force on the lower lip of the duct are reported for a period of time. The minimum pressure $C_{p,min}$ indicates whether locally a maximum is steady, while the force magnitude report can indicate the steadiness over the entire lip. Note that this is the resulting force magnitude. In Figure 4.4 the behaviour of these two properties are displayed over a period of time. As separation is of interest, the ducted propeller is positioned at 40° angle of attack. With a free stream advance ratio of 0.522, this case approximates a case in reference data [25]. It was observed in literature and in these simulations that these conditions can cause separation on the lower lip.

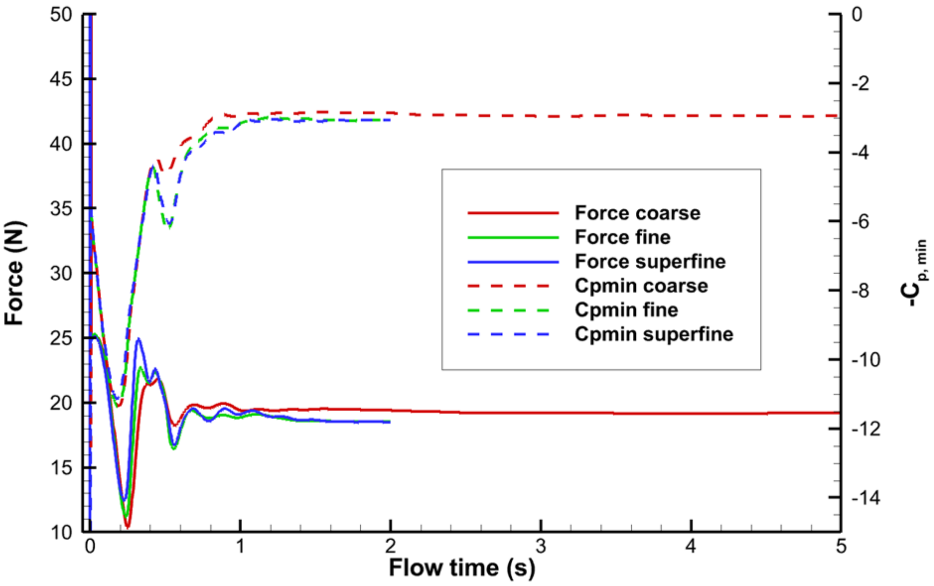

Figure 4.4: $C_{p,min}$ and force on the lower lip over a period of time. The lower lip surface is defined in Figure 3.12b. The ducted propeller operates in a separated condition with v_∞ = 13 m/s, J_∞ = 0.522, α = 40°, $\theta_{0.75}$ = 19°. For this condition the resulting separation is displayed in Figure 5.5.

The coarse mesh was run for 5 s of flow time, while the finer meshes are run for 2 s. It can be noted that after 1.5 s the behaviour seems to stabilise. It is thus chosen to run the coming simulations for 2 s for completely resolved flow at the lower lip.

4.3.2. Pressure validation

In de design process of the Bell X22, the ducted propeller was investigated thoroughly in the wind tunnel [19], [25]. Part of this investigation was the pressure distribution on the ducted propeller itself. In the wind tunnel the pressure measurements were conducted at an offset from the centre plane. The offset angle is 13°, so the results displayed are also taken from the bottom duct surface with an offset angle of 13° with respect to the symmetry plane. This is illustrated in Figure 4.5.

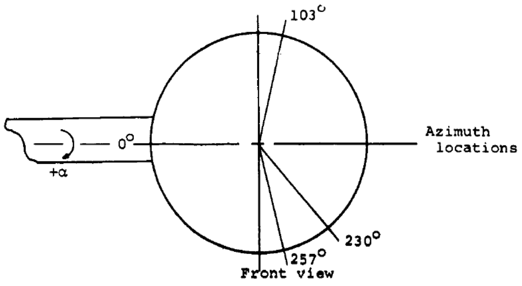

Figure 4.5: The locations of the measurements taken by Kriebel et al. [25].

To validate the 3D setup, the conditions of the wind tunnel were recreated. It must be noted that the exact upstream velocity is not mentioned, but the Reynolds numbers investigated during the test were interpolated and a resulting free stream velocity of 13 m/s was found [25]. In Figure 4.6a and Figure 4.6b the pressure distributions for 20° and 40° angle of attack are presented respectively.

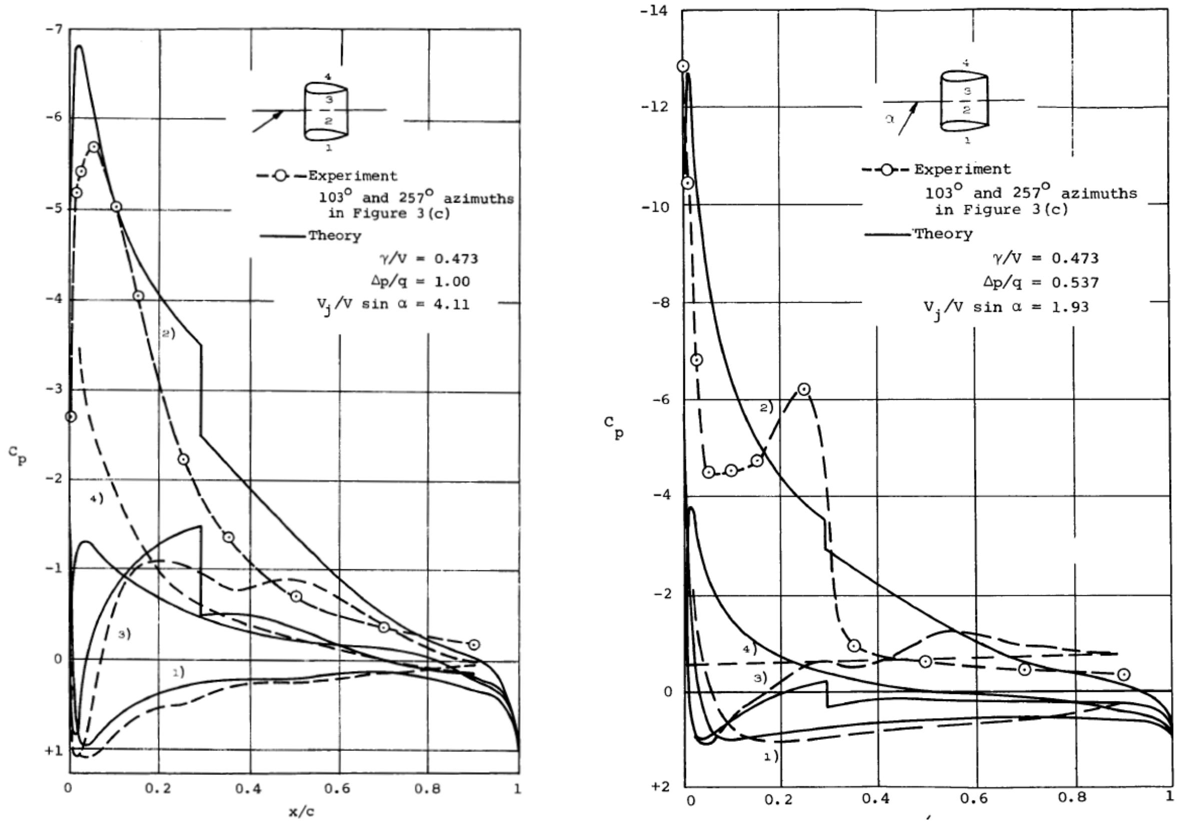

(a) Pressure distribution for α = 20°

(b) Pressure distribution for α = 40°

Figure 4.6: Pressure distribution found by Kriebel et al. [25]. The distribution is taken on the X22 ducted propeller with v_∞ = 13 m/s, J_∞ = 0.522, $\theta_{0.75}$ = 19°

The angle of attack and thrust coefficients were mentioned in the reference. The thrust coefficient was different than what would result with the same advance ratio and propeller pitch setting in axial flow. Due to the angle of attack of the duct, the velocity perceived by the propeller is lower. This yields a lower effective advance ratio, so a higher thrust was generated according to Figure 3.2a. To match the thrust from DFDC to the actual thrust, the propeller rotational speed was altered slightly. This would yield a more similar pressure jump to the actual case. In Figure 4.7a the pressure distribution per mesh is displayed. It was decided to not simulate a tip gap as this introduced the fan-induced separation, so the fine mesh was used to validate with a closed tip gap. This comparison can be seen in Figure 4.7b. Note that the reference data in Figure 4.7b is the same data as can be seen in Figure 4.6a.

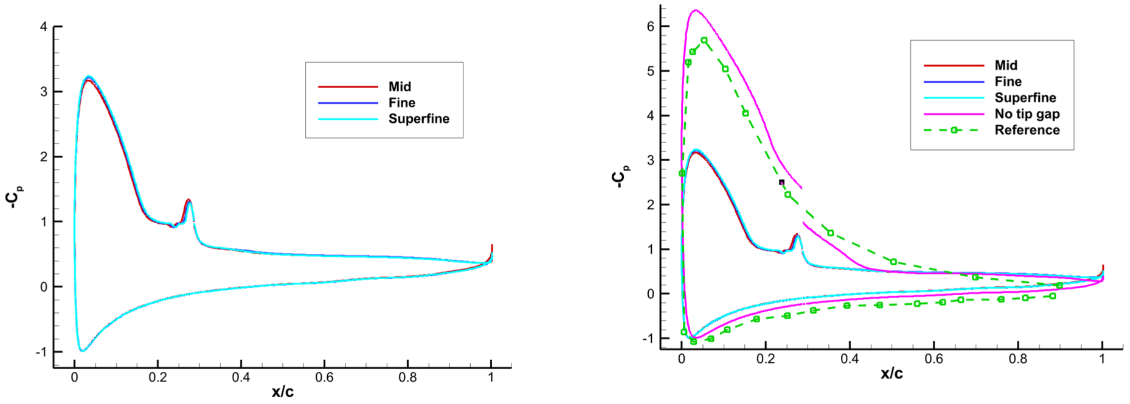

(a) Pressure distribution for three mesh densities. The fine and superfine meshes are nearly identical, while the mid mesh shows a lower pressure distribution.

(b) Pressure distribution with closed tip gap. Note that the simulation with a closed tip gap has a higher pressure distribution compared to the reference data. A cause can be that that the boundary layer is effeted by the closed tip gap.

Figure 4.7: Pressure distribution on the lower lip at 13° off the symmetry plane for v_∞ = 13 m/s, J_∞ = 0.522, α = 20°, $\theta_{0.75}$ = 19°

As can be seen in Figure 4.7a the fine mesh captures the pressure distribution more effectively than the mid mesh, but just as effectively as the superfine mesh. It was therefore chosen as the mesh for this project. In Figure 4.7b the pressure distribution for the fine mesh with a closed tip gap and the reference data can be seen. It must be noted that there is an inherent difference in pressure distribution due to the usage of a fan and the closed tip gap. These are limitations of the setup, however the closed tip gap simulation does approximate the reference data more accurately than the open tip gap simulations. For the purposes of this thesis, it is deemed accurate.

4.3.3. Upstream boundary condition

Upon closer inspection the far field boundary conditions also proved to have an effect on the solution. The numerical domain was bounded by the symmetry plane, a large velocity inlet and a pressure outlet. The upstream and sides of the numerical domain are defined as a velocity inlet in direction of the x-axis, as was displayed in Figure 3.12c.

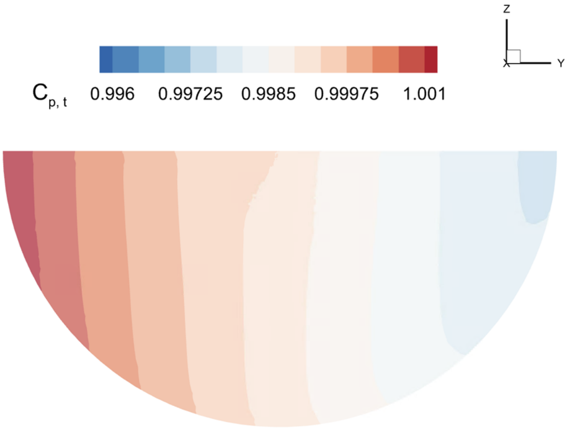

Figure 4.8: Total pressure distribution upstream of the baseline ducted propeller

It was discovered that this inlet boundary condition can apply an unintentional static pressure to the flow field. To check the effects of this boundary condition, the total static pressure coefficient is plotted on a slice 2 m upstream of the ducted propeller. In Figure 4.8 the distribution can be found. It must be noted that there is a noticeable distribution in total pressure. This means that the velocity boundary condition does not provide a uniform pressure field to the numerical domain. One must also note the plotted range of $C_{p,t}$, 0.996 to 1.001. The maximum non-uniformity is 0.4% off the ideal total pressure. The implication is that the non-uniformity of the flow field, although present, is not considered as significant and may only influence the results very slightly.

5

Results

In this chapter the results from the CFD simulations will be discussed. As the simulations were performed in a 2D and 3D phase, the results will also be discussed separately. Certain flow phenomena are found to be relevant from 2D simulations, upon which the 3D simulation will expand. Parameters, such as the freestream velocity, the advance ratio and the momentum coefficient, will be chosen in 2D. All 2D analyses are presented in section 5.1. The results from the 3D analyses are presented in section 5.2.

5.1. 2D analysis

The 2D simulations were used to provide an insight into the effectiveness of the passive momentum concept. Certain parameters, such as operating conditions, can be investigated more efficiently with 2D simulations.

5.1.1. Active tangential blowing effectiveness

Before discussing the entire PTB concept it is worth investigating the momentum addition budget required. From the NACA 0018 investigation the coefficient definition for the momentum addition is taken. In Equation 3.10 the jet height h_j is varied, while the chord length c is the duct chord length.

In the wind tunnel seen in Figure 2.5a [25], the ducted propeller was tested in various conditions. One of these conditions is at v_∞ = 13 m/s and J_∞ = 0.522 and at an angle of attack of 40°, for which the pressure distribution can be found in Figure 4.6b. This condition will be further discussed in section 5.2, but to keep the 2D simulation comparable with 3D condition, the same loading is applied. This means the same pressure jump is applied, so the local effective advance ratio due to the angle of attack is not changed. The predicted pressure jump from DFDC is applied, which is the pressure jump in Figure 3.4.

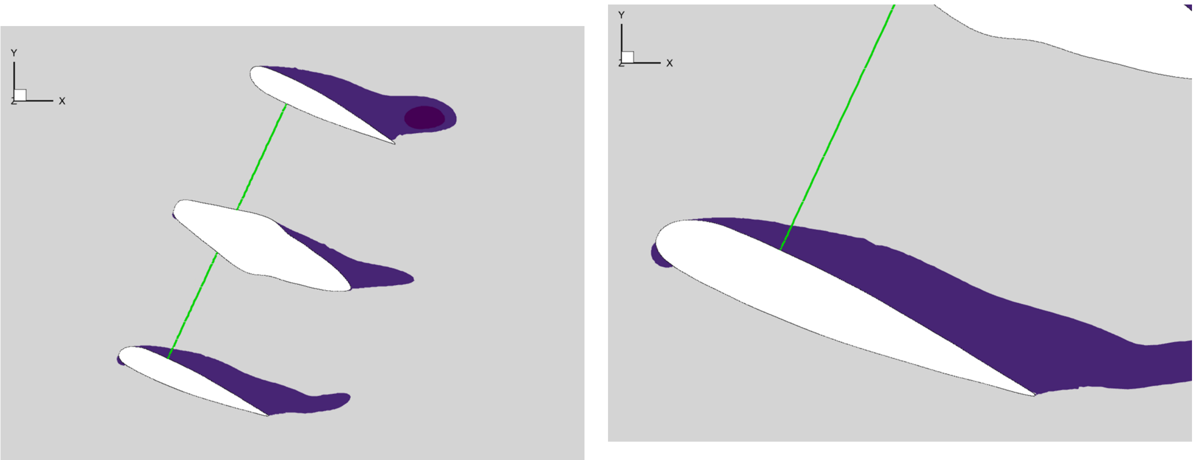

(a) Separation on the ducted propeller. Separation on the centerbody and the top duct are not of interest in this thesis.

(b) Separation on the lower duct. The blue region on the outside of the lip is not separation, but the flow reverses locally from the stagnation point on the lower surface of the duct.

Figure 5.1: Separation on the baseline ducted propeller with V_∞ = 13 m/s, J_∞ = 0.522, α = 25°. These 2D simulations present separation at lower angles of attack as compared to the wind tunnel experiment [25]. It is expected that this is the effect of it being a 2D simulation.

The blue coloured region highlights the locations where the velocity is in negative x direction. It indicates the separated region, as within this region the flow has a reversed direction. The flow reversal is also indicated in the last profile in Figure 2.6. Note that this does not apply to the region at the leading edge, this is flow from the stagnation point to the duct lip.

As can be seen the separation starts near the leading edge. It is the type of separation of interest. To counteract this separation, the tangential blowing port is applied here. In Figure 5.2a the blowing slot is positioned at 5% of the duct chord, has a height of 5 mm and has a local inclination of 20° to the surface. A C_μ of 4% is applied. In Figure 5.2b displays the same setup, but with a C_μ of 5%.

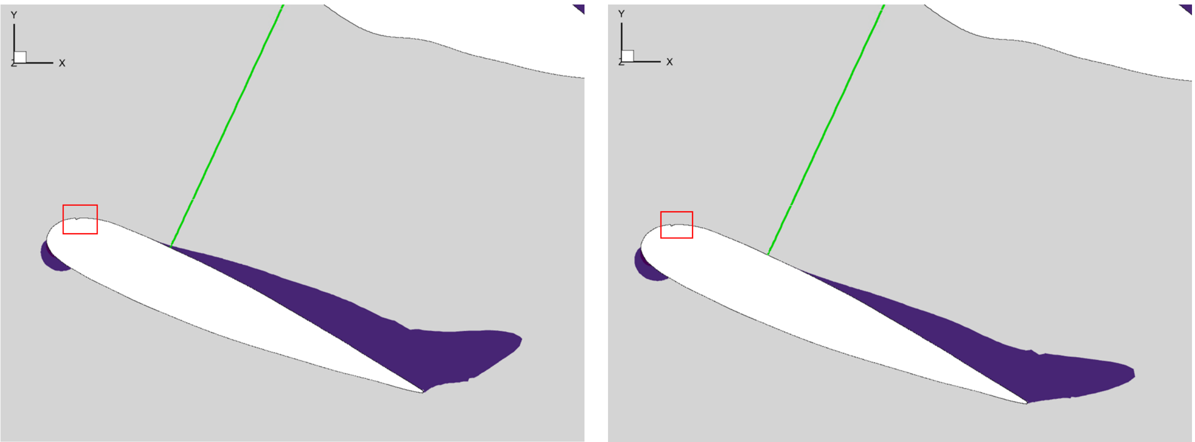

(a) Separation on the lower duct with C_μ = 4%. The red box is zoomed in Figure 5.2c.

(b) Separation on the lower duct with C_μ = 5%. The red box is zoomed in Figure 5.2d.

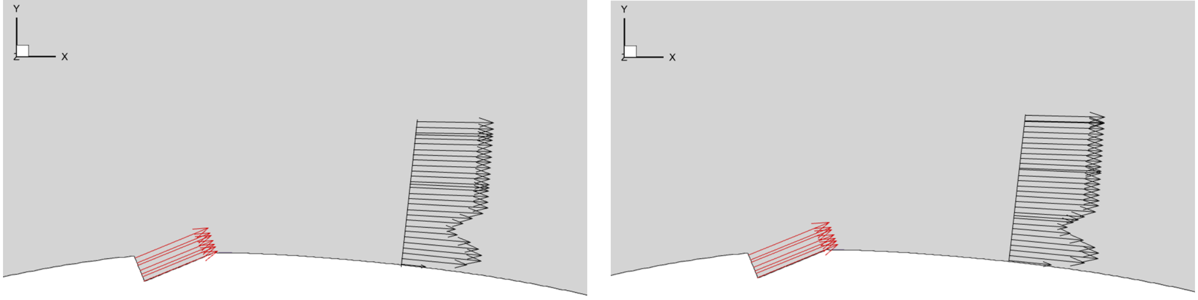

(c) The tangential blowing vectors and the resulting blown boundary layer, C_μ = 4%

(d) The tangential blowing vectors and the resulting blown boundary layer, C_μ = 5%

Figure 5.2: Separation on the blown ducted propeller with v_∞ = 13 m/s, J_∞ = 0.522, α = 25°, $\theta_{0.75}$ = 19°. The resulting blown boundary layers display the momentum addition as discussed in chapter 2. C_μ = 5% displays slightly more momentum in the lower region of the boundary layer than C_μ = 4%.

As can be seen, the momentum addition of 5% is more effective than 4%. The separation is postponed more effectively, but both can reduce the separation, effecting the propeller. The 5% case allows the flow to stay attached slightly longer after the fan. It can thus be concluded that this momentum addition is effective in postponing separation. It can also be seen why Puri et al. [13] used two blowing slots, as separation still occurs at the half chord. The goal of this system is to reduce uneven loading on a propeller induced by separation. The 4% momentum addition is enough to achieve this goal, but 5% is more effective.

5.1.2. Passive line analysis

The 2D analysis was used to discuss if enough pressure differential is available for a possible passive system. To discuss the possibility of a working PTB system, the pressure differential on the channel must be investigated. Two options are possible, a flush port or a ram port. In practice a flush port is more preferable as it disturbs the flow less. From the CFD results, the local pressure coefficients are taken. The flush port would take static pressure and the corresponding coefficient is C_p, while for the ram port the total pressure along the height of the port would be of interest with the $C_{p,t}$. The measurements for the flush port are taken from a surface of 25 mm in length positioned shortly behind the propeller. The ram port is defined as a line starting from the front of the flush port and 25 mm in upward direction to the surface. The ports are presented in Figure 5.3, with the fan boundary indicated in green.

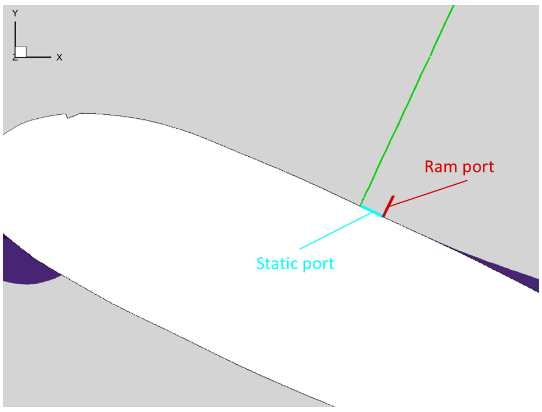

Figure 5.3: Bleed ports in the 2D simulation. Red indicates the flush port, while cyan indicates the ram port.

From CFD, the surface averages are taken for the flush and ram port as indicated in Figure 5.3. The results in Table 5.1 are obtained. The possible momentum addition versus a pressure differential is plotted in Figure 5.4. These are calculated with the channel equation as presented in Equation 3.6.

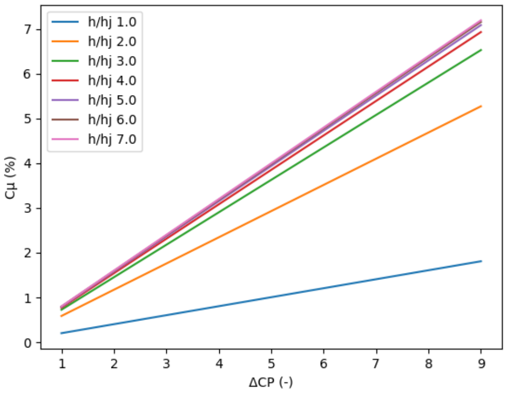

Figure 5.4: Momentum addition possible with pressure differential on the channel

Table 5.1: Pressure differential coefficients for 2D blown case

			ΔC_p	C_μ
cm 4	$C_{p,jet}$	-4.186		
	C_p	-0.494	-3.692	2.930
	$C_{p,t}$	-0.474	-3.711	2.945
cm 5	$C_{p,jet}$	-4.658		
	C_p	-0.488	-4.170	3.310
	$C_{p,t}$	-0.229	-4.429	3.515

As can be seen in the results, the measured pressure differential is not enough to achieve the prescribed momentum addition. It can thus be concluded that in 2D the passive blowing system does not work. This implies that in 3D the system may also not provide enough pressure differential. An advantage in 3D is that the port can be positioned at a different azimuthal positions on the ducted propeller. In 2D azimuthal positions are unavailable, while in 3D a ram port can be placed outside the separated airflow.

5.2. 3D analysis

5.2.1. 3D separation on the ducted propeller

In literature [25], it was discussed that the X22 ducted propeller presented inlet separation at an angle of attack of 40°. This case was recreated with the current setup. The iso-surfaces indicating separation are presented in Figure 5.5. Note that the conditions are similar to the separation indicated in Figure 5.1a and Figure 5.1b. The angle of attack is different, 40° for 3D and 25° for 2D. This difference was explained in subsection 3.5.2.

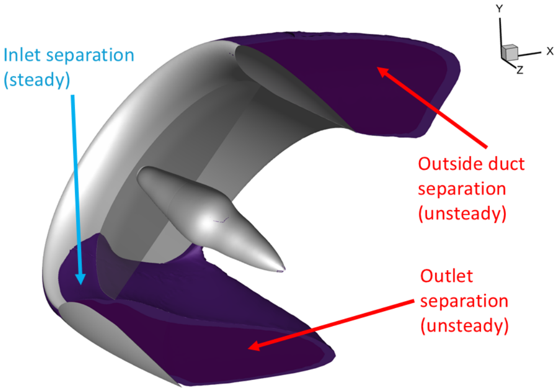

Figure 5.5: Separation indicated by iso-surfaces with v_x = 0 on the baseline duct at v_∞ = 13 m/s, J_∞ = 0.522, α = 40°, $\theta_{0.75}$ = 19°

The separation is quite similar to the 2D case. The centerbody displays less separations, likely influenced by the circular design it has, which the 2D case does not take into account. It can also be observed that the leading edge separation observed in the wind tunnel experiments [25] is also present in Figure 5.5. The discussed unsteady separation regions are indicated as well, however the inlet separation is of interest in this thesis.

5.2.2. Active tangential blowing

To investigate the effectiveness of flow control on a ducted propeller, first the active blowing behaviour is investigated. Three different momentum addition conditions are discussed, C_μ 4%, 5% and 6%. To determine the possible effectiveness, all results will be related to the the baseline duct without blowing slot. For integral evaluations, the distortion factor DC60 will be calculated. The Aerodynamic Interface Plane (AIP) is positioned 1 mm before the fan boundary condition, numerical integration is not possible over the boundary itself. Note that the DC60 involves the most distorted 60° of the AIP, but since this setup only uses a half model the most distorted 30° are taken. Numerically this is equivalent. It was observed that the most distorted region on the AIP was found at the lowest 30°, i.e. the first 30° on the AIP as seen taken from the symmetry plane. In Figure 5.6a, Figure 5.6b, Figure 5.6c and Figure 5.6d the distortion on the AIP for the baseline duct and the blown ducts can be found. The total pressure coefficient, defined in (2.13), is plotted, with 1 being equal to the upstream total pressure coefficient. A $C_{p,t}$ of 1 or higher indicates a flow in which no total pressure is lost with respect to the upstream applied total pressure. Low $C_{p,t}$ indicates a reduced total pressure, which is caused by viscous losses. In the caption the DC60 and the improvement of DC60 over the baseline duct are mentioned.

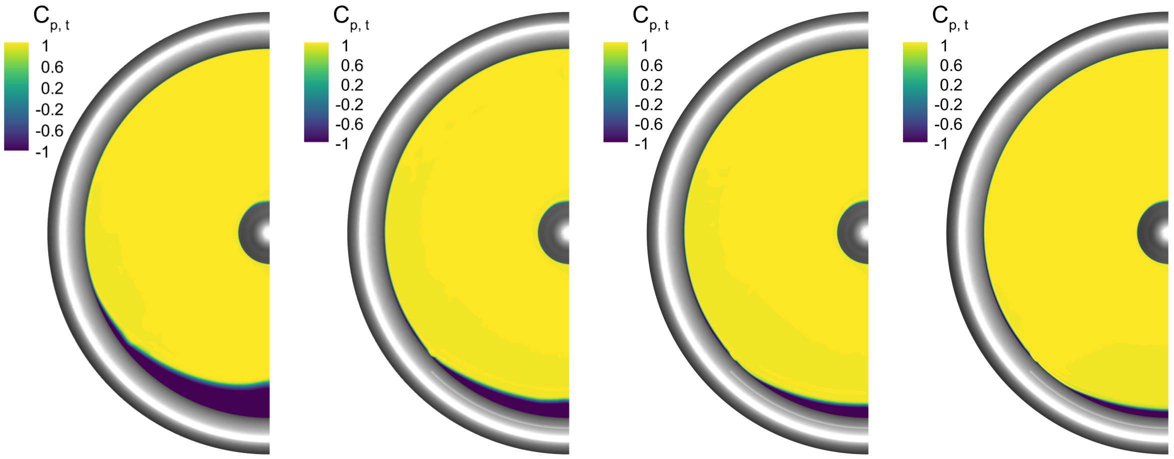

(a) Distortion on the baseline duct DC60 = 0.27

(b) Distortion with $C_\mu = 4\%$ DC60 = 0.14 (-50.3%)

(c) Distortion with $C_\mu = 5\%$ DC60 = 0.09 (-66.4%)

(d) Distortion with $C_\mu = 6\%$ DC60 = 0.06 (-77.6%)

Figure 5.6: Inlet distortion on the AIP at v_∞ = 13 m/s, J_∞ = 0.522, α = 35°, $\theta_{0.75}$ = 19° Active tangential blowing

The figures have also been included in Appendix A for closer inspection . From these figures a number of conclusion can be derived. On the baseline duct, the lower lip exhibits a region of significant viscous losses. In Figure 5.9 the three dimensional streamlines are displayed with the distortion on the AIP for the baseline duct. From this figure it can be deduced that the region with large losses can be associated with separation and a recirculation bubble. This distortion is reduced effectively with the active flow control measure. With a C_μ of 4% the separation can already be reduced significantly. Additional improvement can be made with increasing the momentum addition.

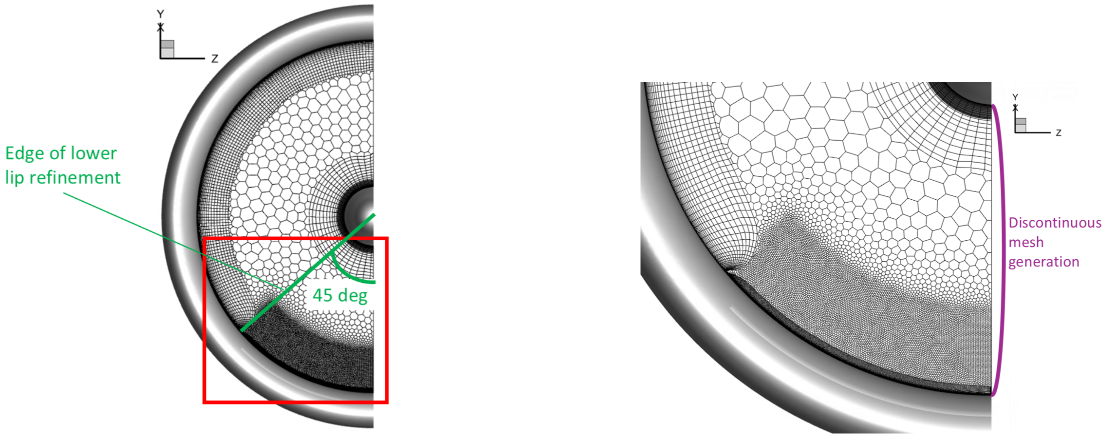

(a) Mesh on the fan boundary. Note the limit of the lower lip refinement. The red zone is enlarged in Figure 5.7b.

(b) Mesh at the edge of the fan boundary. The mesh near the symmetry boundary seems to be discontinuous.

Figure 5.7: Mesh on the fan boundary for the blown ducted propeller setup.

In Figure 5.6a the distortion near the symmetry plane seems to display a non-physical shape. The separation seems to increase in the middle of the duct. It can be reasoned that this is a limitation of the mesh. As Fluent uses a surface mesher before the volume mesher, the mesh is not created in a continuous manner, while the boundary is set to symmetry. This can be seen in Figure 5.7a and Figure 5.7b. A similar distortion deformation can be seen in the passive blowing simulations. Another small effect can be noted at 45° from the symmetry plane. The distortion reduces locally in Figure 5.6a through Figure 5.6d. Coincidentally this is also the location at which the lip refinement is stopped. This would imply that the interaction between the refinement and the rest of the mesh creates some unphysical flow behaviour. However, Nambiar et al. [8] display similar disturbances when using flow control on a nacelle inlet. Their setup used an equally distributed mesh. The results from their simulations are presented in Figure 5.8. Simulations from Hayböck et al. [11] also present non-continuous distortion. The analysis in this reference was done with AJVG, but flow attachment can still be compared. Benjamin et al. [9] present simulations with uneven distortions, indicating the possibility that this problem is not completely symmetric. It can be reasoned from literature, that the distortion may not seem continuous or evenly distributed. This proves that the noted points on the distortion do not necessarily imply an incorrect setup or mesh.

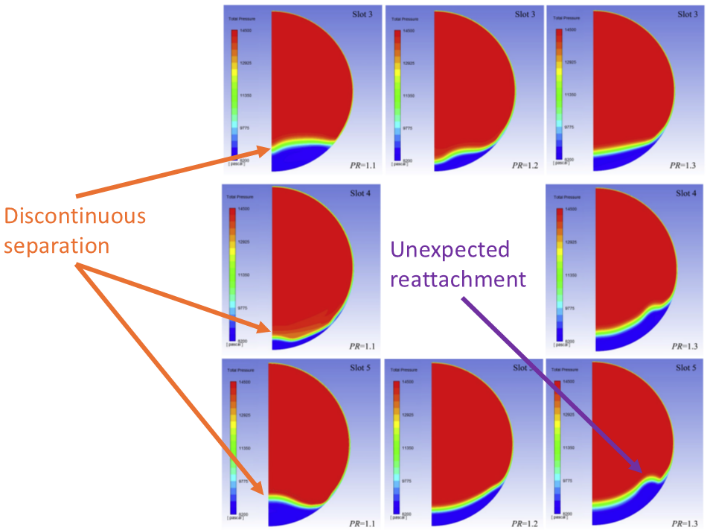

Figure 5.8: Distortion on the fan as found by Nambiar et al. [8]. For a tangentially blown duct inlet, for three different slot designs the distortion is plotted. The nacelle is positioned with 20° angle of attack to a 35000 ft altitude conditions at Mach 0.85. The remarks from the author highlight the same distortions as found in the simulations presented in this thesis.

5.2.3. Passive tangential blowing

To investigate the possible operation of the passive momentum system, the pressure field for the active system was used as a basis. In Figure 5.10 the position of the flush and ram port are presented with jet flow indicated as well. The flush port is positioned in the separated region, as can be seen in comparison with Figure 5.9. It was found that it provided that highest static pressure. It would thus give the highest chance for the passive system to operate effectively.

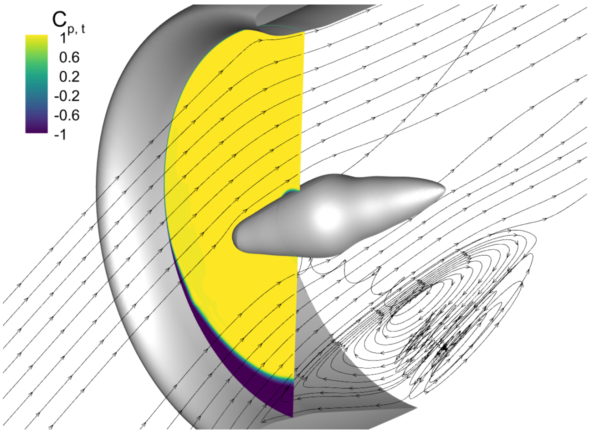

Figure 5.9: Separation and distortion on the baseline duct at v_∞ = 13 m/s, J_∞ = 0.522, α = 35°, $\theta_{0.75}$ = 19°. Streamlines are drawn along the symmetry plane

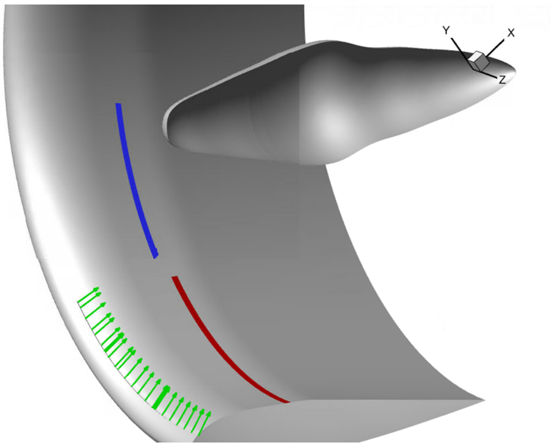

Figure 5.10: Passive ports positioning with respect to the jet flow from the blowing slot. Blue indicates the ram port, while red indicates the flush port.

The flush port is as wide as the blowing slot and has a height 5 times as high as the blowing slot. As discussed earlier, a larger port would not benefit the system more. For the ram port, a similar reasoning is used. As the port utilises total pressure, it was be best to position the port in a region of high total pressure. Using the distortion figure as guide, it was decided that the best option would be to position the port out of the separated wake. This would be between 50° and 80° off of the symmetry plane, the same manner that the 45° for the refinement is established in Figure 5.7a. To achieve the same area as the flush port and thus an area 5 times larger than that of the blowing slot, the height of the ram port was set at 37.5 mm. As the ram port operates with dynamic pressure, it was hypothesised that the ram system would lose effectiveness more quickly when separation spread to the ram port.

The flush and ram ports are geometric zones, but neither is an outlet boundary. Since the pressure differential possible is of interest and not the design of the bleed port, the ports are used as pressure measuring surface. This means that from the internal boundary of the ram port and the wall boundary of the flush port the total and static pressure averages are taken. This pressure is applied to the blowing port with the channel equation. No airflow is bled from the flow in the simulations.

To initialise the simulation for the passive system, the solution for $C_\mu = 4\%$ was used. Using the newly defined port, it was found that in the initial state the ram port would be able to provide enough pressure to achieve $C_\mu = 3.85\%$, while the flush port would only be able to prove enough pressure for $C_\mu = 2.43\%$. Although the initial solution is far from the expected value for the flush system, it would be closer to the solution than a newly initialised solution from the Fluent solver. Once more, the simulation was run for 2 s of flow time to ensure a full resolved flow. During this period the effective C_μ on the blowing slot was reported. This was achieved by averaging the velocity magnitude on the slot and calculating C_μ. It is thus not a calculated value from the channel equation, but a result of applying the channel equation and taking the resulting value from the simulation. In Figure 5.11 the temporal behaviour for the flush and ram ports are displayed.

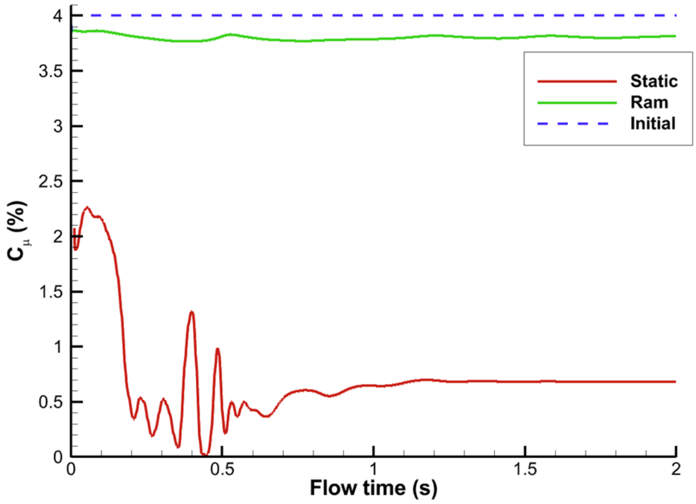

Figure 5.11: C_μ applied over time for flush and ram ports. It can be seen that both systems reach a quasi steady condition. For the flush port the time to resolve is longer, as the initial solution is further from the final solution. The ducted propeller operates at v_∞ = 13 m/s, J_∞ = 0.522, α = 35°, $\theta_{0.75}$ = 19°.

It can be concluded from Figure 5.11 that both the flush and the ram port reach a quasi steady state. This can also be named as a temporally resolved state. It can also be noted that the final effective C_μ for a flush port is much lower than for the ram port. As discussed previously, this was expected, but the final C_μ was significantly lower than was possible in the initial state. The distortion on the AIP was also investigated. The distributions is displayed in Figure 5.12b for the flush port and in Figure 5.12c for the ram port. For reference the modified but unblown duct was also simulated and the distortion is displayed in Figure 5.12a. Note that this duct does not have active blowing but the blowing slot is present on the lip. The displayed improvement for the systems is with respect to the baseline duct.

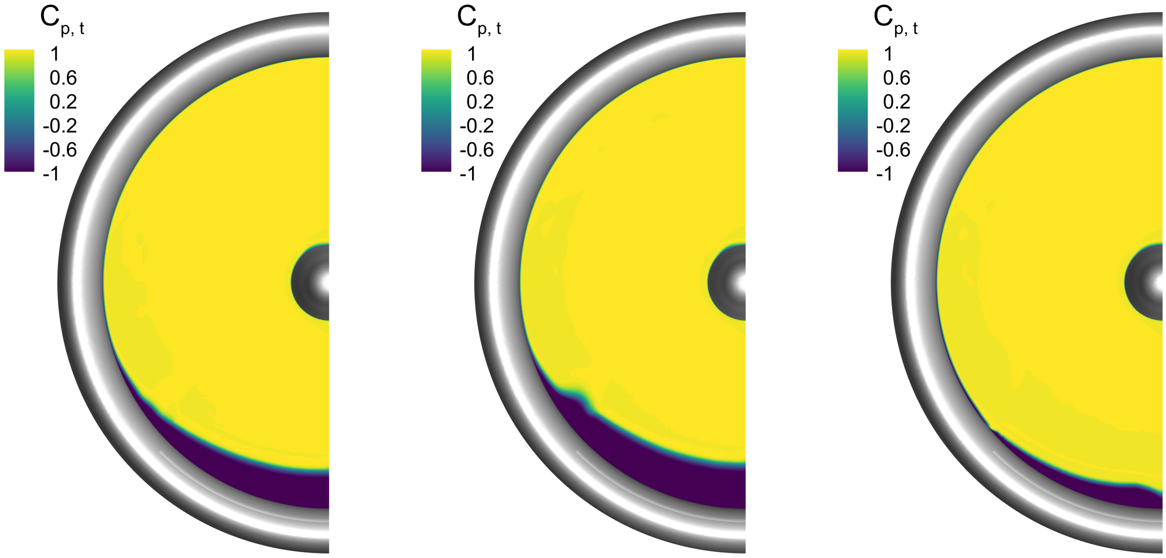

(a) Distortion on the unblown duct
C_μ = 0%, DC60 = 0.27

(b) Distortion with flush port
C_μ = 0.68%, DC60 = 0.34 (+23.3%)

(c) Distortion with ram port
C_μ = 3.8%, DC60 = 0.14 (-50.5%)

Figure 5.12: Inlet distortion on the AIP at v_∞ = 13 m/s, J_∞ = 0.522, α = 35°
Passive tangential blowing

From the figures above a number of conclusions can be taken. From Figure 5.12a it can be concluded that the presence of the slot does not influence the distortion on the AIP significantly. This also implies that this geometry can also function in a deactivated state, without causing additional distortion on the propeller. Note that this conclusion does not apply to an axial flow condition, as it has not been investigated.

Some interesting results can be observed in the distortion for the flush port in Figure 5.12b. Contrary to the expectations and the discussed concepts, the PTB with a flush port increases the distortion on the AIP. The distribution as seen in the figure worsens and the DC60 value over the AIP is increased. This highlights a problem with this type of momentum addition; adding a low amount of momentum to the boundary layer on the brink of separation may induce separation. It is a significant distortion increase of 23%, which raises the question of what induces the separation. Further discussion on this topic will be done in subsection 5.2.4.

Another observation can be taken from Figure 5.12c. The distortion is reduced by the PTB system if a ram port is used. The reduction in distortion is significant and the effective momentum coefficient is quite high. A reduction in DC60 of 50% indicates similar performance when compared to active systems in literature [8]. As no actual port is simulated, the negative effects of the ram port cannot be determined. As it is protruding out of the surface, it can be reasoned that the downstream effects are significant. This thesis focuses on the inlet distortion, so any downstream effects or effects on the performance of the entire propulsion system are considered outside the scope of this research.

As previously stated, the distortion on the AIP is not necessarily continuously distributed. For the baseline duct, distortion on the symmetry plane is noted, while for the ram port the distortion is deflected to the opposite direction. Once more, this is a behaviour seen in the work of Nambiar et al. [8]. As the mesh used in their simulations was more uniform, it is unlikely that the mesh distribution in this simulation causes some of these effects. This would imply the resulting flow field in the simulations of this thesis is more physical than was discussed before. Another reason could be that the separation is more unstable than originally found. The posted results are all snap shots at the end of the simulation time, not time averaged.

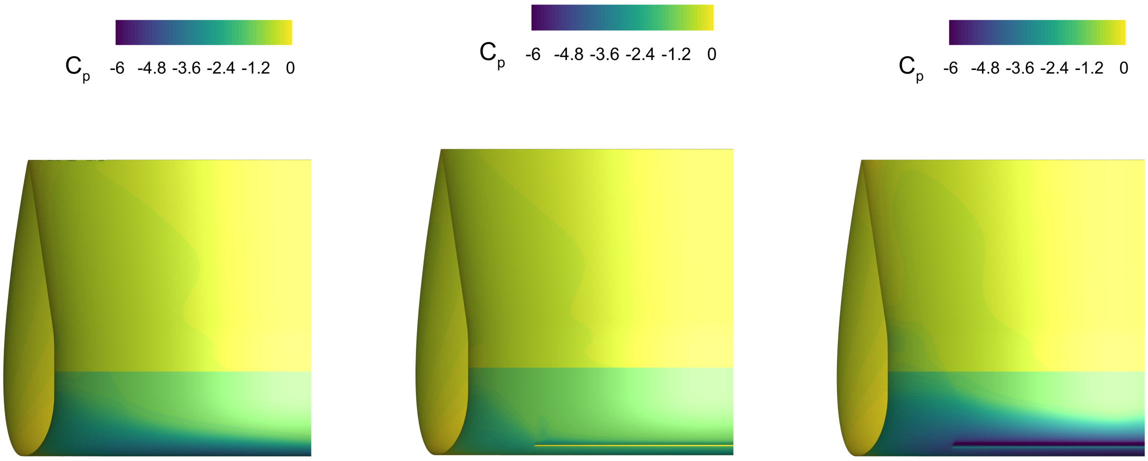

(a) Pressure on the lower baseline duct **(b)** Pressure on the lower duct with flush port **(c)** Pressure on the lower duct with ram port

Figure 5.13: Pressure distribution on the lower duct at v_∞ = 13 m/s, J_∞ = 0.522, α = 35°
Passive tangential blowing

In Figure 5.13a, Figure 5.13b and Figure 5.13c the pressure distribution on the lower duct is indicated for the baseline, flush and ram port cases receptively. The difference between the baseline and the flush blown port seems to small. This can be related to the fact that both cases have leading edge separation. The pressure on the ram passive system displays lower pressures. The flow stays attached longer and is diffused by the curvature more. This would benefit the passive jet, as more airflow can be moved through the channel. The pressure differential over the channel is larger. It can also be observed that the effect of blowing is very low behind the propeller.

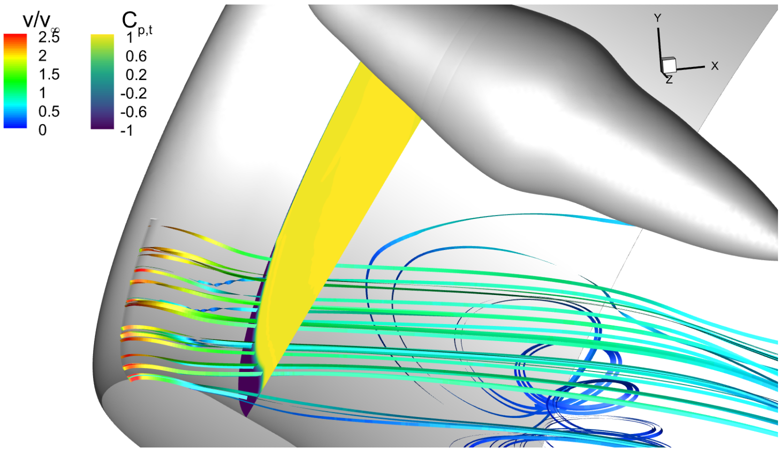

Figure 5.14: The streamlines from the jet with a ram passive system on the ducted propeller with the associated distortion. The streamlines are ribbons coloured by the normalised velocity magnitude. The conditions are the same as in Figure 5.12c. v_∞ = 13 m/s, J_∞ = 0.522, α = 35°

In Figure 5.14, the blown flow from the jet is indicated with streamlines. The colour of the streamline represents the normalised velocity magnitude. The distortion on the AIP is indicated as well. It can be observed that separation of the streamline still occurs before the propeller. The distortion is reduced with respect to the baseline case. Separation still influences that distortion. It can be observed that the flow in the separation region originates from the jet. As was concluded from Figure 5.13a, Figure 5.13b and Figure 5.13c, the effects of this flow control system are not clearly noticeable aft of the propeller. A large separated flow region is still present. As the distorted region on the AIP is smaller, it can be argued that the separated region is reduced in size. The most influential effect of this flow control system is reducing the distortion on the AIP, which was the intention.

5.2.4. Low momentum induced separation

The results in distortion display an increase in separation when low momentum addition is used. To further investigate the separation, the local boundary layer must be discussed. The discussion is best visualised by discussing the differences in boundary layer development. First the unblown boundary layer is discussed. The slot is present here, but the velocity inlet at the jet is set to 0. Note that for each profile in Figure 5.15 an associated velocity profile is plotted in Figure 5.16. Additionally, a streamline is drawn in orange. The local boundary layer thicknesses are calculated for each station, with blue being 1, green 2 and red 3. These are presented in table 5.2. The boundary layer thickness δ is, as previously defined, the point of the highest velocity in the boundary layer without boundary layer control.

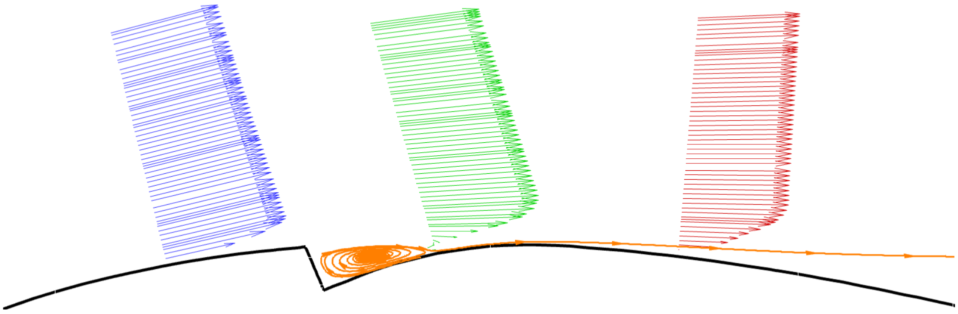

Figure 5.15: Boundary layer development behind the slot with C_μ = 0% associated with the distortion in Figure 5.12a. v_∞ = 13 m/s, J_∞ = 0.522, α = 35°

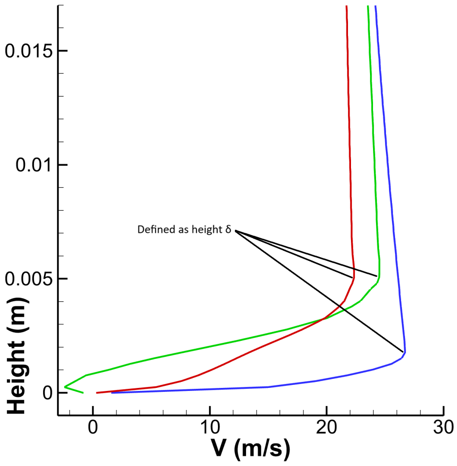

Figure 5.16: Boundary layer velocity profiles with C_μ = 0%, associated with profiles in Figure 5.15.

Table 5.2: Boundary layer thicknesses with C_μ = 0%, associated with profiles in Figure 5.15.

Station	1 (blue)	2 (green)	3 (red)
δ (mm)	1.7	5.5	5.5
$\delta*$ (mm)	0.19	0.49	0.71
θ (mm)	0.38	2.40	1.48
H (-)	1.99	4.88	2.09

The orange streamline displays the profile of a trapped vortex. The geometry gap created by the inactive slot is filled with this trapped vortex, which is driven by the boundary layer moving past. At the slot the shape factor increases, which is due to the reversing flow in the trapped vortex. The shape factor of 2.09 after the slot indicates that the boundary layer is no longer separated and thus reattached. In effect, the boundary layer passes the slot as the boundary layer on the baseline duct would. The boundary layer moves over the trapped vortex and reattaches behind the slot. This explains why the separation performance of the unblown and the baseline ducts are so similar, as the boundary layers perform similarly. In comparison with Figure 5.17 the concept of tangential blowing and the resulting blown boundary layer can be visualised effectively. The boundary layer on the PTB with a ram port is presented.

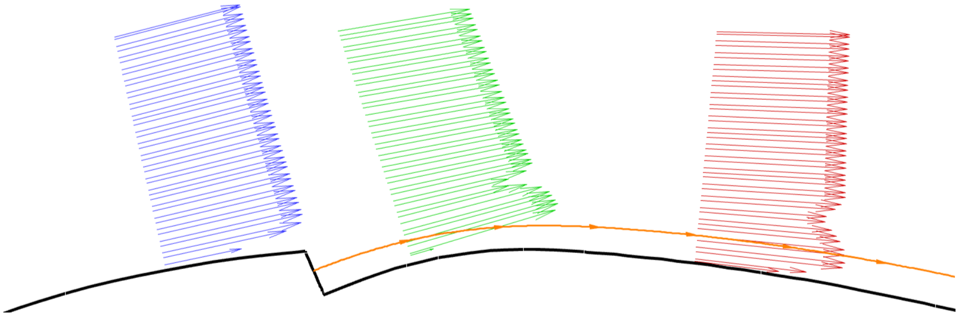

Figure 5.17: Boundary layer development behind the slot with ram air and C_μ = 3.8%

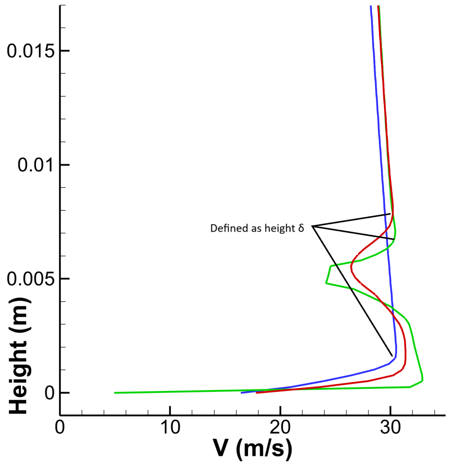

Figure 5.18: Boundary layer velocity profiles with C_μ = 3.8%

Table 5.3: Boundary layer thicknesses with C_μ = 3.8%

Station	1 (blue)	2 (green)	3 (red)
δ (mm)	1.5	7	8
$\delta*$ (mm)	0.16	0.08	0.26
θ (mm)	0.22	0.23	0.32
H (-)	1.39	2.91	1.24

As can be seen, the trapped vortex is blown away, but a new, high momentum boundary layer is positioned underneath the original boundary layer. This high momentum boundary layer is able to pass through the adverse boundary layer more effectively, in turn postponing separation. In Figure 5.18 the high momentum boundary layer mixes with the low momentum of the original boundary layer from the green to red position. With these visualisations of the boundary layer it may be argued that momentum addition does not function by adding momentum to the boundary layer, but by displacing the original boundary layer with a high momentum boundary layer. The result of the blown boundary layer is clearly visualised by the streamline in Figure 5.17, which follows the surface curvature more effectively than in Figure 5.15. The boundary layer thicknesses display the same behaviour. The overall boundary layer thickness δ is larger than for the unblown case. This indicates the displacement of the original boundary layer. However, the momentum and displacement thicknesses are reduced significantly. This can be a mathematical artifact of the assumptions of conservation. However, the shape factor at the last station does display a significant reduction. This implies the boundary layer is delayed in the process of separating. Having discussed the high momentum addition from the ram port, the flush port momentum addition can be compared.

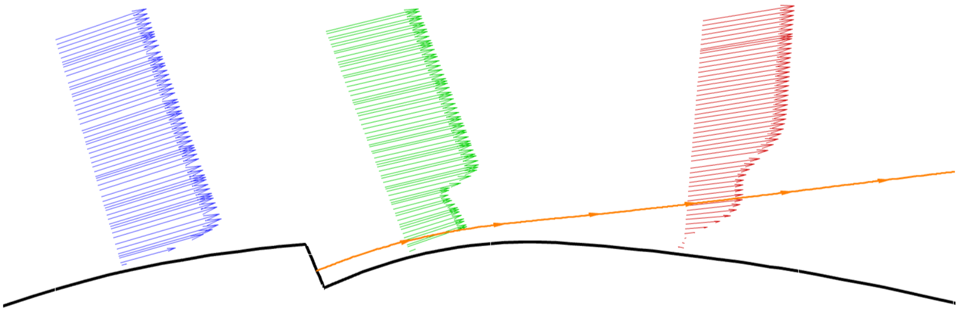

Figure 5.19: Boundary layer development behind the slot with flush air and C_μ = 0.68%

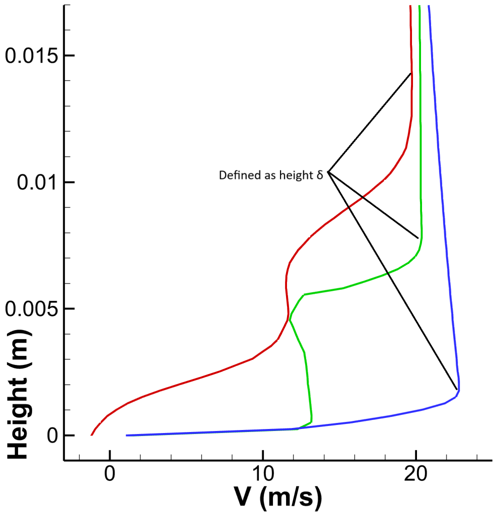

Figure 5.20: Boundary layer velocity profiles with C_μ = 0.68%

Table 5.4: Boundary layer thicknesses with C_μ = 0.68%

Station	1 (blue)	2 (green)	3 (red)
δ (mm)	1.7	10	13
δ^* (mm)	0.19	1.45	1.86
θ (mm)	0.40	2.39	5.03
H (-)	2.07	1.65	2.71

As discussed previously for the higher momentum addition, the blown slot replaces the boundary layer. The same occurs for the flush port, as can be seen in Figure 5.19. However, with the lower momentum blowing the resulting boundary layer has less momentum than the original boundary layer it displaces. In turn the low momentum boundary layer, although undisturbed and uniform at the slot, is unable to move into the adverse pressure gradient. This induces separation, thus exacerbating the distortion on the AIP. Comparing the shape factor H at the last station indicates the problem. With Castillo et al. discussing 2.7 as the separation criterion, the boundary layer would be considered separated. The displacement thickness is increased with respect to the original boundary layer, but the momentum displacement is increased more extremely. This indicates the momentum deficit induced by the low momentum blowing. In conclusion, the low momentum blowing causes the dissolution of the trapped vortex and displaces the original boundary layer with a new low momentum boundary layer, which separates earlier than the original boundary layer does.

5.2.5. Passive blowing at higher thrust setting

To discuss the dependency of the passive systems on the operational conditions it was decided to simulate the ducted propellers with a higher thrust setting. Compared to other conditions and variables, the thrust can be varied effectively and quickly as the prescribed pressure jump can be altered. In Figure 5.21a, Figure 5.21b and Figure 5.21c the distortions for the baseline, flush and ram port are displayed respectively. A logical hypothesis is that the passive systems become more effective when a higher pressure is applied by the propeller. This pressure increases the pressure differential on the channel and thus increases the velocity at the jet. The applied thrust setting is achieved by setting a higher rotational rate for the propeller. DFDC describes a thrust setting of roughly twice the thrust of the previous loading, $T_C = 4.59$ over $T_C = 2.37$.

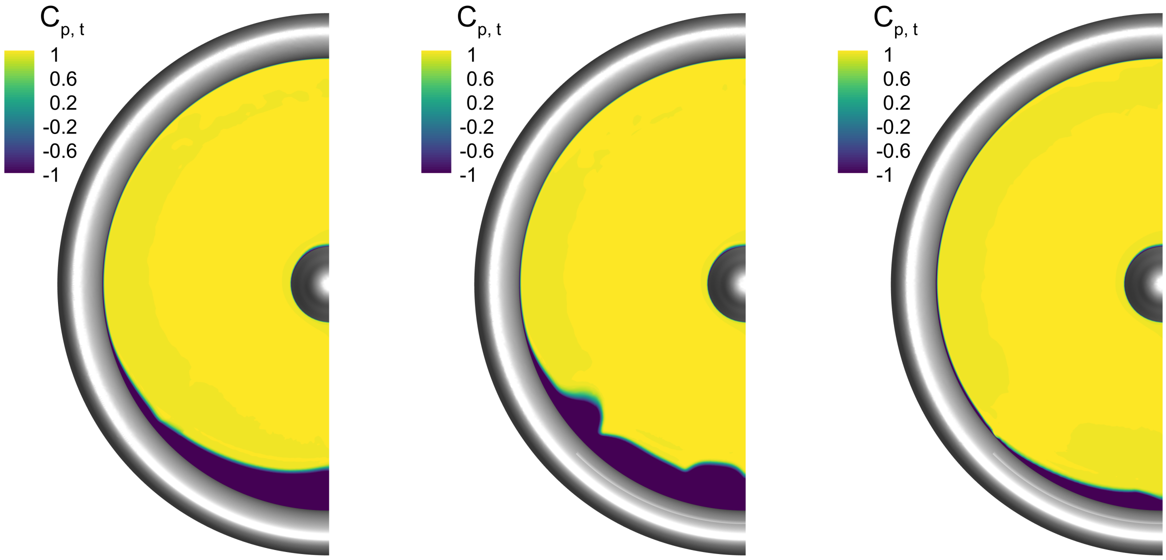

(a) Distortion on the baseline duct duct
DC60 = 0.25

(b) Distortion with flush port
C_μ = 1.8%, DC60 = 0.27 (+8.66%)

(c) Distortion with ram port
C_μ = 6.4%, DC60 = 0.09 (-62.9%)

Figure 5.21: Inlet distortion on the AIP at v_∞ = 13 m/s, J_∞ = 0.522, α = 35°
Passive tangential blowing

During wind tunnel tests of the X22 duct it was found that separation can be postponed by an increase in thrust [19], [25]. A similar effect can be observed in the distortion factor for the baseline duct. Although a reduction in DC60 from 0.27 to 0.25 is not consequential to the investigation, the trend is in general concurrence with the wind tunnel tests. During the wind tunnel tests it was found that at high thrust levels the separation can be eliminated.

The flush port performs similarly as in the lower thrust setting condition, however the DC60 has not increased as significantly. It must however be noticed that the spread of the distortion seems to have altered, a measure not noted with DC60. Instead of a large separated region, two separation bulbs can be noted. The upper bulb can be explained by looking at the added pressure from the jet slot. As discussed previously the low momentum blowing does not add enough momentum to postpone separation. At the edge of the slot the boundary layer is disturbed and momentum is dispersed into lateral direction as well as the normal and axial directions. At the edge the flow exhibits three dimensional behaviour. This means that the newly created low momentum boundary layer from the jet is spread in an additional direction compared the rest of the jetted flow, which only flows downstream. This likely causes the flow at the edge to separate earlier, causing more distortion on the AIP. The relation between the jet flow and the distortion is indicated in Figure 5.22. In red the upstream flow is indicated, while blue indicates flow originating at the jet. It can thus be concluded that the higher bulb of distortion on the AIP is caused by the low momentum boundary layer. Although it is not as visible, a similar bulb can be seen in Figure 5.12b. Here, the problem is likely hidden by the rest of the lower lip exhibiting significant distortion.

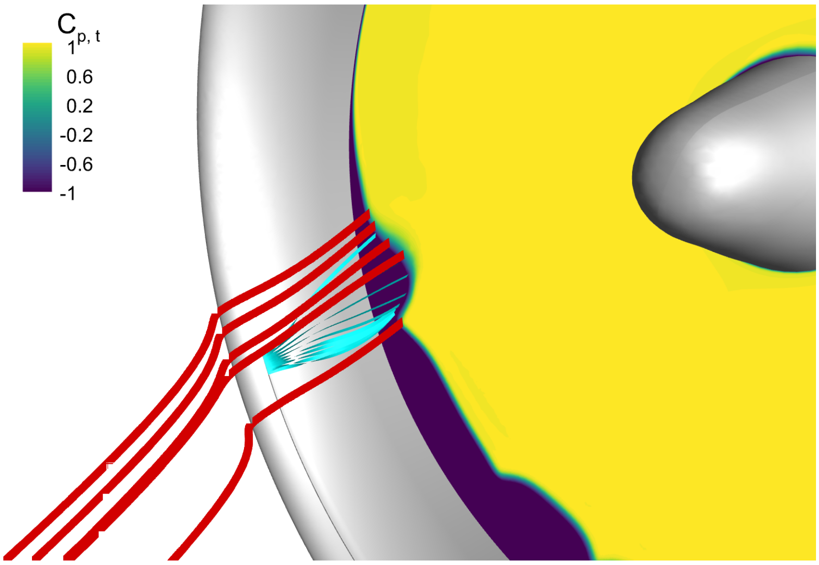

Figure 5.22: Separation induced at the slot edge

The performance of the ram port is increased with a higher thrust setting. The reasoning of an increase in thrust yielding an increase in differential pressure seems to hold as the momentum addition coefficient has increased significantly. However, the added momentum is not proportional to the applied thrust. This implies that even though the pressure applied by the fan is nearly doubled, the pressure differential is not necessarily doubled. A reason could be that the losses in the channel are higher with the higher flow rate through the channel. Another reason could be that the static pressure on the blowing slot has increased, thus requiring the applied total pressure to trade dynamic pressure for static pressure.

6
Conclusions and discussion

In this chapter the conclusions of this thesis will be presented. As previously stated, no conclusions will be taken from the 2D analyses, as the remaining residual imparts a low confidence in the validity of the CFD results. The accuracy of the results from the 3D setup will be discussed in section 6.1. The conclusions from the flow control results are also presented in this section. Conclusions on the results relating to low momentum addition are also discussed. The relevance of the results, the chosen boundary conditions and implications of the effects of certain simplifications are presented also in section 6.2.

6.1. Conclusions

6.1.1. Accuracy of using this setup

Part of this research revolved around the accuracy of the results from the chosen setup. As not all effects on the ducted propeller can be simulated due to computational constraints, the effect of the modelled physics required validation. As was proven, the prescription of a pressure jump on the fan boundary condition operates to an adequate level. Especially as it allows for accurate discussions on the boundary layer behaviour on the inlet of the duct. Limitation arise when discussing on the boundary layer behind the propeller. Effects such as the tip gap, tip vortex and induced swirl are not modelled. Further discussions on these topics are required.

6.1.2. Separation on the Bell X22 ducted propeller

When establishing a reference case for the ducted propeller, the Bell X22 system was chosen due to the presence of publicly available data on the system. Wind tunnel data, performance characteristics and operation manuals are available through public sources. It allowed for accurate validation of the fan model, the pressure jump model and the geometry of the duct. However, as the X22 was designed with VTOL applications in mind, it was reasonable to find that the ducted propeller would be able to operate in VTOL conditions. Wind tunnel data proved that separation on the duct inlet would only be present at high angles of attack [19], [25].

The separation was found to present at an angle of attack of 35°, with leading edge stall at 40°. This flow behaviour is close to what reference data presents [25]. In section 4.3 the pressure distribution for an attached flow was discussed with respect to the wind tunnel data. The separation in Figure 5.5 indicates that separation can be replicated in the same conditions as it was found in the wind tunnel.

During this project it was decided to continue with this design as it was possible to validate the exact design. It does mean that any conclusions in this report will be influenced by the inherent high angle of attack design of the ducted propeller. Compared to ducted propellers and nacelles in axial operation, these angles are very high. This highlights the relevance of the design on the operating window of a ducted propeller design. Other designs may operate at lower angles of attack. The results and discussions presented in this thesis can be related to other systems, but further research with a different ducted propeller system is highly recommended for this purpose.

6.1.3. Active tangential blowing

It was concluded that with the correct positioning and design of the slot, tangential blowing can function as a viable way of postponing separation on a ducted propeller. While literature had discussed this previously, the application in this thesis also proved it can be done with limited momentum addition required. It is comparable with the applied momentum coefficient from Puri et al. [13]. The airfoil discussed in their paper presented separation at a lower angle of attack, namely 18°. This furthermore supports the claim that the results of this thesis can be discussed for other ducted propulsion systems, which operate at lower angles of attack.

6.1.4. Passive tangential blowing

It was found that there is a significant change in the separation reduction of passive tangential blowing using a ram or flush port. The ram port was able to provide significant reduction in distortion of 50% with a momentum addition of 3.8%, comparable to the prescribed momentum addition from the active blowing phase of this thesis. Although the downstream effects of this ram port were not investigated, the benefit of less distortion on the propeller would improve performance more significantly than minor downstream losses would reduce it. It may be argued that this conclusion is not valid for a purely axial flow, in which no separation prevention is required. Here the ram port could negatively impact the performance of the propulsion system.

The passive system with a flush port displayed more 23% distortion than the baseline and the unblown ducts. Part of this problem is due to the low momentum achievable with the flush port. The pressure differential is not enough to postpone separation as effectively as the higher momentum from the ram port is able to. The increase in separation and distortion indicated a problem previously undefined when using momentum addition.

As was expected, the effectiveness of the passive system is better when a higher thrust setting was utilised. Additionally, it was found that the distortion on the baseline duct is also reduced with an increase in thrust. The reason lies in the additional induced velocity on the inlet. When approximating a propeller as a streamtube with an actuator disk, the velocity before the disk already experiences an increase in velocity. This increase in velocity allows the boundary layer to stay attached slightly longer. As the thrust setting was medium to low, the extreme effect of this phenomenon was not investigated, but wind tunnel data displays that the effect becomes more prominent at high thrust settings [19], [25].

Finally, the distortion distribution displayed interesting behaviour for different loading and momentum addition. The distortion was expected to be more evenly distributed. Some distortions could not be explained easily and may indicate limitations of the mesh setup. However, similar effects were found by Hayböck et al. [11] and Nambiar et al. [8]. The work from Nambiar et al. is displayed in Figure 5.8. These papers used different operating conditions, different mesh setups and in some investigations different types of flow control. However, the distortion displayed similar behaviour. Nichols et al. [6] and Erbslöh et al [3]. present other separation distributions in wind tunnel tests. It is thus concluded that while some of the distortion may be caused by the mesh, the general trend of distortions is in line with findings of other papers.

6.1.5. Low momentum addition separation

The increase in distortion when low momentum addition is used, was discussed by investigating the local boundary layer behaviour. Close investigation revealed that the slot in unblown condition is filled with a trapped vortex. This allowed the original boundary layer to reattach. It explained why the distortion on an unblown duct with a slot was similar to the distortion on the baseline duct. With a blown boundary layer, the trapped vortex was lost and the original boundary layer was no longer attached. The newly blown boundary layer is positioned below the original boundary layer. With low momentum addition the newly created boundary layer is of lower overall momentum than the original boundary layer was.

This raises the point of naming convention. During this project the concept of tangential blowing is related to the name of momentum addition. In general this name holds, the conservation of momentum is violated as momentum is added to the flow. However, this added momentum does not present itself as an increase in momentum to the boundary layer. The added flow positions itself underneath the boundary layer and thus can better be formulated as boundary layer displacement. Logically, this implies that the boundary layer can be displaced with a boundary layer of higher or lower momentum. As the widely used momentum coefficient C_μ is related to the velocity applied at the jet, it does not indicate whether it adds momentum by generating a high momentum boundary layer. Using prescribed pressure or pressure ratio PR is an equally complicated solution, as the pressure can present itself as velocity in dynamic pressure or static pressure equal to the local flow field. The use of these variables can thus be very dependent on the local flow field, implying that the same slot on the same duct with the same momentum coefficient may operate differently when applied at a different location.

Results from this thesis point out the difficulty and complexity of this type of boundary layer control. Although it can be very effective, which is presented by the ram port or active tangential blowing, incorrectly applying this technique may significantly worsen the separation one tries to control. Puri et al. also presented a similar occurrence of separation induced by low momentum addition, although their work did not present the inherent origin of this separation. They did present a possible application in the form of vertical wind turbines, which may benefit from controlled separation on an airfoil in the reverse direction [13]. It can thus be concluded that separation induced by blowing can also be used to control the flow, although with the opposite effect of high momentum addition. When designing a tangential blowing system. this effect should be taken under investigation.

6.2. Discussion

6.2.1. Relevance for further research

The conclusions of this report can be used for a multitude of purposes. Initially, one should be cautious with extrapolating information from this thesis, as multiple simplifications were applied. The use of an actual propeller may heavily influence the flow field, especially at the tip gap and with added swirl behind the propeller. As this thesis focused on the behaviour of the boundary layer at the lower lip of the duct, this was known to be a limitation. Now that the passive tangential blowing has proven itself in the simplified condition, a more elaborate analysis can be performed from this point.

Having discussed the relevance of the taken approach, the following points are clear from this thesis. Firstly, it is possible to use high pressure air from behind the propeller to create a stable, effective separation reduction system. The performance of the PTB system with a ram port clearly indicates the viability of this system. Although this system works better than the one with a flush port, no comments can be made about the influence it has downstream. The use of the simplified port did not present the disruption of the flow a real ram port would. The relevance on this topic thus remains: a conceptional version of this PTB with ram port can work and is ready for further analyses.

The second part of interest from this thesis is the investigation on separation induced by a blown boundary layer. The use of low momentum addition and the resulting separation has been presented in other papers. Puri et al. discuss the induced separation as an opportunity for vertical-axis wind turbines [13]. Nambiar et al. display similar induced separation when applying a low pressure ratio at the blowing slot. At low pressure ratios the separation is induced, while higher pressure ratios postpone the separation as intended [8]. Benjamin et al. do not compare the difference between the unblown and low momentum conditions. They do indicate that for low momentum blowing the separation is not reduced [9]. This can be seen in Figure 6.1, where the distortion on the fan, indicated with the blue pressure ratio, is higher on the blown side.

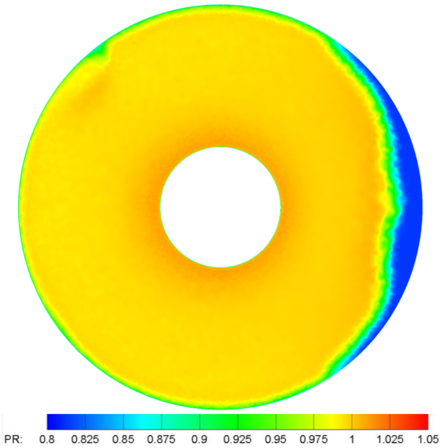

Figure 6.1: Total pressure ratios on the intake-fan for a blowing velocity of 100 m/s. This result from Benjamin et al. [9] displays an ineffective low momentum jet. The intake is a high bypass nacelle intake with 30 kts crosswind.

As this concept has been used in many situations, it is important to note that incorrect use of this separation control may lead to exacerbation of the separation. For future analyses it should be taken into consideration whether the use of this type of flow control is the correct one for achieving the desired goal.

6.2.2. 2D results discussion

In the 2D analyses simulations were run with a steady RANS solver. As the residual in the solution was not reduced to the desired degree, the solutions were considered unconverged. From residual plots it was found that the unconverged flow was present in the region behind the duct. No final conclusions were derived from the solutions in 2D, however the simulations did provide a valuable insight into the performance of the setup and the effectiveness of certain blowing parameters. Conclusions taken from the 2D simulation only directed the 3D analyses. For example, the size of the blowing slot was chosen as 5 mm as this proved more effective in 2D. Another example is that the solver was switched to URANS, as the unconverged solution indicated an unsteady flow.

6.2.3. Boundary conditions considerations

The assumption of incompressible flow seems to hold. In the higher thrust case the maximum velocity for the entire thesis was found. The velocity was 52.3 m/s, which is equivalent to 0.15 Mach at the used flow conditions. This implies the assumption holds. In the beginning of the project it was decided to use an internal fan boundary condition to model the effect of the propeller in the duct. This was considered as an effective and efficient way of understanding the flow on the duct, without the computationally heavy propeller simulation. The use of a fan boundary condition does mean certain effects from the propeller are not correctly simulated. Firstly, the fan boundary condition does not react to the distorted inlet. In reality a propeller blade will experience a different flow when influenced by distortion. The local effective angle of attack on the propeller and thus the local loading may differ due to this distortion. All these effects are unmodelled, as the pressure jump prescribed by DFDC is applied independently of the actual flow field. Another limitation is in the added swirl. No swirl induced by the propeller was prescribed to the fan boundary condition. It may influence the downstream flow field, including the ports. In turn, this could influence the behaviour of the passive momentum system. The fan model also spreads the pressure jump from the propeller blade over the entire fan disk. In reality, the propeller would apply a large pressure in a periodic motion. With the used model this effect is not simulated.

The fan boundary condition also incorrectly modelled the tip gap on the propeller. Due to the experienced fan-induced separation, the tip gap was closed and the boundary layer was also subject to the pressure jump. This does influence the operation of the passive flow back system, as the boundary layer used in the ports, both ram and flush, has been affected by the increase in pressure at the fan. This likely influenced the effectiveness of the system, as a high pressure differential can be found. It can however be argued that the use of a fan boundary condition is already unable to correctly model the tip gap effects in a ducted propeller. As the duct is supposed to reduce the effect of tip losses, the tip interaction would function differently than on an open propeller. However, this interaction, causing a tip vortex, is completely unmodelled with the fan boundary condition. The resulting vortex would interact with the port positioned behind it. As this channel is modelled, not simulated, the effects here can also not be discussed with this setup. A fully operational version of the passive tangential blowing system would require more accurate and higher fidelity solutions.

The effect of the upstream boundary condition has been discussed in chapter 4. As the pressure distribution is less than half a percent non-uniform, it was discussed as a minimal problem. However, with CFD purely uniform boundary conditions are possible. Therefore the incorrect boundary condition should be mentioned in this discussion as well. The final boundary condition that should be discussed is the blowing slot. In the active phase this blowing slot was used as a velocity inlet, as the jet velocity was prescribed. In the passive phase it was replaced with a total pressure inlet. The result for both was that a uniform applied velocity is used at the boundary. During the airfoil analyses in the beginning of the project this was also utilised and it proved to be as accurate as a boundary condition applied further into the blowing slot. However, it can be argued that, although the overall macro effects are similar, the boundary condition should be defined differently when analysing the boundary layer on the inlet more closely. In reality, the flow field in the jet has boundary layers from the movement through the channel.

6.2.4. Channel flow influence

The usage of the channel flow equation for the passive tangential blowing plays a crucial role in the analyses of the system. The use of a single equation for this purpose has been chosen since the flow through a channel is well understood. Additionally, the choice for an equation rather than a meshed channel reduced the computational demand during this project. However, the channel has been simplified significantly as a result. The temporal effect of the channel is ignored and a pressure applied at the port is directly applied at the jet as well. The solution seems to resolve to a steady condition, but when a rotating propeller is modelled this will become unsteady. The time for the flow to pass through the channel will have to be implemented accordingly. Reference material has looked into using unsteady flow control, however this is mostly done in combination with an air jet vortex generator. Hayböck et al. [11] found that using periodic blowing can operate less efficiently than continuous blowing, as no stable vortex can be generated. This could be a similar problem when the propeller is passing periodically. Every time the momentum addition reduces, separation can be worsened as was found with the low momentum induced separation.

Additionally the implementation of a propeller will also introduce a vortex from the tip of the blade. As it is not under consideration in this thesis, it is unknown how this vortex will interact with a flush or ram port. It could be that the vortex has either a beneficial or opposite effect on the pressure in the channel. The vortex may actually funnel into the channel and travel to the jet. This behaviour has not been considered in this thesis, but should be further discussed when implementing a more complete higher fidelity model.

The final effect not modelled with the channel equation is the bend losses. When a flow moves through a channel or pipe with a bend, losses present. This is especially true for tight bends. In the channel from the ram port and the channel to the jet, very tight bends could be present. These losses could not be analysed as no design is known for this problem. It is argued that the losses reduce the effective momentum addition possible with a passive momentum system. However, as the friction losses were comparatively low, the bend losses were considered negligible.

7
Recommendations

During the research performed in this thesis certain additional research questions were identified. The limitations of the setup of the analyses were also found and their implications were discovered. Recommendations on further research about this subject are presented in section 7.1. These recommendations mostly discuss the additional information that can be found on the topics discussed in this thesis with a different numerical setup. Results from this thesis can also be applied to a wider field of research. Recommendations on other applications are found in section 7.2.

7.1. Recommendations on further research

To further investigate the performance of the passive tangential blowing it is highly recommended to enhance the current setup first. The noted limitations should be removed to display the dependency of the results on these limitations and simplifications. Firstly, the limitation of the half model may not have played a role in a physical sense when using an actuator disk. However, it was found that the Ansys Fluent mesher does not allow the mesh to be properly continuous. The symmetry plane was given a surface mesh on which the volume mesh was generated. It would be recommended to investigate if the distortion changes if a full model is meshed.

Changing to a full model also opens the possibility of using a rotating pressure jump. In wind energy analyses the rotation of a blade is modelled with a rotating actuator line. While the actuator disk model spreads the pressure jump over the entire disk, an actuator line model sources the pressure jump at the position of the blade and lets this jump rotate. It allows for an analysis of all behaviours of the propeller, swirl and temporal behaviour, while limiting the mesh size as no propeller blades are simulated. The mesh would double in size compared to the setup discussed in this paper, but the pressure jump at the disk would still provide a reduced effort solution for this investigation. Using an actuator line may also prove to reduce fan-induced separation and would allow for a closer investigation of the tip gap effect on the performance of the passive tangential blowing system. It does require a small time step to yield accurate results. However, as the simulations in this paper are already using a URANS solver, this would increase computational time, but would not add complexity in terms of setup.

To completely investigate the effects of distortion on the propeller it is recommended to investigate this system with full blade modelling. This can be done with a rotating reference frame, locally adding a rotation to the flow. This solution can influence the swirl from the propeller, as this rotation is removed once flow flows out of the rotating frame region. The more complicated, but more accurate solution would require a rotating mesh around the blade. The complexity lies in the mesh size with the small time steps required for a rotating mesh option. Using a rotating mesh would only be recommended if limitations are found with an actuator line that can influence results. It can be argued that the use of an actuator line can reflect the swirling flow better than a rotating frame simulation could. Therefore it is highly recommended to not use blade meshing as a following step, but investigate the option of the rotating actuator line in depth.

7.2. Recommendations on wider research

During this simulation the ducted propeller from the Bell X22 was used as a reference case. This particular reference case exhibits a few design choices that influence the results significantly. Firstly, the ducted propeller is designed for VTOL applications, as discussed previously. As was noted, this implies that not all results can be extrapolated as easily to a different ducted propeller which may be optimised for axial flight. This limitation was known from the start, but with the setup discussed in this thesis it is recommended to investigate the application of the PTB system for a propulsion system more optimised for axial flight. As discussed in the literature review, active flow control may allow rounded inlets on ducts and nacelles to have a smaller leading edge radius. This would in turn reduce drag in high Reynolds number and high Mach number conditions. It is recommended to discuss the setup of this thesis on a ducted propeller with a thinner lip.

This also presents the possibility of optimising the tangential blowing system more accurately. As discussed, many papers are discussed and many different designs have proven to perform adequately. The position of the jet slot can be varied, which may benefit the performance of the momentum added to the flow. The position may also vary with the design of the duct. Different pressure and velocity distributions can influence the performance of the tangential blowing system. One can also discuss the operation of jetting orthogonal to the surface. Papers indicate that an Air Jet Vortex Generator can achieve similar results as tangential blowing with a lower pressure.

Finally, it is recommended to apply the PTB to nacelles of turbofan aircraft. This paper discusses a ducted propeller, but in practice similar problems arise on turbofan nacelles. The closed tip gap assumption in this thesis may hold more accurately on a turbofan which have relatively small tip gaps. The use of an actuator disk may also be more applicable to a fan or an axial compressor. This implies one can discuss the tangential blowing on a nacelle with this setup, without the need for significant changes to the setup.

References

[1] T. Jiang, Y. Liu, and Y. Zheng, “Ducted fan design for vtol aircraft flight mission based on bayesian optimization,” *Journal of Aircraft*, pp. 1–12, DOI: `10.2514/1.C037541`.

[2] B. Mohankumar, C. A. Hall, and M. J. Wilson, “Fan aerodynamics with a short intake at high angle of attack,” *Journal of Turbomachinery*, vol. 143, no. 5, Mar. 2021. DOI: `10.1115/1.4050606`.

[3] S. Erbsloeh and W. Crowther. “Control of boundary layer separation on a civil turbofan intake using air-jet vortex generators.” (2015), [Online]. Available: `https://www.researchgate.net/publication/228413753`.

[4] S. Erbsloeh, W. Crowther, and J. Frutos, “Control of compressor face total pressure distortion on a high bypass turbofan intake using air-jet vortex generators,” in *2nd AIAA Flow Control Conference*. 2004. DOI: `10.2514/6.2004-2206`.

[5] D. A. Nichols, B. Vukasinovic, A. Glezer, M. C. DeFore, B. Rafferty, and F. D. Palacios, “Characterization and control of nacelle inlet flow in crosswind,” in *AIAA Aviation 2019 Forum*. 2019. DOI: `10.2514/6.2019-3685`.

[6] D. A. Nichols, B. Vukasinovic, A. Glezer, M. C. DeFore, and B. Rafferty, “Fluidic control of nacelle inlet flow in crosswind,” in *AIAA AVIATION 2020 FORUM*. 2020. DOI: `10.2514/6.2020-2955`.

[7] C. T. Wakelam, T. P. Hynes, H. P. Hodson, S. W. Evans, and P. Chanez, “Separation control for aeroengine intakes, part 1: Low-speed investigation of control strategies,” *Journal of Propulsion and Power*, vol. 28, no. 4, pp. 758–765, 2012. DOI: `10.2514/1.B34326`.

[8] V. R. Nambiar and V. Pachidis, “Nacelle intake flow separation reduction at cruise condition using active flow control,” *Propulsion and Power Research*, vol. 11, no. 3, pp. 337–352, 2022, ISSN: 2212-540X. DOI: `https://doi.org/10.1016/j.jppr.2022.07.005`.

[9] L. Benjamin and J. Friedrichs, “Numerical evaluation of active flow control concepts for short ultra-high-bypass-ratio engine intakes,” in *AIAA AVIATION FORUM AND ASCEND 2024*. 2024. DOI: `10.2514/6.2024-3919`.

[10] A. Johns, R. Williams, and H. Potonides, “Performance of a v/stol tilt nacelle inlet with blowing boundary layer control,” in *15th Joint Propulsion Conference*. 1979. DOI: `10.2514/6.1979-1163`.

[11] S. Hayböck and C. Breitsamter, “Implementation of active flow control on a short-inlet uhbr engine nacelle,” in *34th Congress of the International Council of the Aeronautical Sciences, ICAS 2024*, International Council of the Aeronautical Sciences, 2024. [Online]. Available: `https://www.scopus.com/inward/record.uri?eid=2-s2.0-85208806975&partnerID=40&md5=f365b518359d5c992aad637a4d6d8faa`.

[12] D. Borgmann, A. Pande, J. C. Little, and R. Woszidlo, “Experimental study of discrete jet forcing for flow separation control on a wall mounted hump,” in *55th AIAA Aerospace Sciences Meeting*. 2017. DOI: `10.2514/6.2017-1450`.

[13] K. Puri, M. Laufer, H. Müller-Vahl, D. Greenblatt, and S. H. Frankel, “Computations of active flow control via steady blowing over a naca-0018 airfoil: Implicit les and rans validated against experimental data,” in *2018 AIAA Aerospace Sciences Meeting*. 2018. DOI: `10.2514/6.2018-0792`.

[14] L. Prandtl, “Applications of modern hydrodynamics to aeronautics,” NASA/Göttingen University, Tech. Rep., 1923. [Online]. Available: `https://ntrs.nasa.gov/citations/19930091180`.

[15] T. Burton, N. Jenkins, D. Sharpe, and E. Bossanyi, “Aerodynamics of horizontal axis wind turbines,” in *Wind Energy Handbook*. John Wiley & Sons, Ltd, 2011, ch. 3, pp. 39–136, ISBN: 9781119992714. DOI: `https://doi.org/10.1002/9781119992714.ch3`.

[16] E-33 In Flight Propulsion Measurement Committee, *Propeller/propfan in-flight thrust determination*, May 2012. DOI: `https://doi.org/10.4271/AIR4065A`.

[17] H. F. Bento, R. de Vries, and L. L. Veldhuis, “Aerodynamic performance and interaction effects of circular and square ducted propellers,” in *AIAA Scitech 2020 Forum*. 2020. DOI: `10.2514/6.2020-1029`.

[18] D. M. Black, R. C., and H. S. Wainauski, “Shrouded propellers - a comprehensive performance study,” in *5th Annual Meeting and Technical Display*. DOI: `10.2514/6.1968-994`.

[19] K. W. Mort and B. Gamse, “A wind-tunnel investigation of a 7-foot- diameter ducted propeller,” NASA, Tech. Rep., 1967. [Online]. Available: `https://ntrs.nasa.gov/citations/19670025554`.

[20] D. S. Douglas, S. Mills, and E. Kisielowski, “Comparative performance study of propeller, ducted propeller and turbofan propulsion systems,” US Army Aviation Materiel Laboratories, Tech. Rep., 1968.

[21] J. L. Pereira, “Hover and wind-tunnel testing of shrouded rotors for improved micro air vehicle design,” Ph.D. dissertation, University of Maryland, College Park, Jan. 2008.

[22] S. Yilmaz, D. Erdem, and M. Kavsaoglu, “Effects of duct shape on a ducted propeller performance,” in *51st AIAA Aerospace Sciences Meeting including the New Horizons Forum and Aerospace Exposition*. 2013. DOI: `10.2514/6.2013-803`.

[23] R. Bontempo and M. Manna, “Effects of duct cross section camber and thickness on the performance of ducted propulsion systems for aeronautical applications,” *International Journal of Aerospace Engineering*, vol. 2016, Feb. 2016. DOI: `10.1155/2016/8913901`.

[24] D. Szondy. “E-fan electric aircraft makes first public flight.” Last visited: 15-08-2025. (2014), [Online]. Available: `https://newatlas.com/e-fan-airbus-electric-plane/31823/`.

[25] A. R. Kriebel and M. R. Mendenhall, “Predicted and measured performance of two full-scale ducted propellers,” NASA, Tech. Rep., 1966. [Online]. Available: `https://ntrs.nasa.gov/citations/19660027014`.

[26] Bell Aerosystems Company, “Demonstration planning and progress report,” Bell Aerospace Corporation, Tech. Rep., 1967. [Online]. Available: `https://apps.dtic.mil/sti/tr/pdf/AD0447814.pdf`.

[27] H. C. Marquardt, “X-22a tri-service v/stol aircraft - final progress report,” Bell Aerospace Company, Tech. Rep., 1969.

[28] H. Schlichting and K. Gersten, “Boundary–layer equations in plane flow; plate boundary layer,” in *Boundary-Layer Theory*. Berlin, Heidelberg: Springer Berlin Heidelberg, 2017, pp. 145–164, ISBN: 978-3-662-52919-5. DOI: `10.1007/978-3-662-52919-5_6`.

[29] F. M. White and J. Majdalani, *Viscous fluid flow*, fourth. McGrraw Hill, 2022.

[30] L. Castillo, X. Wang, and W. K. George, “Separation criterion for turbulent boundary layers via similarity analysis,” *Journal of Fluids Engineering*, vol. 126, no. 3, pp. 297–304, Jul. 2004, ISSN: 0098-2202. DOI: `10.1115/1.1758262`.

[31] A. Batikh, L. Baldas, and S. Colin, “Application of active flow control on aircrafts -State of the art,” in *International Workshop on Aircraft System Technologies*, Hamburg, Germany, Feb. 2017. [Online]. Available: `https://hal.science/hal-01820331`.

[32] G. B. Schubauer and W. G. Spangenberg, “Forced mixing in boundary layers,” *Journal of Fluid Mechanics*, vol. 8, no. 1, pp. 10–32, 1960. DOI: `10.1017/S0022112060000372`.

[33] H. Schlichting and K. Gersten, “Boundary-layer control (suction/blowing),” in *Boundary-Layer Theory*. Berlin, Heidelberg: Springer Berlin Heidelberg, 2017, pp. 291–320, ISBN: 978-3-662-52919-5. DOI: `10.1007/978-3-662-52919-5_11`.

[34] M. Gad-el-Hak and D. M. Bushnell, “Separation control: Review,” *Journal of Fluids Engineering*, vol. 113, no. 1, pp. 5–30, Mar. 1991. DOI: `10.1115/1.2926497`.

[35] K. B. M. Q. Zaman, A. Bar-Sever, and S. M. Mangalam, “Effect of acoustic excitation on the flow over a low-re airfoil,” *Journal of Fluid Mechanics*, vol. 182, pp. 127–148, 1987. DOI: `10.1017/S0022112087002271`.

[36] M. Winter and A. K. Jain, “Gas turbine engine system providing simulated boundary layer thickness increase,” U.S. Patent US 8209953 B2, Jul. 3, 2012.

[37] V. Kumar and F. S. Alvi, “Use of high-speed microjets for active separation control in diffusers,” *AIAA Journal*, vol. 44, no. 2, pp. 273–281, 2006. DOI: `10.2514/1.8552`.

[38] E. A. Whalen, M. Spoor, P. M. Vijgen, *et al.*, “Full-scale flight demonstration of an active flow control enhanced vertical tail,” in *8th AIAA Flow Control Conference*. 2016. DOI: `10.2514/6.2016-3927`.

[39] K. R. Saripalli and R. L. Simpson, “Investigation of blown boundary layers with an improved wall jet system,” NASA, Tech. Rep., 1980.

[40] C. VanSickle, D. R. Cuppoletti, R. Manek, *et al.*, “Boundary layer control with a shallow inclined wall injector,” in *AIAA AVIATION FORUM AND ASCEND 2024*. 2024. DOI: `10.2514/6.2024-3633`.

[41] K. Xu, Y. Ren, and G. Zha, “Separation control by co-flow wall jet,” in *AIAA AVIATION 2021 FORUM*. 2021. DOI: `10.2514/6.2021-2946`.

[42] T. Surply and C. Bourdeau, “Turbojet nacelle and method for controlling separation in a turbojet nacelle,” U.S. Patent US 8640986 B2, Feb. 4, 2014.

[43] Y. Qian, Y. Luo, X. Hu, Z. Zeng, and Y. Zhang, “Improving the performance of ducted fans for vtol applications: A review,” *SCIENCE CHINA Technological Sciences*, vol. 65, no. 11, pp. 2521–2541, 2022. DOI: `https://doi.org/10.1007/s11431-021-2110-x`.

[44] M. Drela and H. Youngren, “Axisymmetric analysis and design of ducted rotors,” MIT, Tech. Rep., Dec. 2005. [Online]. Available: `https://web.mit.edu/drela/Public/web/dfdc/DFDCtheory12-31.pdf`.

[45] R. Nederlof, D. Ragni, and T. Sinnige, “Experimental investigation of the aerodynamic performance of a propeller at positive and negative thrust and power,” in *AIAA AVIATION 2022 Forum*. DOI: `10.2514/6.2022-3893`.

[46] G. D. Stich, L. Fernandes, J. Duensing, G. Kenway, J. Housman, and C. Kiris. “Validation of actuator disk, actuator line and sliding mesh methods within the structured curvilinear overset solver.” (2022), [Online]. Available: `https://www.nas.nasa.gov/assets/nas/pdf/ams/2022/AMS_20220825_Stich.pdf`.

[47] M. Hepperle, *Javaprop user’s guide*, Aug. 2018. [Online]. Available: `https://www.mh-aerotools.de/airfoils/java/JavaProp%20Users%20Guide.pdf`.

[48] A. Talmon. “Basic principles of flow of liquid and particles in a pipelines.” TU Delft Open Courseware. (2023), [Online]. Available: `https://ocw.tudelft.nl/wp-content/uploads/B._oe4625_Chapter01.pdf`.

[49] A. Akturk and C. Camci, “Tip clearance investigation of a ducted fan used in vtol unmanned aerial vehicles- part i: Baseline experiments and computational validation,” *Journal of Turbomachinery*, vol. 136, pp. 021 004–1, May 2022. DOI: `10.1115/1.402346`.

[50] A. Deperrois. “Theoretical limitations and shortcomings of xflr5.” (2019), [Online]. Available: `https://www.xflr5.tech/docs/Part%20IV:%20Limitations.pdf`.

[51] T. Sinnige, N. Van Arnhem, T. Stokkermans, R. De Vries, and B. Della Corte. “Tud data sets on propeller integration.” (2020), [Online]. Available: `https://filelist.tudelft.nl/Websections/Propeller%20Aerodynamics/TUD_propIntegrationResearch_Overview.pdf`.

A

Figures

This appendix contains figures and data used for this thesis, but not discussed in text.

The ducted propeller discussed in this thesis is based on the system of the Bell X22. The duct design data is presented in Figure A.1. The design of the propeller is described in Figure A.2. These figures are taken from the work of Mort et al. [19]. Note that this thesis did not create structural elements in the duct, and that the spinner and centerbody in the reference are smoothend to reduce separation on this section of the design. This separation was not of interest and only increased numerical complexity.

In Figure A.4, the forces over the duct and spinner and the lower lip are presented. The coordinate system is presented in Figure A.3, as is the lower lip zone. It can be determined that the improvement from the mid mesh to fine mesh is larger than from fine to superfine. Note that the refinement is altered mostly around the lower lip. In conclusion, the fine mesh was considered as a good mesh for this application.

The figures described in section 5.2 may be considered small for close inspection. For this purpose Figure 5.6a through Figure 5.6d are enlarged in this appendix.

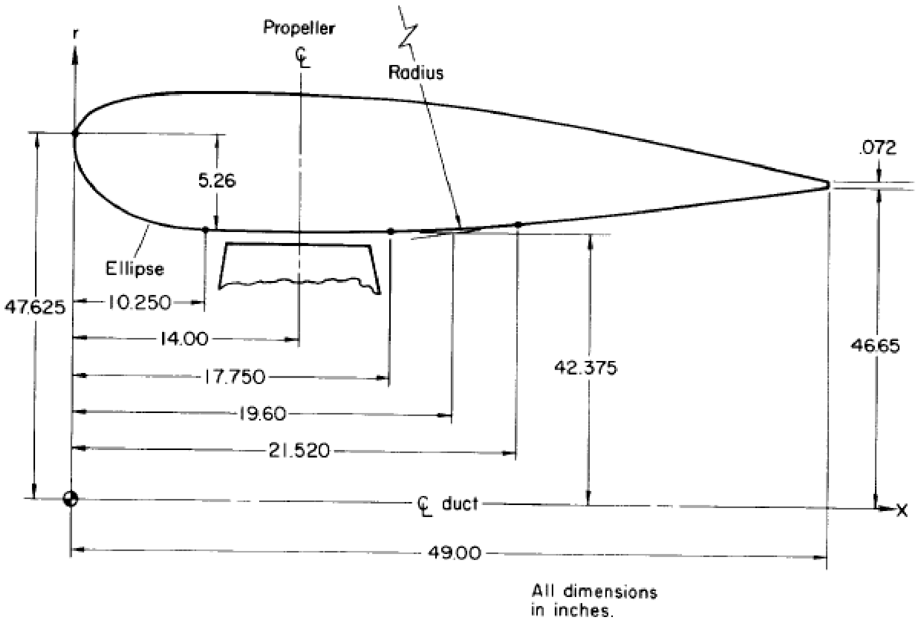

Outside surface ordinates	
X	r
0	47.625
.613	48.695
1.225	49.096
2.450	49.609
3.675	49.953
4.900	50.205
7.350	50.535
9.800	50.710
10.250	–
12.250	50.779
14.700	50.763
17.750	–
19.600	50.552
23.700	–
24.500	50.164
29.400	49.649
34.300	49.038
39.200	49.344
44.100	47.576
46.550	47.160
49.000	46.722

Pressure orifice location		
Number	Location, percent chord	
	Inside	Outside
1	0	
2	1	
3	2.5	
4	5	
5	10	
6	15	
7	25	
8	35	
9	50	
10	70	
11	90	
12		90
13		70
14		50
15		35
16		25
17		15
18		5
19		1.8

Figure A.1: Bell X22 ducted propeller systems design. Duct design values as presented by Mort et al. [19]. Note that the inside of the duct is generated with geometric shapes, while the outside of the duct is defined by coordinates. In this thesis the outside is recreated with a spline through these coordinates. The duct is axisymmetric.

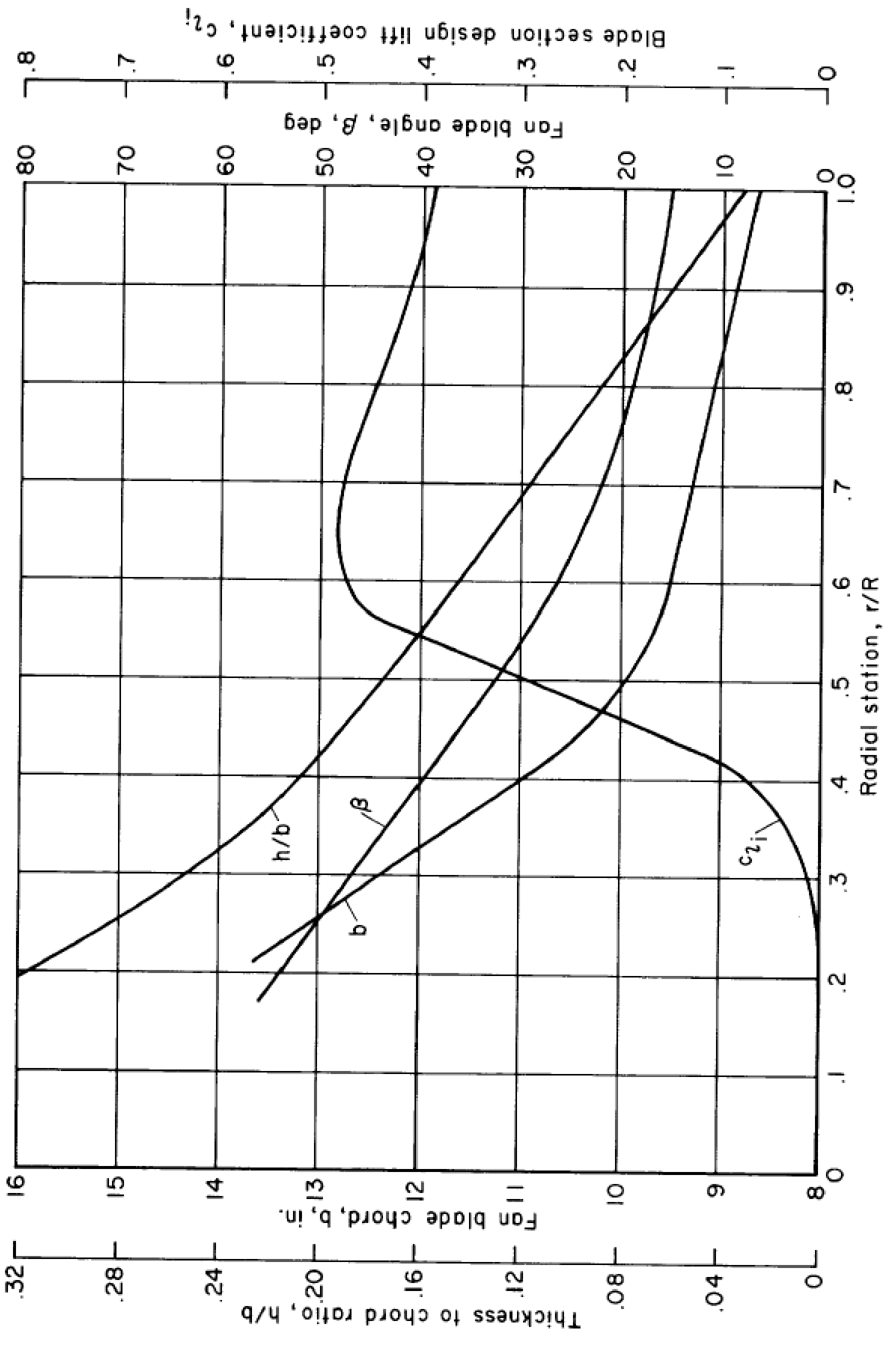

Figure A.2: Bell X22 ducted propeller systems design. Propeller design values as presented by Mort et al. [19]. The airfoil shapes are not found, but the design lift coefficient $C_{l,i}$ and thickness to chord $\frac{t}{c}$ are matched with NACA 4-series airfoils. For this four airfoils are used, from root to tip, 2430, 2425, 2413, 2408.

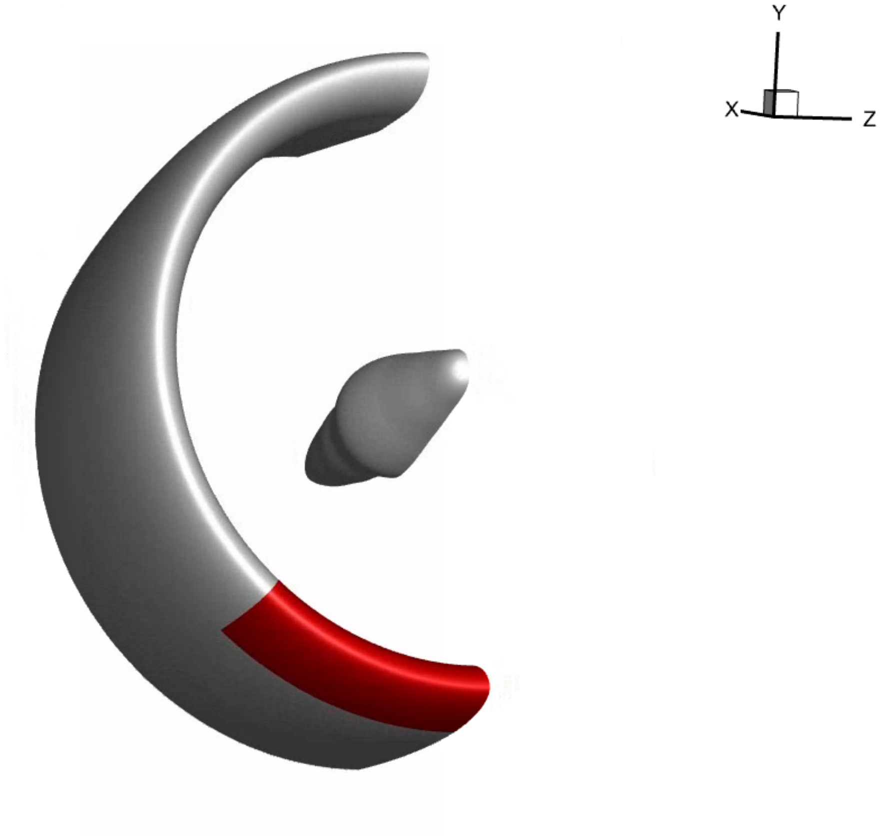

Figure A.3: The surface zones used in this thesis. The coordinates system used for the drag and lift direction in Figure A.4.

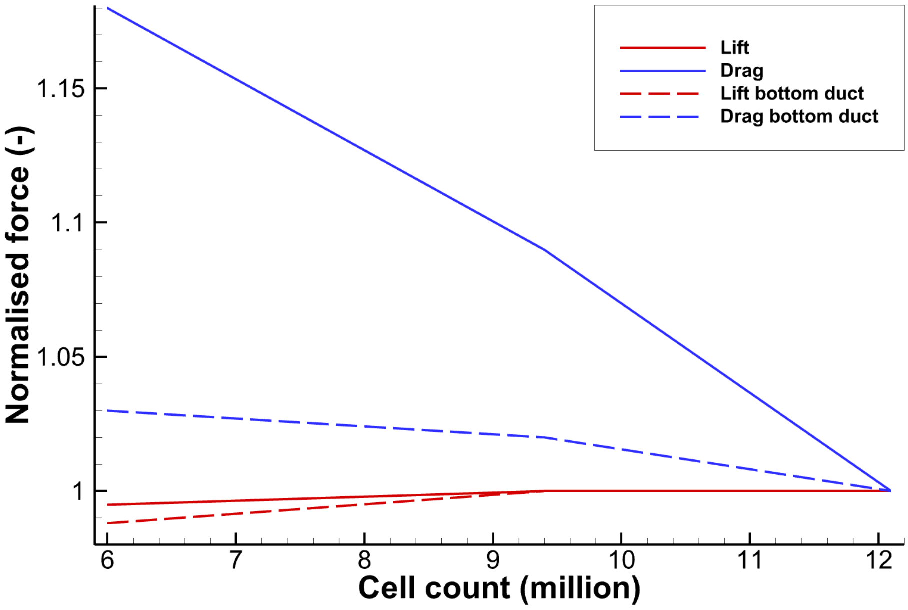

Figure A.4: Normalised forces for different mesh destinies with the ducted propeller at v_∞ = 13 m/s, J_∞ = 0.522, α = 35°, $\theta_{0.75}$ = 19°. The normalisation is done by dividing the force by the value of the same force found for the fine mesh. This makes the values for the fine mesh all equal to 1. The mesh count displayed are for the mid (6 millions), fine (9 million) and superfine (12 million) meshes.

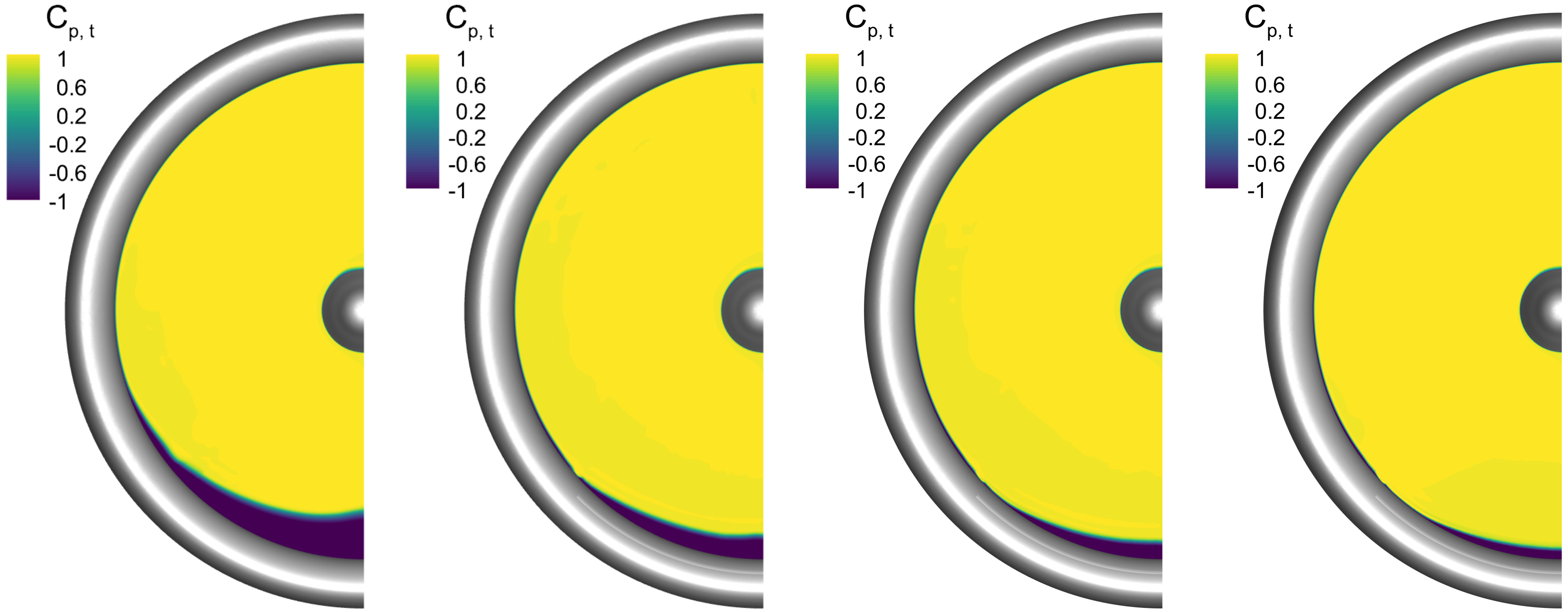

(a) Distortion on the natural duct
DC60 = 0.27

(b) Distortion with $C_\mu = 4\%$
DC60 = 0.14

(c) Distortion with $C_\mu = 5\%$
DC60 = 0.09

(d) Distortion with $C_\mu = 6\%$
DC60 = 0.06

Figure A.5: Inlet distortion on the AIP at v_∞ = 13 m/s, J_∞ = 0.522, α = 35°, $\theta_{0.75}$ = 19°
Active tangential blowing
Same figures as in section 5.2, but enlarged for clarity.